UCLouvain
Institute of Mechanics,
Materials and Civil Engineering

A Simulation Framework for Inviscid Unsteady Aerodynamics of Flexible Bodies

Application to Schooling Fish

Doctoral dissertation presented by
Denis DUMOULIN
in partial fulfillment of the requirements for
the degree of Doctor in Engineering Sciences

June 2024

Thesis committee
Pr. Philippe CHATELAIN (supervisor, UCLouvain)
Pr. Aude SIMAR (chairperson, UCLouvain)
Pr. Grégoire WINCKELMANS (UCLouvain)
Pr. Karen MULLENERS (EPFL)
Pr. Jeff D. ELDREDGE (UCLA)
Pr. Grigorios DIMITRIADIS (ULiège)

"Sindjeu!"

– K. Vandenbossche, 2012

Remerciements

"Une thèse ça s'écrit pas tout seul" est l'une des phrases les plus vraies qu'un doctorant puisse entendre. Si techniquement, j'ai effectivement été la seule personne à écrire ces quelque pages, ce travail demeure néanmoins l'œuvre d'un environnement, d'une myriade d'expériences et surtout d'une multitude d'interactions humaines plus que nécessaires afin de maintenir le cap menant à l'élaboration de cet ouvrage. Il convient dès lors de mettre en lumière tout le beau monde ayant, d'une quelconque manière, influencé mon humeur, ma santé ou mon travail au long des cinq dernières années.

Je remercie d'abord ma famille pour m'avoir supporté pendant si longtemps malgré mon manque manifeste de communication ou d'émotivité apparente, mes caprices incommensurables et ma récurrente insurrection.

Je souhaite également partager mes sentiments les mieuxveillants et les plus reconnaissants envers toute personne ayant séjourné au 31. En particulier, Nicolas, Gilles, Mathieu, Mathias et Quentin avez à tant de reprises égayé mes soirées après de longues heures de doute, de bug, ou de flemme olympique. Vous m'avez fait confiance pour un tout autre projet et j'espère profondément vous avoir fourni un lieu de vie confortable où vous avez pu vous sentir pleinement chez vous. Le Sbuff, c'était sympa de t'héberger. Rends la calculette maintenant.

Mes pensées se tournent ensuite vers un état où j'ai passé tant d'heures de rire, d'effort, de froid et d'effroi : suspendu au bout d'une corde. Sur site naturel ou artificiel, en moulinette ou en tête, au pied ou au sommet d'une paroi, merci à tous ceux entre les mains de qui j'ai eu le plaisir de laisser le sort de ma vie, et qui m'ont confié l'immense honneur de risquer la leur malgré tous les signes avant-coureurs que je leur ai pourtant clairement manifestés. Nicolas, Gilles , Quentin, Bruno, Thib, Anthilde, Matoine, Éléonore, Fede, Sara, Emile, et tant d'autres, je vous souhaite de vivre encore tant d'expériences aussi sensationnelles que celles que l'on a partagées. Julien, merci pour ces moments de stress, de chutes immenses, de joie, de doigts pétés, de tendinites, et d'autres plaisirs sensoriels ne menant pas au bonheur. Prenez soin de vous, on n'est jamais trop prudent.

Je remercie la jeunesse de Thy-le-Château, qui pour la plupart sont tout a fait agnostiques des joies et plaisirs que procure une thèse de doctorat en mécanique des fluides numériques. Dieu vous en garde. Merci à la bande du bois de Thy et sympathisants pour toutes ces soirées plus qu'endiablées et aux frères de la Gaule pour ces truites à gogo. Merci au Booster pour nos arsouilles à 50km/h en pocket bike à travers tout le royaume. Albert, fais gaffe aux priorités de droite pour l'amour du Christ! D'ailleurs, merci aux Jésus B et au 5650 pour les vacances et les nombreuses soirées par trop arrosées. Impossible de ne pas citer les e$cro, merci pour les jeux de massacre.

En outre, il est important de souligner un caractère hors du commun du laboratoire TFL: il y règne une atmosphère très positive voire festive dans laquelle travailler est un vrai plaisir. Merci aux nombreux collègues sans qui les drinks n'existeraient pas ou à tout le moins auraient une saveur bien différente. Je remercie particulièrement François pour son diabète, Pierre pour son anti-diabète, Xavier pour le *Tie Tuesday*, Mathieu pour son infinie sapience, Louis et Gilles pour leur traitrise, Victoria pour la fin de thèse, Alice pour le Pastis, Jaoma pour son bitchage, Anouk pour ses convictions, Romain pour son sérieux, JB pour ses vomis et Youri.

Aurel, merci pour tous ces mêmes de haute qualité et surtout pour le reste.

Enfin, après ceux qui m'ont maintenu la tête hors de l'eau, le temps est venu de louer ceux qui m'ont appris à nager. Prof. Philippe Chatelain, aka Boss, Mad Dog ou encore Philch... Merci pour tout ce pognon lol. Merci pour ton expertise, ta créativité presque industrielle, ta bonne humeur et ta bienveillance remarquables. Merci au temps alloué à mes recherches et à la patience dont tu as pu faire preuve. Enfin, merci pour ce que tu es. Tes blagues loufoques mériteraient un manuscrit à elles seules. Il me faut également témoigner mes plus grands respect et reconnaissance aux Vortex Gurus : Prof. Grégoire Winckelmans, Denis-Gabriel et Thomas. Vous êtes parvenus à initier un mécréant aux méthodes vortex, à partager votre passion tant pour les outils analytiques que numériques. Merci au Dr. Flavio Noca pour le rapport Galcit96 and many thanks to Prof. Jeff Eldredge for your warm support and enthusiasm. I could not have made it through without your work. Victor, merci pour ta sagesse et tes sordides histoires chinées sur reddit. Enfin, je remercie Lejeune Max, Tignace et Marion qui ont beaucoup contribué à mes recherches. J'ai eu beaucoup d'agrément à travailler, chercher des bugs, pratiquer le kicker et guindailler avec vous. Enfin merci au personnel administratif et technique pour leur travail de grande qualité; merci à Isabelle pour avoir pris soin de mes paperasses, à Frank et Julien pour les races qu'on a pu vous mettre au Royal St-Eloi Kicker Championship. Mes derniers remerciements s'adressent à Benoit Herman: chaque caractère de ce texte fut dactylographié sans douleur aux bras.

Ce travail fut difficile mais il aurait été impossible sans vous.

Finalement, merci à vous qui vous hasardez à parcourir cet ouvrage.
Bonne lecture,
Denis

Contents

Introduction

The quantification of biological locomotion within fluidic environments encompasses a broad spectrum of engineering utility. The delineation of aquatic propulsion characteristics as well as the elucidation of the remarkable energy efficiency exhibited by various species and the intricate nature of the associated flow patterns [see 67] still remain to this day very challenging endeavours. In spite of many attempts, no man-made device has yet managed to rival the spectacular maneuverability and efficiency of these complex biological systems. In addition, gregarious aquatic animals demonstrate astounding synergies to harvest the energy made available in their surroundings by their peers to diminish even further their energetic necessities. Even though their sensing mechanisms [see 12] are getting better understood, the analysis of the subtle physical mechanisms entailed by specific schooling patterns at the scale of the fluid remain a challenge for biologists and experts in numerical simulations alike.

Amongst biomechanicists who played a huge role in unveiling the complex intricacies implied by fish swimming, Van Leeuwen [68] reviewed the muscular action of different species in different swimming modes using data obtained with cameras and electromyograms gathered by Jayne and Lauder [30], Blight [6] and Van Leeuwen et al. [69]. Muller and van Leeuwen [47] combined high speed cameras and segmentation methods to extract the kinematics of the spine of a larval zebrafish. Later, Muller et al. [46] used particle image velocimetry to link the spine deformation pattern to trailing vortical flow structures. Voesenek et al. [72] used 3D cameras capable of automatic tracking to follow swimming zebrafish larvae and post process the data to obtain the hydrodynamic force and moment resulting from the swimming gait. In parallel, [66] and Eloy [19] reviewed the optimal swimming regimes of different species of fish.

In addition to observation and experiments which have continuously kept biologists engaged for more than one century [see 54, 25, 42], mathematical models and computational simulations play a pivotal role in the task of comprehending these complex phenomena.

Pioneer in the theory of swimming mechanisms, Lighthill [40] proposed a Slender Body Theory to examine what transverse oscillatory swimming gaits generate highest swimming efficiencies. That theory based on so-called *reactive forces* between a small volume of water and the body surface has later been extended in [41] to account for larger amplitudes of swimming motion. This theoretical model has recently been used in robotics applications in [7] and [55]. In parallel were carried out other endeavours relying on more computationally intensive methods such as [32] and [48] where articulated or deforming bodies in potential flows were simulated. Schooling formations in potential flows were investigated in [23]. Although planar swimming dynamics are mostly attributed to *added mass* effects well captured by these methods, a significant contribution from vorticity in the reactive forces propelling the swimmers is lacking in potential flow theory. To correct this anomaly, Kanso [31] proposed a simple model where compact vorticity dipoles are shed by the swimmers. On the other hand, other models with a more sophisticated strategy for the shedding of compact vorticity have been developed [see 75, 64, 80] but their field of application remains restricted to the realm of imposed kinematics.

On top of the inaccuracy inherent to these mostly irrotational models, the absence of viscosity in the flow casts an additional layer of shadow on the validity of the obtained solutions. This was addressed by precise simulations involving Computational Fluid Dynamics (CFD) methods, such as the seminal work of Carling et al. [8]. In [34], a commercial software relying on finite volume is used in the case of a single continuously deforming swimmer. Along recent advances in computational resources came more refined numerical frameworks allowing Direct Numerical Simulation of the flow around a single or multiple of these swimmers. Gazzola et al. [22] designed a vorticity-based Lagrangian method for immersed bodies with arbitrary deformation allowing accurate simulations of multiple anguilliform swimmers. This framework was re-used in [24] to determine optimal C-start gaits for larval fish. In parallel, the biomechanics of the initialization of swimming motion for zebrafish larvae were also studied by Li et al. [38] where they used finite-volume model of Liu [43]. So far, all these CFD methods remained agnostic to the bending moments that are the root cause of any deformation. The pioneering work of Hess and Videler [28] concluded from kinematics data obtained from swimming patterns of *pollachius virens* (a caranguiform fish) that contrary to the deformation signal, the bending moment distribution does not act as a fast traveling wave from head to tail but as a standing wave. Cheng et al. [9] confirmed these results for the sames species with a visco-elastic 3D beam model also based on experimental data. This standing wave was also observed by Voesenek et al. [71] when they studied bending moments using a complete model coupling automatic 3D reconstruction of kinematics from cameras with a large amplitude beam model and direct numerical simulations of Navier-Stokes equations.

In other attempts aiming at shedding light on internal mechanics of eel-like swimmers, Eldredge [16] coupled a Multi-Body System (MBS) solver to Navier-Stokes equations to simulate the dynamics of a swimmer composed of three articulated ellipses. Kinematics of more general geometries were studied by Li et al. [39] where they coupled an MBS with the commercial software *Fluent*. Bernier et al. [3] proposed a Vortex Particle-Mesh method coupled with an MBS for the simulation of 2D articulated swimmers in the wake of a cylinder and measured their energy expenditure. This framework was re-used in [4] for energy harvesting purposes using mechanical dampers to store energy.

With the recent development of machine learning, model-free control strategies were developed at the scale of a single swimmer: Mandralis et al. [44] designed escape patterns in larval fish under energy optimization. But primarily for flow configurations involving several swimmers: Novati et al. [50] applied Deep Reinforcement Learning [see 63] coupled with vortex-based 2D direct numerical simulations on the optimization of the propulsive power of a fish following another. Verma et al. [70] extended this to 3D and to a 2-leader 1-follower configuration. These data-driven methods were also used for lower-order fluid models involving schools of a hundred swimmers in purely potential flow by Gazzola et al. [23], for flow sensing purposes by Weber et al. [76] or for navigating in a von Karman vortex street by Gunnarson et al. [27].

We are convinced that these learning methods are a turning point in research on fish swimming and can unveil many mechanisms hidden by the complexity of fluid-body interactions. However, most Deep Reinforcement Learning frameworks require massive amounts of data from simulations the higher-end of which are very computationally intensive. Therefore, we are still in need for low-order models of enough accuracy. To that end, we propose an extension of the unsteady panel method with vortex shedding of Xia and Mohseni [80] to self-propelled deforming anguilliform swimmers coupled with the MBS proposed by Bernier et al. [3] formulated for both inverse dynamics in the aim of retrieving the actuation moments of a swimmer and direct dynamics for direct control of the swimmers. We also base our model on the *added mass* formalism of Kanso et al. [32] for stabilization purposes. This complete framework enables simulations of many swimming individuals in finite time-horizons with moderate computational cost, while still capturing the main flow characteristics.

In this manuscript, we aim at answering the following questions:

- Can a low-order simulation framework approximate the dynamics of a school of fish?
- How can this model be adapted to retrieve information on swimming performance?
- Given our framework, what are the energetic benefits of collective swimming?
- Can we make the framework modular enough to enable simple maneuvering and control strategies?
- Can we make the framework fast enough for keeping the data generation process of model-free control strategies feasible with reasonable computational and temporal resources ?

Outline of the manuscript

This work starts with the presentation of the mathematical and numerical methods composing the simulation framework developed to tackle these questions. We begin by describing the building blocks of the vorticity-based unsteady panel method lying at the root of the tool and how these parts are assembled together to form a solvable system representing a body immersed in an inviscid flow with vortex shedding. Three different ways of retrieving aerodynamic coefficients are then presented. Finally, the framework is verified and validated on the case airfoils undergoing rigid motion.

In Chapter 2, the simulation framework is extended to self-propelled flexible bodies in the context of eel-like fish swimming. After describing the geometrical design of such swimmers as well as their swimming gait, focus is set on the fluid-structure interaction and the numerical tools necessary to the design of a stable framework enabling swimming dynamics of one or multiple bodies. Simulations are then compared with similar setups simulated by means of finite-volume and vortex-based CFD methods. Turning maneuvers through body curvature modulation are examined as well as the impact of nearby vorticity on the swimming dynamics and kinematics.

To complete the model, Chapter 3 introduces the Euler-Lagrange formalism in an attempt to represent the anguilliform swimmer as a chain of articulated links. This representation not only allows to expose the energetic facets of a given swimming gait but also enables the direct control of the swimmer through its articulations, as would be the case in actual robotics applications. We demonstrate this extension first on a simpler system composed of rigid ellipses prior to focusing on a continuous eel-like swimmer. The extension is validated with *Robotran* [see 14], a commercial solver for multi-body systems.

Chapter 4 proposes an upgrade of the initial framework for rigid bodies where amalgamation of free vorticity is taken advantage of in order to leverage computational complexity. Generalizing the work of Darakananda and Eldredge [13] to bodies terminated with a wedged trailing edge, this lumping of vorticity is carried out in an impulse-preserving fashion to avoid any spurious effect on the lift/drag coefficients. This lower-order model is then validated on the same benchmarks as in Chapter 1.

Finally, this work ends with conclusions and proposals for future work addressing limitations and prospective extensions.

CHAPTER 1

An unsteady model for inviscid flows

In this Chapter, we present the tools and methods used to elaborate the numerical framework serving as a basis for the extensions developed in further Chapters. Our model aims at simulating inviscid flows around two-dimensional objects. To be more specific, it is restricted to elongated bodies characterized with a trailing edge of finite-angle from which flow separates into a wake of vorticity. All notions of fluid mechanics presented below can be found in [11, 18, 37, 2, 78, 33], among other.

This first Chapter is structured as follows: Section 1.1 presents fundamental physics of incompressible flows. Section 1.2 focuses on the building bricks of the framework, namely vortex elements. Then, Section 1.3 gives the physical constraints the flow-body system needs to obey and how they are used together to solve for vorticity on the body surface in Section 1.4. Section 1.5 presents ways to compute the surface pressure and aerodynamic loads while Section 1.6 provides details on the algorithm used to advance the flow simulation in time. The system is validated in Section 1.7 before a summary in a short discussion in Section 1.8.

1.1 Incompressible irrotational unsteady planar flows

A quick and dirty definition of vorticity would be the tendency of the flow to whirl around itself. It is quantitatively defined as the curl of the velocity field:

$$\boldsymbol{\omega} = \nabla \times \boldsymbol{u}. \tag{1.1}$$

In two-dimensional flow domains ($\mathcal{N}_d = 2$), vorticity is oriented in the out-of-plane direction $\hat{\boldsymbol{e}}_z$.

The incompressibility constraint requires a uniform density field ρ anywhere in the flow domain. Coupled with the conservation of mass which imposes a zero mass-flux on any closed surface in the domain, it results in a constraint on the velocity field

$$\nabla \cdot \boldsymbol{u} = 0, \tag{1.2}$$

known as the continuity equation.

The restriction to two-dimensional domains means that a few quantities are defined per unit length. For instance, a volume of fluid $\mathscr{V}_f$ is in fact a volume per unit length, i.e. a surface area, and the surface $\mathscr{S}_b$ bounding such a volume becomes a path.

1.2 Vortex elements

In this Section, we define the basic tools required to build the flow model. Namely, vortex elements. These elements are each responsible for specific vorticity distributions the addition of which produce more or less complex flow structures.

If the total vorticity distribution $\boldsymbol{\omega}$ is known in a flow domain $\mathscr{V}_f$, the associated velocity field is the solution of the Poisson problem for incompressible flows:

$$\nabla^2 \boldsymbol{u}(\boldsymbol{x}) = -\nabla \times \boldsymbol{\omega}(\boldsymbol{x}). \tag{1.3}$$

Using the identity $\nabla \times (\nabla^2 \boldsymbol{a}) = \nabla^2(\nabla \times \boldsymbol{a})$, this problem can be turned into

$$\nabla^2 \boldsymbol{\psi}(\boldsymbol{x}) = -\boldsymbol{\omega}(\boldsymbol{x}), \tag{1.4}$$

where $\boldsymbol{\psi}$ is the streamfunction; its curl then gives the flow velocity $\nabla \times \boldsymbol{\psi} = \boldsymbol{u}$. It bears that name because its iso-contours represent streamlines of the flow. In bidimensional flow problems, the streamfunction has a single component along $\hat{\boldsymbol{e}}_z$, just like $\boldsymbol{\omega}$.

The solution of the Poisson equation with a general forcing term is found by convolving the forcing term with the so-called Green's function. This function is defined as the solution of the simpler Poisson equation:

$$\nabla^2 G(\boldsymbol{x}) = -\delta(\boldsymbol{x}), \tag{1.5}$$

where $\delta(\boldsymbol{x})$ is the Dirac delta function. In unbounded planar domains, the solution to Eq. (1.5) is

$$G(\boldsymbol{x}) = -\frac{1}{2\pi} \log |\boldsymbol{x}|. \tag{1.6}$$

Therefore, the solution to Eq. (1.4) is

$$\boldsymbol{\psi}(\boldsymbol{x}) = \int_{\mathscr{V}_f} G(\boldsymbol{x}-\boldsymbol{y})\boldsymbol{\omega}(\boldsymbol{y})\,\mathrm{d}V(\boldsymbol{y}). \tag{1.7}$$

By taking the curl of Eq. (1.7), we obtain the solution of Eq. (1.3) called the *Biot-Savart* integral

$$\boldsymbol{u}(\boldsymbol{x}) = \int_{\mathscr{V}_f} \boldsymbol{K}\,(\boldsymbol{x}-\boldsymbol{y}) \times \boldsymbol{\omega}(\boldsymbol{y})\,\mathrm{d}V(\boldsymbol{y}), \tag{1.8}$$

where we define the velocity kernel $\boldsymbol{K}$ as the gradient of the Green's function:

$$\boldsymbol{K}(\boldsymbol{x}) = \nabla G(\boldsymbol{x}) = -\frac{\boldsymbol{x}}{2\pi|\boldsymbol{x}|^2}. \tag{1.9}$$

We have just presented how to compute the flow velocity when the vorticity field is known everywhere on $\mathscr{V}_f$ but have yet to demonstrate how to calculate the vorticity. As discussed earlier, vorticity results from the combination of several vortex elements carried by the flow. There exists two species of such elements in planar domains: point vortices and vortex sheets.

1.2.1 Point vortex

As its name suggests, a point vortex is the integral of a vorticity distribution localized at a single point. It is fully determined by two parameters: its circulation Γ and position $\boldsymbol{y}$; its expression is given by

$$\boldsymbol{\omega}(\boldsymbol{x}) = \Gamma\delta(\boldsymbol{x}-\boldsymbol{y})\hat{\boldsymbol{e}}_z. \tag{1.10}$$

The solution of the Laplace problem whose forcing term is a point vortex is rather straightforward given the similarity between the right hand side of Eqs. (1.10) and (1.5). The streamfunction induced by a point vortex is therefore

$$\boldsymbol{\psi}(\boldsymbol{x}) = -\frac{\Gamma\hat{\boldsymbol{e}}_z}{2\pi}\log|\boldsymbol{x}-\boldsymbol{y}|, \tag{1.11}$$

and the induced velocity field is

$$\boldsymbol{u}(\boldsymbol{x}) = -\frac{\Gamma(\boldsymbol{x}-\boldsymbol{y})}{2\pi|\boldsymbol{x}-\boldsymbol{y}|^2} \times \hat{\boldsymbol{e}}_z, \tag{1.12}$$

where $\boldsymbol{x} \neq \boldsymbol{y}$.

To avoid any numerical issue caused by the growth of velocity magnitude as $\boldsymbol{x} \to \boldsymbol{y}$, it is common practice to regularize the forcing term of the Laplace problem by replacing the Dirac delta function with a smooth distribution, see [77]. In practice, it results in a smooth velocity field with no singularity. Two of the most popular regularization kernels are the *Rosenhead-Moore* low-order algebraic kernel [58]:

$$\boldsymbol{K}_\delta(\boldsymbol{x}) = -\frac{\boldsymbol{x}}{2\pi(|\boldsymbol{x}|^2 + \delta^2)}, \tag{1.13}$$

and the *Lamb-Oseen* Gaussian kernel [52]:

$$\boldsymbol{K}_\delta(\boldsymbol{x}) = -\frac{\boldsymbol{x}}{2\pi(|\boldsymbol{x}|^2)}\left(1 - \exp\left(-\frac{|\boldsymbol{x}|^2}{\delta^2}\right)\right). \tag{1.14}$$

Whether a regularization is applied or not, a point vortex does not influence its own transport velocity given the form of Eq. (1.12).

1.2.2 Vortex sheet

A vortex sheet is a surface on which an amount of circulation is distributed. Its main effect is a discontinuity in the velocity tangent to the sheet. It is fully characterized by the sheet $\mathcal{S}$ and its vortex strength distribution $\boldsymbol{\gamma}(\boldsymbol{x})$.

The streamfunction associated to a vortex sheet is

$$\boldsymbol{\psi}(\boldsymbol{x}) = \int_{\mathcal{S}} G(\boldsymbol{x} - \boldsymbol{y})\boldsymbol{\gamma}(\boldsymbol{y})\,\mathrm{d}S(\boldsymbol{y}), \tag{1.15}$$

and the velocity it induces is

$$\boldsymbol{u}(\boldsymbol{x}) = \int_{\mathcal{S}} \boldsymbol{K}(\boldsymbol{x} - \boldsymbol{y}) \times \boldsymbol{\gamma}(\boldsymbol{y})\,\mathrm{d}S(\boldsymbol{y}), \tag{1.16}$$

where $\boldsymbol{x} \notin \mathcal{S}$. What happens when $\boldsymbol{x} \in \mathcal{S}$ will be the topic of Section 1.3.1.

In bidimensional domains, the vortex strength is directed along $\hat{\boldsymbol{e}}_z$. It has units of velocity and represents the tangential velocity jump across the sheet. To put it formally, for a point $\boldsymbol{x} \in \mathcal{S}$,

$$\boldsymbol{\gamma}(\boldsymbol{x}) \times \boldsymbol{n}(\boldsymbol{x}) = \boldsymbol{u}^+(\boldsymbol{x}) - \boldsymbol{u}^-(\boldsymbol{x}), \tag{1.17}$$

where $\boldsymbol{n}$ is the normal unit vector, $\boldsymbol{u}^+$ and $\boldsymbol{u}^-$ are the velocities above and below the sheet, as shown in Fig. 1.1. Because Eq. (1.17) forms a right-handed orthogonal coordinate system, we can also write

$$\boldsymbol{\gamma}(\boldsymbol{x}) = \boldsymbol{n}(\boldsymbol{x}) \times \left(\boldsymbol{u}^+(\boldsymbol{x}) - \boldsymbol{u}^-(\boldsymbol{x})\right). \tag{1.18}$$

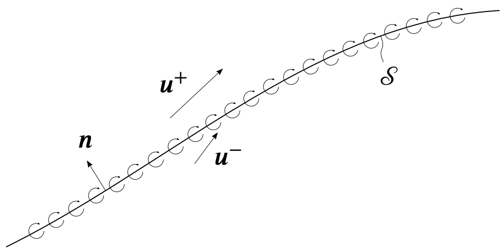

Figure 1.1: A bidimensional vortex sheet with a negative vortex strength $\boldsymbol{\gamma}$.

The velocity of the sheet itself is the average of the flow velocities on either side of it. Namely

$$\boldsymbol{u}_s(\boldsymbol{x}) = \frac{1}{2}\left(\boldsymbol{u}^+(\boldsymbol{x}) + \boldsymbol{u}^-(\boldsymbol{x})\right). \tag{1.19}$$

1.3 The immersed body

In a flow domain $\mathcal{V}_f$ extending to infinity with a flow velocity $\boldsymbol{u}$, the immersed body is a volume $\mathcal{V}_b$ evolving with velocity $\boldsymbol{u}_b$.

Its surface is marked with a velocity discontinuity: $\boldsymbol{u}_b$ inside of the body and $\boldsymbol{u}$ outside of it. Therefore, the body surface $\mathcal{S}_b$ must be represented by a vortex sheet. This bound vorticity is defined by

$$\boldsymbol{\gamma} \times \boldsymbol{n} = \boldsymbol{u} - \boldsymbol{u}_b, \tag{1.20}$$

where $\boldsymbol{n}$ is the unit normal vector pointing towards the fluid.

Because the body evolves with an arbitrary velocity, there is no reason for the bound vortex sheet to be steady. Additionally, if the body presents a wedge angle at its trailing edge, the velocity discontinuity leaves the body and some vorticity is shed inside of $\mathcal{V}_f$. This free vorticity remains compact and is represented by a vortex sheet of uniform strength γ_s in the near vicinity of the trailing edge followed by point vorticity [see 59, 10] as we get further away from the body. Such a formalism is illustrated in Fig. 1.2 where $\mathcal{S}_s \subset \mathcal{V}_f$ represents the free vortex sheet.

Let us now make an important point: the body surface is impenetrable, i.e. no flow can penetrate it. A swift manipulation of Eq. (1.20) yields the boundary condition

$$\boldsymbol{u}_b \cdot \boldsymbol{n} = \boldsymbol{u} \cdot \boldsymbol{n}, \tag{1.21}$$

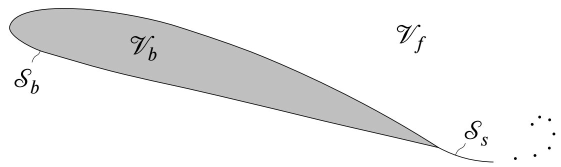

Figure 1.2: A fluid-body system where an immersed body sheds free vorticity at its trailing edge. The flow is irrotational everywhere except on $\mathscr{S}_b$ and on $\mathscr{S}_s$.

which holds everywhere on the body surface except for the very trailing edge where free vorticity leaves the body.

To determine the bound vorticity $\boldsymbol{\gamma}$, we now need to compute the flow velocity just outside the body as well as the strength and direction of the free vortex sheet. As this task is not straightforward, it is the topic of the following Sections.

1.3.1 The impenetrable body equation

The equation to impose on the body surface comes from the curl of Green's third identity (see Eq. (A.6)) where $\boldsymbol{u}$ is the external flow velocity and $\boldsymbol{u}_b$ is the body velocity. Considering the divergence-free nature of both vector fields, with Eq. (1.20) and the boundary condition (1.21) on $\mathscr{S}_b$, we obtain:

$$\begin{aligned}\frac{1}{2}\boldsymbol{\gamma}(\boldsymbol{x})\times\boldsymbol{n}(\boldsymbol{x})+\boldsymbol{u}_b(\boldsymbol{x}) = &\int_{\mathscr{V}_f}\boldsymbol{K}\left(\boldsymbol{x}-\boldsymbol{y}\right)\times\boldsymbol{\omega}\,\mathrm{d}V+\int_{\mathscr{V}_b}\boldsymbol{K}\left(\boldsymbol{x}-\boldsymbol{y}\right)\times\left(\nabla\times\boldsymbol{u}_b\right)\,\mathrm{d}V\\ &+\fint_{\mathscr{S}_b}\boldsymbol{K}\left(\boldsymbol{x}-\boldsymbol{y}\right)\times\boldsymbol{\gamma}\,\mathrm{d}S,\end{aligned}\tag{1.22}$$

where $\boldsymbol{x}\in\mathscr{S}_b$ and where the integral over $\mathscr{V}_b$ represents the vorticity associated with body rotation. We dropped the dependency on the integration variable $\boldsymbol{y}$ for the sake of clarity. We can now subtract $\boldsymbol{u}_b$ on both sides and using Eq. (A.3), we obtain

$$\begin{aligned}\frac{1}{2}\boldsymbol{\gamma}(\boldsymbol{x})\times\boldsymbol{n}(\boldsymbol{x}) = &\int_{\mathscr{V}_f}\boldsymbol{K}\left(\boldsymbol{x}-\boldsymbol{y}\right)\times\boldsymbol{\omega}\,\mathrm{d}V+\fint_{\mathscr{S}_b}\boldsymbol{K}\left(\boldsymbol{x}-\boldsymbol{y}\right)\times\boldsymbol{\gamma}\,\mathrm{d}S-\frac{1}{2}\boldsymbol{u}_b(\boldsymbol{x})\\ &+\fint_{\mathscr{S}_b}\left[\boldsymbol{K}\left(\boldsymbol{x}-\boldsymbol{y}\right)\times\left(\boldsymbol{n}\times\boldsymbol{u}_b\right)-\boldsymbol{K}\left(\boldsymbol{x}-\boldsymbol{y}\right)\left(\boldsymbol{n}\cdot\boldsymbol{u}_b\right)\right]\,\mathrm{d}S.\end{aligned}\tag{1.23}$$

Finally, by grouping together all terms involving $\boldsymbol{\gamma}$, we get the so-called impenetrable body equation for $\boldsymbol{x} \in \mathcal{S}_b$:

$$\begin{aligned}
\frac{1}{2}\boldsymbol{n}(\boldsymbol{x}) \times \boldsymbol{\gamma}(\boldsymbol{x}) + &\fint_{\mathcal{S}_b} \boldsymbol{K}(\boldsymbol{x}-\boldsymbol{y}) \times \boldsymbol{\gamma}\, \mathrm{d}S = \\
&- \int_{\mathcal{V}_f} \boldsymbol{K}(\boldsymbol{x}-\boldsymbol{y}) \times \boldsymbol{\omega}\, \mathrm{d}V + \frac{1}{2}\boldsymbol{u}_b(\boldsymbol{x}) \\
&- \fint_{\mathcal{S}_b} \left[\boldsymbol{K}(\boldsymbol{x}-\boldsymbol{y}) \times \left(\boldsymbol{n} \times \boldsymbol{u}_b\right) - \boldsymbol{K}(\boldsymbol{x}-\boldsymbol{y})\left(\boldsymbol{n}\cdot\boldsymbol{u}_b\right)\right] \mathrm{d}S.
\end{aligned} \tag{1.24}$$

Despite the vectorial character of this equation, only the component normal to the body surface is necessary to impose the no-flow-through boundary condition. The tangential component is therefore relaxed.

1.3.2 Kelvin's conservation of circulation

The linear system to solve for $\boldsymbol{\gamma}$ resulting from the imposition of a non-penetration condition on the body surface has a non-null kernel space. Additional conditions are therefore required to regularize the system and fix the integration constant. Thankfully, it is well known that the overall circulation in a planar flow must remain constant, or

$$\frac{\mathrm{d}\Gamma}{\mathrm{d}t} = 0. \tag{1.25}$$

Therefore, we can impose $\Gamma = 0$ at every time step of a simulation. This constraint can be written

$$\int_{\mathcal{V}_f} \boldsymbol{\omega}\, \mathrm{d}V(\boldsymbol{y}) + \oint_{\mathcal{S}_b} \boldsymbol{\gamma}\, \mathrm{d}S(\boldsymbol{y}) + \oint_{\mathcal{S}_b} \boldsymbol{n} \times \boldsymbol{u}_b\, \mathrm{d}S(\boldsymbol{y}) = 0. \tag{1.26}$$

1.3.3 Unsteady Kutta condition

The final condition to close the system concerns the creation of free vorticity in the flow at the trailing edge of the body. This is called the *Kutta* condition. The approach proposed in Eldredge [18] where conservation of mass and continuity of velocity are imposed inevitably results in a free vortex sheet tangent to either side of the trailing edge and a stagnation point. At each transition, numerical instabilities occur due to the sudden change in the shedding direction. We relax the continuity constraint on the velocity field and rather impose it on the vorticity flux at the trailing edge. This allows for smooth variations in the shedding direction while still producing a stagnation point on either side when the flow demands it. Additionally, it complies with the steady flow Kutta condition where vorticity is shed along the bisector of the trailing edge angle. This unsteady condition originates from the work of Xia and Mohseni [80] and can be summarized as follows:

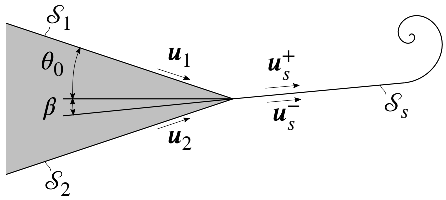

Figure 1.3: Close up view at the trailing edge.

Without loss of generality, the trailing edge condition is derived in a frame of reference rigidly attached to the body (i.e. $\boldsymbol{u}_b = 0$). In such a configuration – shown in Fig. 1.3 – the bisector of the trailing edge angle is aligned with $\hat{\boldsymbol{e}}_x$ and creates an angle $\pm\theta_0$ with the trailing edge panels $\mathcal{S}_1$ and $\mathcal{S}_2$. We define the angle β as the orientation of the free vortex sheet $\mathcal{S}_s$ just behind the trailing edge with respect to $\hat{\boldsymbol{e}}_x$. Finally, the vortex strengths on the body panels and on the free vortex sheet are given by

$$\begin{cases} \gamma_+ = u_1 - u_b = u_1, \\ \gamma_- = -(u_2 - u_b) = -u_2, \\ \gamma_s = u_s^+ - u_s^-. \end{cases} \tag{1.27}$$

We can now impose constraints determining both the direction and the strength of the shed vortex sheet. The conservation of mass above and below the free vortex sheet links the vortex strength to its direction:

$$\gamma_s = \gamma_+ \cos(\theta_0 + \beta) + \gamma_- \cos(\theta_0 - \beta). \tag{1.28}$$

Using the conservation of vorticity flux, Xia and Mohseni [80] give an equation for the shedding direction:

$$\theta_0 + \beta = \arccos\left(\frac{u_1^2 + u_3^2 - u_2^2}{2u_1u_3}\right), \tag{1.29}$$

where $u_3 = -\sqrt{u_1^2 + u_2^2 + 2u_1 u_2 \cos(2\theta_0)}$.

For the sake of simplicity, we only expose here the final results enabling the flow model. For a detailed expose on the matter, we refer either to [80] or to Appendix B where a clearer and simpler way to achieve and present equivalent results is proposed. This appendix is the work of Prof. Winckelmans.

1.4 Discretization and solving for vorticity

So far, all these equations and boundary conditions were given for an assumed continuous and smooth surface. However, to implement this model in a computer, one needs to discretize the time domain as well the vorticity surfaces both on the body and in the free flow. This discretization is presented graphically in Fig. 1.4 and is now detailed.

To stay consistent with the model of Xia and Mohseni [80], a set of N_p panels of linearly varying vortex strength enclose the body surface $\mathcal{S}_b$. The first and last of these panels make for the finite-angle trailing edge. The sharp angle makes ensuring the continuity of velocity impossible. For this reason and to avoid any singularity resulting from the discontinuity of velocity at that point, a ball of small radius ε is truncated from the flow domain, and hence from the vortex sheets, at the trailing edge.

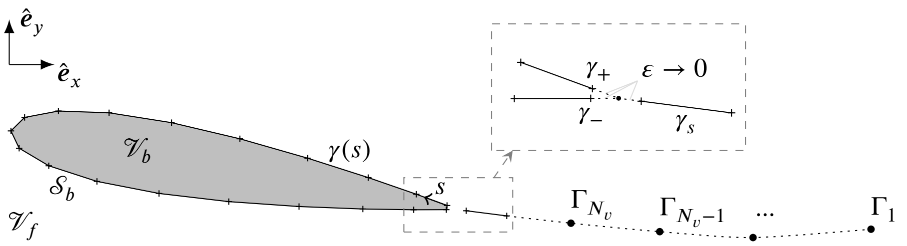

Figure 1.4: Discretization of an airfoil-shaped body in an inviscid fluid. The trailing edge and shed panels are cropped by an small length ε in order to avoid the singularity that would result from the discontinuity of the vortex sheet strength.

Free vorticity is represented in the very near wake $\mathcal{S}_u \subset \mathcal{S}_s$ with a panel of uniform vortex strength of length $2b_s$ which is transformed at each time step into a point vortex. This transformation is carried out at the vorticity centroid in a way that conserves fluid impulse. The far wake is hence composed of a finite set of point vortices, each having been created at an anterior time step. The cardinality of this set is denoted as N_v and is incremented at each time step of a simulation.

Using Eq. (1.24), Eq. (1.26) and Eq. (1.28), it is possible to build a linear system of dimension N_p+2 the solution of which gives the unknown vorticity distributed around $\mathcal{S}_b$:

$$\left[\begin{array}{c|c} A & \boldsymbol{a} \\ \hline \boldsymbol{k}^T & 2b_s \\ \hline \boldsymbol{\kappa}^T & -1 \end{array}\right] \left[\begin{array}{c} \boldsymbol{\gamma} \\ \hline \gamma_s \end{array}\right] = \left[\begin{array}{c} \boldsymbol{\chi} \\ \hline -\Gamma \\ \hline 0 \end{array}\right]. \tag{1.30}$$

The first line enforces the no-flow-through condition with A_{ij} the influence of vortex strength j and a_i the influence of the shed panel at panel i. On the RHS, χ_i holds the normal component of the right hand side of Eq. (1.24) computed at the collocation point of panel i. The second and third lines impose the Kelvin theorem and Kutta condition, respectively. Γ is the third component of the right hand side of Eq. (1.26). The solution of Eq. (1.30) provides the distribution of circulation on the profile $\boldsymbol{\gamma}$ as well as the strength γ_s of the shed panel. This system is entirely closed thanks to the knowledge of the shedding direction β determined with Eq. (1.29) at the previous temporal substep (see Section 1.6).

At the end of a time step, the shed panel is transformed into a point-vortex at its centre. In this specific case, the last column of the left hand side matrix is filled with zeros except for its last element. In other words, the strength γ_s has no contribution over the bound vortex sheet whatsoever and the Kutta condition is trivially satisfied by the existing set of point vortices. Hence, the system is reduced to

$$\underbrace{\left[\begin{array}{c} A \\ \hline \boldsymbol{k}^T \end{array}\right]}_{\tilde{A}} \left[\, \boldsymbol{\gamma} \,\right] = \left[\begin{array}{c} \boldsymbol{\chi} \\ \hline -\Gamma \end{array}\right]. \tag{1.31}$$

1.5 Hydrodynamic force and moment

Three different methods to obtain hydrodynamic loads are presented here. Each formalism has its own perks which justify its use over another in various contexts.

1.5.1 From surface traction

The hydrodynamic force and moment with respect to point $\boldsymbol{x}_p$ can be obtained by integrating the pressure on the body surface:

$$\boldsymbol{f} = -\oint_{\mathcal{S}_b} p\boldsymbol{n}\,\mathrm{d}S, \tag{1.32}$$

$$\boldsymbol{m}_{\boldsymbol{x}_p} = -\oint_{\mathcal{S}_b} (\boldsymbol{x} - \boldsymbol{x}_p) \times p\boldsymbol{n}\,\mathrm{d}S, \tag{1.33}$$

where $\boldsymbol{x}$ is the integration variable. The pressure on the surface is obtained with the Bernoulli equation [see 37, 20, 18]):

$$p = B(t) - \rho\left(\frac{1}{2}|\boldsymbol{\gamma}|^2 - \frac{1}{2}|\boldsymbol{u}_b|^2 + \frac{\mathrm{d}\varphi}{\mathrm{d}t}\right), \tag{1.34}$$

where $B(t)$ is a spatially-uniform value called the Bernoulli constant. The velocity potential can be calculated by integrating the component of fluid velocity tangent to the surface:

$$\varphi(\boldsymbol{x}) - \varphi_0 = \int_{\boldsymbol{x}_0}^{\boldsymbol{x}} \boldsymbol{u}\cdot\,\mathrm{d}\boldsymbol{\tau}, \quad \boldsymbol{x} \in \mathcal{S}_b. \tag{1.35}$$

The flow velocity $\boldsymbol{u}$ at the surface can be computed using Eq. (1.20) once the bound vorticity is known.

It is worth noting that the integral of the product of the Bernoulli integration constant and the normal vector $B(t)\boldsymbol{n}$ as well as its first moment vanish when the integration surface is closed. The velocity potential constant φ_0 disappears too when deriving φ in time.

1.5.2 Using a momentum budget

Another way of obtaining the hydrodynamic force and moment on the body is by taking the time derivative of the fluid momentum and its moment with respect to point $\boldsymbol{x}_p$.

$$\boldsymbol{f} = -\frac{\mathrm{d}\boldsymbol{p}}{\mathrm{d}t}, \tag{1.36}$$

$$\boldsymbol{m}_{\boldsymbol{x}_p} = -\frac{\mathrm{d}\boldsymbol{l}_{\boldsymbol{x}_p}}{\mathrm{d}t} - \dot{\boldsymbol{x}}_p \times \boldsymbol{p}, \tag{1.37}$$

where the fluid momentum is [see 2, 78]

$$\boldsymbol{p} = \frac{\rho}{\mathcal{N}_d - 1}\left(\int_{\mathcal{V}_f} \boldsymbol{x} \times \boldsymbol{\omega}\,\mathrm{d}V + \oint_{\mathcal{S}_b} \boldsymbol{x} \times (\boldsymbol{n} \times \boldsymbol{u})\,\mathrm{d}S\right). \tag{1.38}$$

Similarly, the angular momentum in the fluid with respect to point $\boldsymbol{x}_p$ is

$$\begin{aligned} \boldsymbol{l}_{\boldsymbol{x}_p} = \frac{\rho}{\mathcal{N}_d}\Bigg(& \int_{\mathcal{V}_f} \boldsymbol{x}' \times (\boldsymbol{x}' \times \boldsymbol{\omega})\, \mathrm{d}S \\ & + \oint_{\mathcal{S}_b} \boldsymbol{x}' \times [\boldsymbol{x}' \times (\boldsymbol{n} \times \boldsymbol{u})]\, \mathrm{d}S \Bigg), \end{aligned} \tag{1.39}$$

where $\boldsymbol{x}' = \boldsymbol{x} - \boldsymbol{x}_p$. Because of the singular character of the ambient vorticity field in our framework, volume integrals in both Eqs. (1.38) and (1.39) can be rewritten as a finite sum of contributions from each point vortex.

This formalism presents three main drawbacks: the first and least important is the non-compactness of the formulation. Indeed, the volume integral translates into a sum on all point vortices and its computation linearly scales with the cardinality of the set of free vortex elements. This is only a minor inconvenience because most of the time is spent solving for $\boldsymbol{\gamma}$ and advecting vorticity. The worst-case cost of both operations is $\mathcal{O}\left(N_p^3\right)$ and $\mathcal{O}\left(N_v^2\right)$, respectively. A second and more problematic issue is the loss of numerical accuracy as the span of the free vorticity field extends: as a point vortex gets further away from the body (i.e. $\boldsymbol{x}'$ gets larger), the fluid impulse associated with this vortex increases. Because the computation of derivatives of large numbers entails numerical errors, a point vortex far from the body results in an inaccurate force contribution. Finally, when multiple bodies are immersed, the momentum budget only gives the force (resp. moment) on the whole set of bodies instead of a force (resp. moment) for each body.

1.5.3 Using a control volume approach

A way of alleviating all these issues at once is to get rid of the integrals on $\mathcal{V}_f$ of Eqs. (1.38) and (1.39) through a control volume approach. The development of this formalism, extended from the work of Noca [49], is not straightforward and is fully detailed in Appendix C. This formalism is based on the assumption that the immersed body is neutrally buoyant in a fluid of unit density.

For $\mathcal{N}_d = 2$, it produces the hydrodynamic force

$$\begin{aligned} \boldsymbol{f} = & \oint_{\mathcal{S}_b} \left(\frac{1}{2}u'^2\boldsymbol{n} - \boldsymbol{u}'\boldsymbol{u}'_b \cdot \boldsymbol{n}\right) \,\mathrm{d}S \\ & - \frac{\mathrm{d}}{\mathrm{d}t}\oint_{\mathcal{S}_b} \boldsymbol{x}' \times (\boldsymbol{n} \times \boldsymbol{u}) \,\mathrm{d}S \\ & - \oint_{\mathcal{S}_b} \boldsymbol{n} \cdot (\boldsymbol{u} - \boldsymbol{u}_b)(\boldsymbol{x}' \times \boldsymbol{\omega}) \,\mathrm{d}S, \end{aligned} \tag{1.40}$$

where $\boldsymbol{x}' = \boldsymbol{x} - \boldsymbol{x}_p$ and $\boldsymbol{u}' = \boldsymbol{u} - \dot{\boldsymbol{x}}_p$.

The hydrodynamic moment with respect to point $\boldsymbol{x}_p$ obtained through the control volume approach is

$$\begin{aligned} \boldsymbol{m}_{\boldsymbol{x}_p} = & \oint_{\mathcal{S}_b} \boldsymbol{x}' \times \left(\frac{1}{2}u'^2\boldsymbol{n} - \boldsymbol{u}'\boldsymbol{u}'_b \cdot \boldsymbol{n}\right) \,\mathrm{d}S \\ & - \frac{1}{2}\frac{\mathrm{d}}{\mathrm{d}t}\oint_{\mathcal{S}_b} \boldsymbol{x}' \times [\boldsymbol{x}' \times (\boldsymbol{n} \times \boldsymbol{u})] \,\mathrm{d}S \\ & - \frac{1}{2}\oint_{\mathcal{S}_b} \boldsymbol{n} \cdot (\boldsymbol{u} - \boldsymbol{u}_b)[\boldsymbol{x}' \times (\boldsymbol{x}' \times \boldsymbol{\omega})] \,\mathrm{d}S \\ & + \dot{\boldsymbol{x}}_p \times \oint_{\mathcal{S}_b} \boldsymbol{n} \cdot \boldsymbol{u}_b \boldsymbol{x}' \,\mathrm{d}S. \end{aligned} \tag{1.41}$$

In the last integral of the right hand side of Eq. (1.40) appears the non-penetration condition (see Eq. (1.21)) which holds everywhere but at the trailing edge where $\mathcal{S}_b$ intercepts $\mathcal{S}_s$. Therefore, that integral accounting for the flux of momentum leaving the control volume can be rewritten as

$$\boldsymbol{n} \cdot (\boldsymbol{u} - \boldsymbol{u}_b)(\boldsymbol{x}' \times \boldsymbol{\gamma}_s), \tag{1.42}$$

where the flux velocity $\boldsymbol{n} \cdot (\boldsymbol{u} - \boldsymbol{u}_b)$ is fully determined by the Kutta condition.

The same comment can be addressed to the third integral in the right hand side of Eq. (1.41) which in turn becomes

$$\boldsymbol{n} \cdot (\boldsymbol{u} - \boldsymbol{u}_b)[\boldsymbol{x}' \times (\boldsymbol{x}' \times \boldsymbol{\gamma}_s)]. \tag{1.43}$$

1.6 Notes on numerical methods

The numerical framework is built using the *julia* programming language [5] for its speed and ease of implementation.

Every integral, whether involved in enforcing the non-penetration of the body or in determining the hydrodynamic loads, is computed analytically. Indeed, the discretized surface integrals can always be reduced to a sum of one dimensional integrals linked with each panel, the integrand of which is cast into the local frame of reference of the panel. These integrands are for the most part polynomial functions and in the worst case scenario combinations of polynomials, log and $\arctan$ functions with a well-known antiderivative. Their treatment is given a more thorough analysis in Appendices A.1 and A.3.

The ambient vorticity shed behind the body is advected using a Runge-Kutta 4 (RK4) integration scheme and so is the position of the distal extremity of the trailing uniform panel. This particular choice of integrator is justified by the absence of dissipation in the model and the large overlap of the imaginary axis by the stability region of the RK4 scheme.

As stated in Section 1.4, the end of a time step is characterized by the coalescence of the shed uniform panel into a point vortex. This phenomenon results into a dimension reduction from a linear system of size $N_p + 2$ of Eq. (1.30) to the smaller system of size $N_p + 1$ (see Eq. (1.31)) where the unsteady Kutta condition is voided. To avoid unnecessary computations, we use the Sherman-Morrison-Woodbury formula [61] to quickly determine the inverse of the matrix after a 1-rank reduction.

At initiation of a simulation, the prescribed initial body kinematics are used for the body placement while the average length of the panels composing its surface determines the length of the trailing panel $2b_s$, oriented in the direction of the bisector of the trailing edge wedge. The bound vorticity is solved for in this initial configuration in order to determine the initial momentum as well as potential and pressure distributions on surface $\mathcal{S}_b$. Then, time marching starts and the whole sequence of events composing a RK4 temporal substep is as follows: the velocity and position of the body are updated with the knowledge of the imposed kinematics. The constellation of vortices is advected by the free flow. Using the shedding direction β from the previous temporal substep, the positioning of the shed uniform panel is determined through time integration of the average flow velocity computed on both sides of the trailing edge. Bound vorticity is computed as well as the new shedding direction β. This internal procedure is repeated for the four substeps. Then, at the end of the entire RK4 time step, the trailing panel coalesces into a point vortex and the reduced linear system is solved. Finally, hydrodynamic force and moment are determined. Pseudocode for the whole procedure is given in Algorithm 1 where `RK4Proc()` is the standard RK4 integration procedure.

Input:
Acceleration function $\mathbb{R} \to \mathbb{R}^3 : t \mapsto f_x(t) = [\ddot{x}_{cm}, \ddot{y}_{cm}, \ddot{\theta}]^T$
Simulation and geometric parameters $\mathscr{P}$
Result:
Runs the simulation
Procedure `run_flow_model(`$f_x, \mathscr{P}$`)`
$(\Delta t, T) \leftarrow \mathscr{P}$
$t := 0$
Initialize surface $(\boldsymbol{x}, \boldsymbol{u}_b) \leftarrow \mathscr{P}$
Initialize trailing panel $\mathcal{S}_u \leftarrow (b_s, \beta) \leftarrow \mathscr{P}$
Initialize vortex sheet set $\mathcal{S}_s = \mathcal{S}_v \cup \mathcal{S}_u = \mathcal{S}_u$
Solve linear system for $(\boldsymbol{\gamma}, \gamma_s) \leftarrow (\mathcal{S}_s, \boldsymbol{x}, \boldsymbol{u}_b)$
Compute hydro. loads and pressure $(\boldsymbol{f}, \boldsymbol{m}_{\boldsymbol{x}_{cm}}, p) \leftarrow (\boldsymbol{\gamma}, \mathcal{S}_s, \boldsymbol{x}, \boldsymbol{u}_b)$
Procedure `updateProc(`t`)`
Update acceleration $\ddot{\boldsymbol{x}} := f_x(t)$
Update surface $(\boldsymbol{x}, \boldsymbol{u}_b) \leftarrow (\ddot{\boldsymbol{x}})$
Update free vortex sheet $\mathcal{S}_v \leftarrow (\boldsymbol{\gamma}, \mathcal{S}_s, \boldsymbol{x}, \boldsymbol{u}_b)$
Create uniform panel at TE $(\mathcal{S}_u, \gamma_s) \leftarrow (\boldsymbol{\gamma}, \mathcal{S}_s, \boldsymbol{x}, \boldsymbol{u}_b, \beta)$
Solve linear system for $(\boldsymbol{\gamma}, \gamma_s) \leftarrow (\mathcal{S}_s, \boldsymbol{x}, \boldsymbol{u}_b)$
Compute shedding direction $\beta \leftarrow (\boldsymbol{\gamma})$
end
while $t < T$ **do**
`RK4Proc(`$x \to$ `updateProc(`x`)`, t, Δt`)`
Coalesce trailing panel into new point vortex of $\mathcal{S}_s$
Solve linear system for $\boldsymbol{\gamma} \leftarrow (\mathcal{S}_s, \boldsymbol{x}, \boldsymbol{u}_b)$
Compute hydro. loads and pressure $(\boldsymbol{f}, \boldsymbol{m}_{\boldsymbol{x}_{cm}}, p) \leftarrow (\boldsymbol{\gamma}, \mathcal{S}_s, \boldsymbol{x}, \boldsymbol{u}_b)$
$t := t + \Delta t$
end
end

Algorithm 1: Pseudocode for the unsteady flow solver for rigid bodies with prescribed kinematics.

1.7 Validation with rigid airfoils

This Section assesses the flow model described in the previous Sections of this Chapter. The gradual validation of the model starts with simple benchmarks: (i) an impulsively started NACA0012 airfoil and (ii) heaving and pitching NACA0012 and NACA0013 airfoils. The results obtained are compared to theories of Wagner [73] and Theodorsen [65], to the simulations of Xia and Mohseni [80] and to the experimental results from Izraelevitz and Triantafyllou [29] and Anderson et al. [1]. In all simulations, the airfoil of chord c, towed at horizontal velocity U_∞, is uniformly discretized with $N_p = 200$ panels of linear vortex strength and a time step $\Delta t = 10^{-2} c/U_\infty$ is used. Both the fluid and the body have unit density $\rho = 1[\text{kg/m}^3]$. The Gaussian regularization kernel is used with a cut-off width $\delta = 10^{-2} c$.

1.7.1 Impulsively started NACA0012

We run the simulation at an angle of attack $\alpha = \pi/18$ and show four snapshots at different times in Fig. 1.5.

(a) $tU_\infty/c = 1$

(b) $tU_\infty/c = 2$

(c) $tU_\infty/c = 5$

(d) $tU_\infty/c = 10$

Figure 1.5: Impulsively started NACA0012 airfoil at $\alpha = \pi/18$.

In Fig. 1.6, the hydrodynamic coefficients defined as $C_D = -2 f_x (\rho U_\infty^2 c)^{-1}$, $C_L = 2 f_y (\rho U_\infty^2 c)^{-1}$ and $C_{M,1/4} = 2 m_{\boldsymbol{x}_{1/4}} (\rho U_\infty^2 c^2)^{-1}$ are presented, $\boldsymbol{x}_{1/4}$ being the quarter-chord and towing-point of the airfoil. They are obtained with all three methods described in Section 1.5. Their difference is of the order of 10^{-2}, which is significant compared to the amplitudes of the drag and moment coefficients but represents less than 1% of the lift coefficient. It is safe to assume that this small mismatch will lose its significance for kinematics involving translations in the direction perpendicular to the midline of the airfoil or pitching motions of reasonable amplitudes.

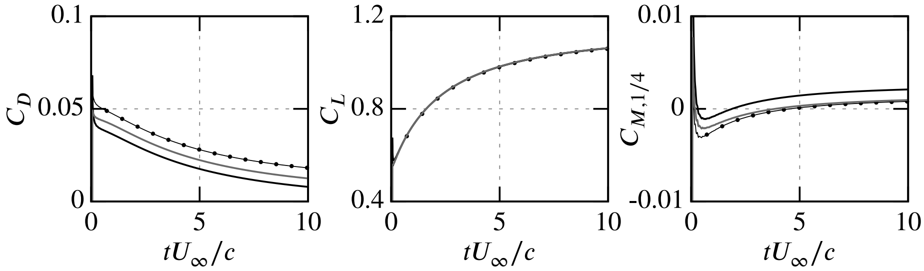

Figure 1.6: Impulsively started NACA0012 airfoil at $\alpha = \pi/18$. Aerodynamic coefficients computed with the impulse budget (—), the control volume approach (—) and the pressure distribution (-•-).

Fig. 1.7 shows the scaled lift coefficient derived from the pressure distribution as well as the scaled bound circulation for three angle of attacks and compares them to the theoretical Wagner function. Results are in good agreement with the Wagner function regardless of the angle of attack.

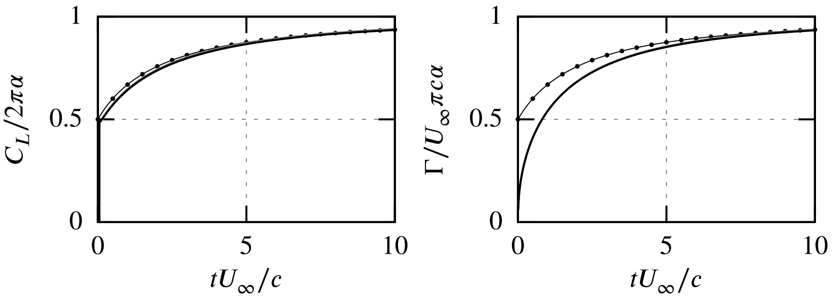

Figure 1.7: Impulsively started NACA0012 airfoil. Scaled lift coefficient and bound circulation at $\alpha = \pi/90$ (—), $\alpha = \pi/30$ (—) and $\alpha = \pi/18$ (—). Comparison with the Wagner function (-•-).

Fig. 1.8 presents the pressure coefficient distributed along the chord of the airfoil. On the left panel, we see that longer simulation times translate into a larger suction close to the leading edge. However, the right panel of the Figure, which displays the distribution of a steady panel method, shows the difficulty of our model to converge to the steady distribution. Increasing further the horizon time has only a limited influence on the amplitude of the downward peak and does not close the gap in a significant way. We let to any patient numerical practitioner the opportunity to study the behaviour of this discrepancy for very long simulation horizons.

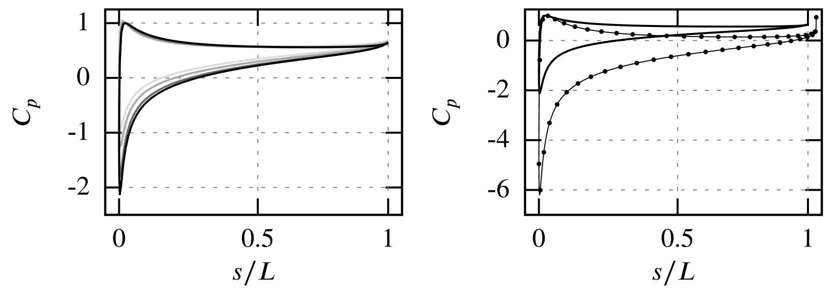

Figure 1.8: Impulsively started NACA0012 at $\alpha = \pi/18$. Distribution of the pressure coefficient on the body surface. Comparison between different times: $tU_\infty/c = 1$ (——), $tU_\infty/c = 2$ (——), $tU_\infty/c = 5$ (——) and $tU_\infty/c = 10$ (——) (left) and between $tU_\infty/c = 10$ (——) and a steady panel method (–•–) (right).

Finally, results of simulations performed at various angles of attack are compared with the simulations of Xia and Mohseni [80] in Fig. 1.9. For any configuration, the lift coefficient agrees well with their model. As expected, the shedding angle converges towards the bisector of the trailing edge. However, this occurs at a slower rate than what Xia and Mohseni [80] observed.

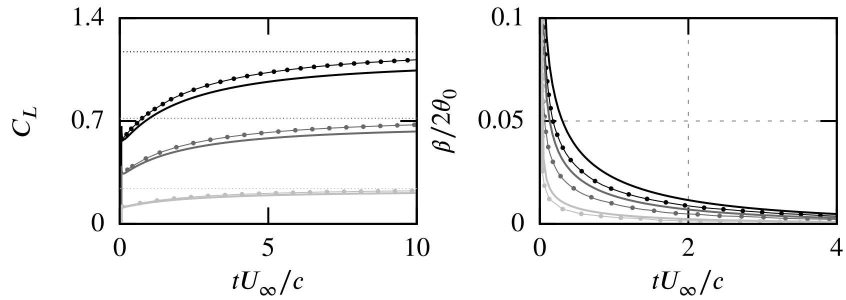

Figure 1.9: Impulsively started NACA0012 airfoil at $\alpha = \pi/90$ (——), $\alpha = \pi/30$ (——) and $\alpha = \pi/18$ (——). Lift coefficient and shedding angle of our model (——) and results of Xia and Mohseni [80] (–•–) along with steady values obtained with a steady flow model (······). Shedding angle β is defined with respect to the bisector of the trailing edge; $\beta \in [-\theta_0, \theta_0]$.

1.7.2 Heaving and pitching NACA0012 and NACA0013

This Section focuses on the study of airfoils undergoing vertical heaving and pitching motion while being towed horizontally with a constant velocity U_∞. The heaving motion is given by

$$y(t) = hc\cos(\omega t), \tag{1.44}$$

while the trajectory of the pitch angle $\theta(t)$ will be case dependent.

Before running any experiment, we define the reduced frequency as

$$\kappa = \frac{\omega c}{2U_\infty}, \tag{1.45}$$

and the Strouhal number – linking the heaving amplitude to the frequency – as

$$St = \frac{\omega hc}{\pi U_\infty} = \frac{2h\kappa}{\pi}. \tag{1.46}$$

Low amplitude motion

We begin by validating our model using the linear theory of Theodorsen [65] for flat plates undergoing oscillatory motion of small amplitude. We define the trajectory of the pitch angle as

$$\theta(t) = \theta_0\cos(\omega t + \psi), \tag{1.47}$$

where we set $\psi = \pi/2$, i.e. the pitching motion leads the heaving motion. The reduced frequency to $\kappa = 1$, the pivot point is the quarter-chord of the airfoil and we set the amplitudes to $h = 1/40$ and $\theta_0 = \{\pi/72, \pi/36, \pi/18\}$.

Fig. 1.10 shows snapshots of these simulations at convective time $tU_\infty/c = 5$. If the drag coefficient of a flat plate is 0 under the hypothesis of small amplitude oscillatory motion, it is not the case for the other aerodynamic coefficients. Lift and moment coefficients are presented on Fig. 1.11 along with their theoretical values using the model of Theodorsen [65]. It shows very good agreement between our model and theory. However, as the pitch amplitude increases and as the validity of the small amplitude hypothesis becomes ambiguous (at $\theta_0 = \pi/18$), discrepancies appear between the obtained results and the theory: the theoretical linear dependency on the amplitude of the results starts to fail at explaining the dynamics of the actual flow.

Fig. 1.12 shows the difference in lift and moment coefficient between the different methods of computation for the largest pitching amplitude $\theta_0 = \pi/18$. Both coefficients obtained with either the momentum budget or the control volume approaches show a maximal difference with coefficients obtained using the integration of the pressure distribution of 1% of their amplitude.

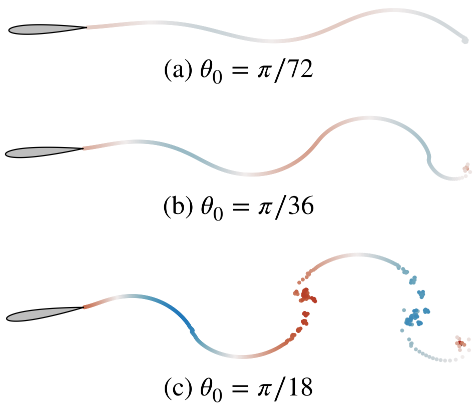

Figure 1.10: Heaving and pitching NACA0012 airfoil towed at its quarter-chord with $\kappa = 1$, $h = 1/40$ at $tU_\infty/c = 5$.

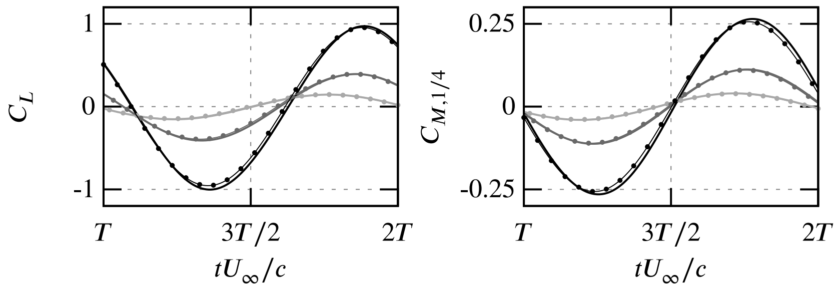

Figure 1.11: Heaving and pitching NACA0012 airfoil towed at its quarter-chord with $\kappa = 1$, $h = 1/40$ and $\theta_0 = \pi/72$ (—), $\theta_0 = \pi/36$ (—) and $\theta_0 = \pi/18$ (—). Lift and moment coefficients compared to the theoretical model of Theodorsen [65] (—•—).

High amplitude

We now switch to settings with higher amplitudes of motion. Under these circumstances, no mathematical model can elucidate the dynamics of the flow and numerical or experimental data become necessary.

We start by comparing our model to experimental results of Anderson et al. [1]. In their work, they towed a NACA0012 wing in a water tank at various motion parameters and compared the effect of the Strouhal number on the produced thrust coefficient and the associated thrust efficiency.

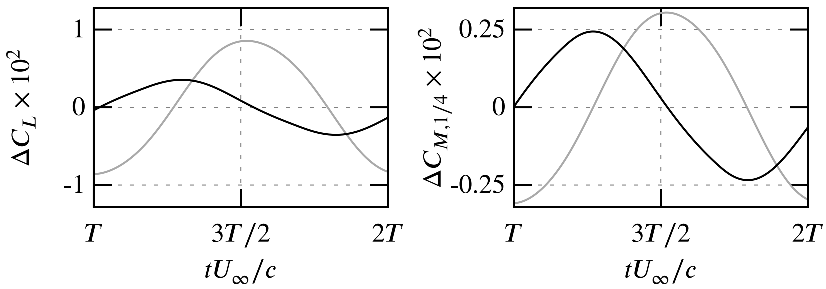

Figure 1.12: Heaving and pitching NACA0012 airfoil towed at its quarter-chord with $\kappa = 1$, $h = 1/40$ and $\theta_0 = \pi/18$. Difference between lift and moment coefficients obtained with the pressure distribution and the impulse budget (——) or the control volume approach (——).

To compare our model to their results, we used the same kinematics as in the previous experiment with $h = 0.75$ and a series pitch amplitudes θ_0 deduced each from an approximate maximum *effective* angle of attack α_0 at the towing point given by

$$\alpha_0 = \arctan\left(\frac{\omega h c}{U_\infty}\right) - \theta_0. \tag{1.48}$$

We set $\alpha_0 = \{\pi/36, \pi/18, \pi/9\}$ and the pivot point is located at $c/3$. We run simulations at different regimes where $\mathcal{S}t \in [0.1, 0.5]$ with a step of 0.1.

Results of thrust coefficient $C_T = -C_D$ and thrust efficiency:

$$\eta = \frac{C_T U_\infty}{\frac{1}{T}\int_{t-T}^{t}\left(C_L \frac{\mathrm{d}y}{\mathrm{d}t} + C_{M,1/3}\frac{\mathrm{d}\theta}{\mathrm{d}t}\right)\,\mathrm{d}\tau}, \tag{1.49}$$

– derived from the pressure coefficients – are shown on Fig. 1.13 and compared to the results of Anderson et al. [1]. They suggest an agreement in thrust between simulation and experiment until higher values of $\mathcal{S}t$ when the value of α_0 is larger. They show that our model looks to perform quite well until $\mathcal{S}t = 0.4$ where the relative spread between simulation and experiment gets larger as the value of α_0 decreases. The absence of viscous drag in our framework might justify this behaviour. Additionally, for higher $\mathcal{S}t$ values, we suspect the appearance of a leading edge vortex separating from the airfoil before reaching the trailing edge which may or may not interact with the wake and disrupt the vorticity pattern. Such separation can not be represented by our framework in which the Reynolds number is considered infinite. As far as the thrust efficiency is concerned, our framework also agrees better with experimental data when α_0 is large. However, higher Strouhal number do not appear to hinder the results, meaning that in our simulations, the energy necessary for the actuation also overshoots what was required in the water-tank experiments with higher $\mathcal{S}t$. When $\mathcal{S}t$ is low, the efficiency reported by our model overshoots experimental data, this behaviour is once again caused by the absence of viscous drag on the airfoil in our framework.

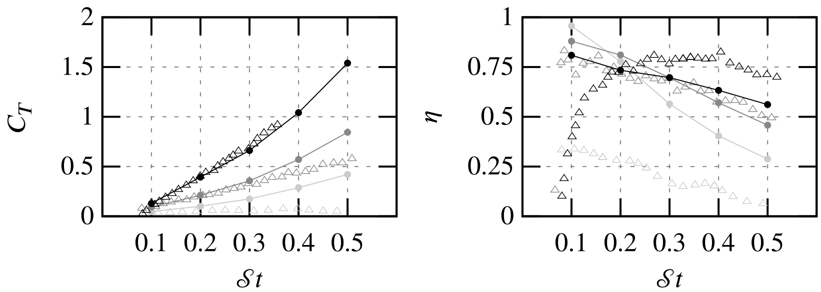

Figure 1.13: Heaving and pitching NACA0012 airfoil towed at its third-chord with $h = 0.75$, $\alpha_0 = \pi/36$ (—), $\alpha_0 = \pi/18$ (—) and $\alpha_0 = \pi/9$ (—). Thrust coefficient and efficiency as a function of the Strouhal number. Comparison with experimental data of Anderson et al. [1] (Δ).

Izraelevitz and Triantafyllou [29] argued that experiments performed in [1] were not representative of what was observed in the realm of biolocomotion and were the product of experimentalists only. Indeed, with these motion parameters, the effective angle of attack is altered under the effect of the arctan term in Eq. (1.48), accounting for the relative incoming flow velocity seen by the airfoil. For large Strouhal numbers, this term produces a significant increase in both the effective frequency and amplitude of the angle of attack, deviating from the target parameters ω and α_0. This effect is shown in Fig. 1.14 for $h = 0.75$, $\alpha_0 = \pi/36$ and different Strouhal numbers. In this case, the overshoot in maximal angle of attack represents 150% of α_0 at $\mathcal{S}t = 0.5$. For higher values of α_0, the relative size of the overshoot at studied particular Strouhal numbers is much less significant and the actual maximal angle of attack of all experiments never exceeds $5\pi/36$. To avoid these difficult to predict and undesirable effects, they suggested instead to directly impose the trajectory of the angle of attack $\alpha(t)$ and ran experiments using the same experimental apparatus as Anderson et al. [1]. We now reproduce one of these experiments which has also been simulated in [80] to compare their results to our model.

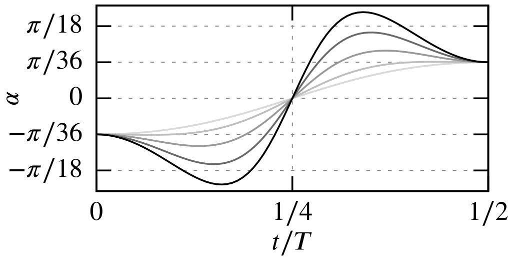

Figure 1.14: Heaving and pitching NACA0012 airfoil towed at its third-chord with $h = 0.75$ and $\alpha_0 = \pi/36$. Effect of the Strouhal number on the effective angle of attack at the towing point. $\mathcal{S}t$ is increased from 0.1 (—) to 0.5 (—) with steps of 0.1.

We consider a NACA0013 airfoil towed at its quarter-chord such that the relative angle of attack is the sinusoid:

$$\alpha(t) = \theta(t) - \arctan\left(\frac{\dot{y}(t)}{U_\infty}\right) = \alpha_{\max}\sin(\omega t). \tag{1.50}$$

The motion parameters are parameters: $h = 1$, $\alpha_{\max} = 5\pi/36$ and $St = 0.3$. In this situation, Izraelevitz and Triantafyllou [29] have experimentally shown the absence of leading edge separation at Reynolds number of 11000 which makes this set up an ideal candidate for our framework.

In Fig. 1.15, we present the hydrodynamic coefficients computed with all three methods proposed in Section 1.5. They once again result in macroscopically similar loads, with a difference smaller than 1% of the drag/lift coefficient amplitudes and of about 4% of the maximum value of the moment coefficient. This is visible in Fig. 1.16 where we show the difference between coefficients obtained from the pressure distribution (see Eq. (1.32)) and the two other methods, namely the impulse budget of Eq. (1.36) and the control volume approach of Eqs. (1.40) and (1.41). The figure also suggests that the difference between any pair of methods has the same order of magnitude, which indicates that any method is comparable to the others. Snapshots of the simulation appear in Fig. 1.17.

We then compare the hydrodynamic coefficients with computational results of Xia and Mohseni [80] and Izraelevitz and Triantafyllou [29] in Fig. 1.18. They display a good agreement between both simulation frameworks whereas experimental data, although presenting a similar trend, match more loosely. We remark an overshoot in

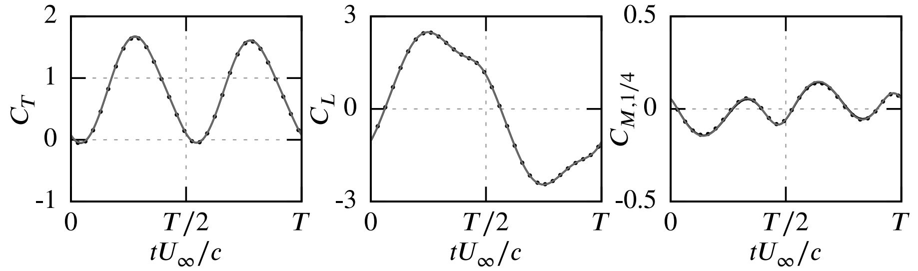

Figure 1.15: Heaving and pitching NACA0013 airfoil towed at its quarter-chord with $St = 0.3$, $h = 1$ and $\alpha_{max} = 5\pi/36$. Aerodynamic coefficients computed with the impulse budget (—), the control volume aproach (—) and the pressure distribution (-•-).

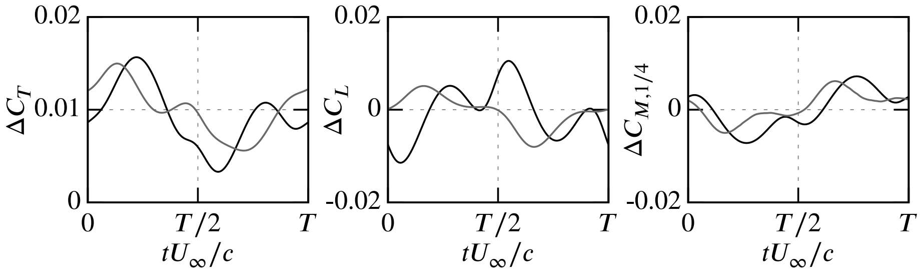

Figure 1.16: Heaving and pitching NACA0013 airfoil towed at its quarter-chord with $St = 0.3$, $h = 1$ and $\alpha_{max} = 5\pi/36$. Difference between aerodynamic coefficients obtained with the pressure distribution and the impulse budget (—) or the control volume approach (—).

thrust amplitude by both presented numerical frameworks compared to the experimental data. This is again is the result of the absence of viscous friction in both models.

Finally, we give the evolution of the shedding direction β and compare it to the computational reference in Fig. 1.19. If the trend is similar, the amplitude obtained with our model is approximately 25% smaller than the reference. The authors of the latter have provided no information on their discretization strategy which might be the reason of this mismatch. Indeed, what happens near the trailing edge and particularly the direction of shedding is very sensitive to the discretization choice in that region.

1.8 Discussion

This chapter presented a flow model for unsteady simulations of rigid airfoils presenting a trailing edge of finite-angle. The model is based on discretization of the flow into vortex elements such that the bound vorticity is restricted to an infinitely thin layer surrounding the immersed body and separates at the trailing edge. This separation releases ambient vorticity in the flow under the form of singular point vortices that are then advected under the laws of vortex dynamics. The mathematical foundations to build the model were provided as well as tools for post-processing including developments for surface pressure and three different methods enabling the computation of aerodynamic loads.

After successfully comparing the model to theoretical models, experimental data and a similar numerical framework found in the literature, we draw the conclusion that our model suitably represents the vortical structures shed by elongated bodies when no leading edge separation takes place. Under these circumstances, it can be applied to the study of more complex phenomena such as the locomotion of flexible bodies undergoing undulatory deformation.

(a) $tU_\infty/c = 1$

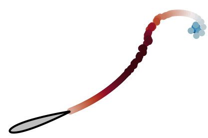

(b) $tU_\infty/c = 2$

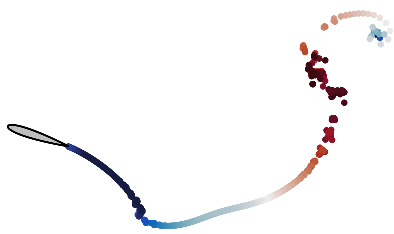

(c) $tU_\infty/c = 5$

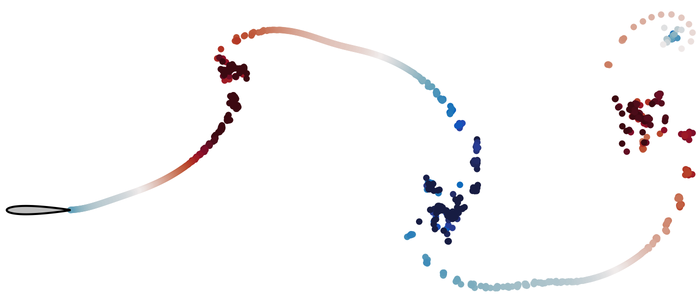

(d) $tU_\infty/c = 10$

Figure 1.17: Heaving and pitching NACA0013 airfoil towed at its quarter-chord with $St = 0.3$, $h = 1$ and $\alpha_{max} = 5\pi/36$.

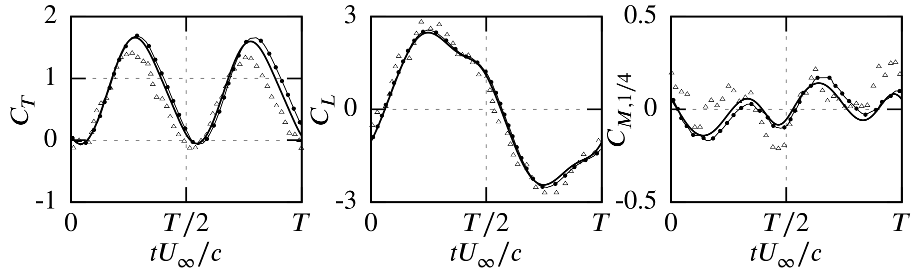

Figure 1.18: Heaving and pitching NACA0013 airfoil towed at its quarter-chord with $St = 0.3$, $h = 1$ and $\alpha_{max} = 5\pi/36$. Aerodynamic coefficients of our model (—), computational results of Xia and Mohseni [80] (–•–) and experimental data measured by Izraelevitz and Triantafyllou [29] (Δ).

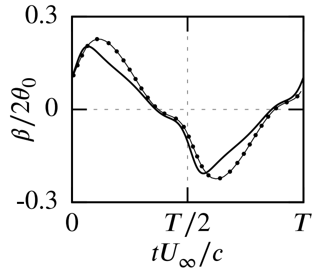

Figure 1.19: Heaving and pitching NACA0013 airfoil towed at its quarter-chord with $St = 0.3$, $h = 1$ and $\alpha_{max} = 5\pi/36$. Shedding angle between for our model (—) and the reference model of Xia and Mohseni [80] (–•–).

CHAPTER 2

Self-propelled swimmers

We now expand the model proposed in Chapter 1 to account for mass conserving body deformation and self-propulsion in the aim of applying this extension to undulatory swimming gait of anguilliform bodies.

This Chapter is structured as follows: section Section 2.1 presents the added mass: why it matters and how to derive its expression. Then we introduce a simple swimmer design involving a set of ellipses in Section 2.2. It has the advantage of simplifying the simulation framework and enabling validation with data found in literature. In Section 2.3, we focus on the model for a single continuous swimmer. After a quick comparison with similar experiments with higher-fidelity CFD models, maneuvering strategies are presented as well as effect of external perturbations. Finally, we study the kinematics of small schools of fish in Section 2.4.

2.1 On added mass and stabilization

As a preamble to this Chapter, we provide a few words on *added mass*. This corresponds to the mass of fluid reacting to the acceleration of an immersed body. It is formulated as an inertia matrix and is referred to as *added* or *virtual* mass or inertia. For the avid reader, [17, 32, 48, 18] all provide very relevant information about added mass in the case of single, multiple or articulated bodies.

This concept can be fully described by potential flow theory and for specific shapes like ellipses, analytic expressions exist. However, we here present a development for a self-propelling entity with 3 degrees of freedom intrinsic to the group of rigid motions in $\mathbb{R}^2$, namely two planar translations and a rotation around the out-of-plane direction. In addition, we consider a unitary fluid density ($\rho = 1[\text{kg/m}^3]$).

2.1.1 An expression for the added mass

We begin by decomposing the velocity potential as a linear combination of basis potentials $\boldsymbol{\zeta}$ and χ due to translational and rotational motions, respectively:

$$\varphi(\boldsymbol{x}) = \dot{\boldsymbol{x}}_{cm} \cdot \boldsymbol{\zeta}(\boldsymbol{x}) + \Omega\chi(\boldsymbol{x}) \tag{2.1}$$

where $\dot{\boldsymbol{x}}_{cm}$ and Ω are the three velocity components necessary to fully determine the rigid motion of the body.

If we recall the no-flow-through boundary condition on the body surface:

$$\nabla\varphi(\boldsymbol{x}) \cdot \boldsymbol{n} = \boldsymbol{u}(\boldsymbol{x}) \cdot \boldsymbol{n} = \boldsymbol{u}_b(\boldsymbol{x}) \cdot \boldsymbol{n}, \tag{2.2}$$

where $\boldsymbol{x} \in \mathscr{S}_b$, we can use decomposition Eq. (2.1) to specify it by means of the three degrees of freedom of the rigid motion:

$$\nabla\varphi \cdot \boldsymbol{n} = \frac{\partial\varphi}{\partial n} = \left(\dot{\boldsymbol{x}}_{cm} \cdot \frac{\partial\boldsymbol{\zeta}}{\partial n} + \Omega\frac{\partial\chi}{\partial n}\right) = \left(\dot{\boldsymbol{x}}_{cm} + \Omega\hat{\boldsymbol{e}}_z \times (\boldsymbol{x} - \boldsymbol{x}_r)\right) \cdot \boldsymbol{n}, \tag{2.3}$$

where we drop the dependency on $\boldsymbol{x}$ and where $\boldsymbol{x}_r$ is the center of rotation of the body.

Therefore, we can safely assume that:

$$\frac{\partial\boldsymbol{\zeta}}{\partial n} = \boldsymbol{n}, \tag{2.4}$$

$$\frac{\partial\chi}{\partial n} = [(\boldsymbol{x} - \boldsymbol{x}_r) \times \boldsymbol{n}] \cdot \hat{\boldsymbol{e}}_z, \tag{2.5}$$

using the identity: $(\boldsymbol{a} \times \boldsymbol{b}) \cdot \boldsymbol{c} = (\boldsymbol{b} \times \boldsymbol{c}) \cdot \boldsymbol{a}$.

After having defined the added mass matrix as the quadratic operator of the fluid kinetic energy in irrotational flows:

$$T_f(\boldsymbol{v}) = \frac{1}{2}\boldsymbol{v}^T \boldsymbol{M}_a \boldsymbol{v} = \frac{1}{2}\int_{\mathscr{V}_b} |\nabla\varphi|^2 \, \mathrm{d}V = -\frac{1}{2}\oint_{\mathscr{S}_b} \varphi\frac{\partial\varphi}{\partial n} \, \mathrm{d}S, \tag{2.6}$$

with $\boldsymbol{v} = [\dot{x}_{cm}, \dot{y}_{cm}, \Omega]^T$, we can determine the added mass tensors for the basis potentials:

$$M_{kl}^{\zeta\zeta} = -\oint_{\mathcal{S}_b} \zeta_l \frac{\partial \zeta_k}{\partial n} \, \mathrm{d}S = -\oint_{\mathcal{S}_b} \zeta_l \boldsymbol{n} \, \mathrm{d}S \cdot \hat{\boldsymbol{e}}_k, \tag{2.7}$$

$$M_{k}^{\zeta\chi} = -\oint_{\mathcal{S}_b} \chi \frac{\partial \zeta_k}{\partial n} \, \mathrm{d}S = -\oint_{\mathcal{S}_b} \chi \boldsymbol{n} \, \mathrm{d}S \cdot \hat{\boldsymbol{e}}_k, \tag{2.8}$$

$$M_{l}^{\chi\zeta} = -\oint_{\mathcal{S}_b} \zeta_l \frac{\partial \chi}{\partial n} \, \mathrm{d}S = -\oint_{\mathcal{S}_b} (\boldsymbol{x} - \boldsymbol{x}_r) \times \zeta_l \boldsymbol{n} \, \mathrm{d}S \cdot \hat{\boldsymbol{e}}_z, \tag{2.9}$$

$$M^{\chi\chi} = -\oint_{\mathcal{S}_b} \chi \frac{\partial \chi}{\partial n} \, \mathrm{d}S = -\oint_{\mathcal{S}_b} (\boldsymbol{x} - \boldsymbol{x}_r) \times \chi \boldsymbol{n} \, \mathrm{d}S \cdot \hat{\boldsymbol{e}}_z, \tag{2.10}$$

where $k, l \in \{x, y\}$ and use them to express the global added mass matrix:

$$\boldsymbol{M}_a = \begin{bmatrix} \boldsymbol{M}^{\zeta\zeta} & \boldsymbol{M}^{\zeta\chi} \\ \boldsymbol{M}^{\chi\zeta} & \boldsymbol{M}^{\chi\chi} \end{bmatrix}. \tag{2.11}$$

We can interpret the columns of the matrix in Eq. (2.11) as corresponding to the linear and angular momenta resulting from unitary translational or rotational motion of the body surface by noticing that on a closed surface in two dimensions,

$$\oint_{\mathcal{S}} \varphi \boldsymbol{n} \, \mathrm{d}S = -\oint_{\mathcal{S}} \boldsymbol{x} \times (\boldsymbol{n} \times \nabla\varphi) \, \mathrm{d}S, \tag{2.12}$$

and similarly, that

$$\oint_{\mathcal{S}} \boldsymbol{x} \times \varphi \boldsymbol{n} \, \mathrm{d}S = -\frac{1}{2} \oint_{\mathcal{S}} \boldsymbol{x} \times (\boldsymbol{x} \times (\boldsymbol{n} \times \nabla\varphi)) \, \mathrm{d}S. \tag{2.13}$$

This artifice is actually used to compute the added mass matrix without the need for the velocity potential on the body surface. Rather, for each of its possible configurations, the swimmer is artificially displaced with the three unitary velocities and the resulting linear and angular momenta computed with Eqs. (1.38) and 1.39 provide the elements of the added mass matrix.

Because kinetic energy is a quadratic form, $\boldsymbol{M}_a$ is symmetric positive semi-definite and so are its constituting tensors. This means that measuring component k of the impulse when displacing/rotating the body along/around $\hat{\boldsymbol{e}}_l$ is equivalent to measuring component l of the impulse when displacing/rotating the body along/around $\hat{\boldsymbol{e}}_k$.

2.1.2 Time integration with the added mass

This Chapter brings two major differences to the unsteady flow model presented in Chapter 1: the immersed body not only deforms but is now fully responsible for its own locomotion. In other words, the kinematics of its center of mass are not known anymore but result from the hydrodynamic loads the swimmer is submitted to because of its own deformation.

This means there is now some sensitive coupling between the fluid and body. This fluid-body interaction is governed by the dynamical system associated with Newton's second law of equilibrium:

$$\frac{\mathrm{d}}{\mathrm{d}t}\left(\boldsymbol{M}_b\dot{\boldsymbol{x}}_{cm}\right) = \boldsymbol{f}, \tag{2.14}$$

where $\boldsymbol{M}_b$ is the body mass matrix and $\boldsymbol{f}$ is the resultant of hydrodynamic forces applied on that point. However, the absence of any dissipation term in the system can make the integration of the swimmer dynamics challenging and requires a particular treatment. We note that the total hydrodynamic force on the body (obtained with any of the methods presented in Section 1.5) can be decomposed into two contributions:

$$\boldsymbol{f} = \boldsymbol{f}_v - \frac{\mathrm{d}}{\mathrm{d}t}\left(\boldsymbol{M}^{\zeta\zeta}\dot{\boldsymbol{x}}_{cm} + \boldsymbol{M}^{\zeta\chi}\Omega\right), \tag{2.15}$$

where $\boldsymbol{f}_v$ is the circulatory force and the second term is the force due to the added mass effect. This dichotomy allows to rewrite Eq. (2.14) as

$$\frac{\mathrm{d}}{\mathrm{d}t}\left(\left(\boldsymbol{M}_b + \boldsymbol{M}^{\zeta\zeta}\right)\dot{\boldsymbol{x}}_{cm} + \boldsymbol{M}^{\zeta\chi}\Omega\right) = \boldsymbol{f}_v; \tag{2.16}$$

the force contributions caused by the body acceleration are merged with the left hand side of Eq. (2.14). This in turn makes the time integration more tractable without interfering with the physical integrity of the equilibrium equation. More mathematical details on Eq. (2.16) as well as its extension accounting for the rotational equilibrium are provided in Appendix D. However, our framework is not designed with an easy procedure at hand for the isolation of the circulatory contribution to the hydrodynamic force and stabilization can be achieved in easier ways. Therefore, we suggest a workaround which stabilizes Eq. (2.14) through the introduction of numerical dissipation resulting from a semi-implicit treatment of the added mass contribution to the force.

We now have to introduce a few notations in order to regroup both linear and angular equilibria in the equilibrium equation. The extended force is defined as $\tilde{\boldsymbol{f}} = [f_x, f_y, l]^T$, the extended inertia matrix as $\tilde{\boldsymbol{M}}_b = [\boldsymbol{M}_b, \boldsymbol{0}; \boldsymbol{0}^T, I_b]$ and the global added mass matrix as $\boldsymbol{M}_a$. This latter matrix is computed according to Eq. (2.11), in the frame of reference following the center of mass of the swimmer, as the strategy presented in [17] suggests. The stabilization of Eq. (2.14) is achieved with the addition of $\boldsymbol{M}_a\dot{\boldsymbol{v}}^{n+1}$ to its left hand side and $\boldsymbol{M}_a\dot{\boldsymbol{v}}$ to its right hand side. It yields

$$(\boldsymbol{M}_a + \tilde{\boldsymbol{M}}_b)\dot{\boldsymbol{v}}^{n+1} = \tilde{\boldsymbol{f}} + \boldsymbol{M}_a\dot{\boldsymbol{v}} - \dot{\tilde{\boldsymbol{M}}}_b\boldsymbol{v}, \tag{2.17}$$

where the superscript refers to the next temporal sub-step while all other quantities are explicitly known at substep n. The last term of Eq. (2.17) is negligible in the case of small deformation. This hypothesis is crucial for the neutral buoyancy of the swimmer and the conservation of mass inside of $\mathscr{V}_b$. It is in practice valid in the forthcoming experiments.

2.2 An N-link swimmer

We start by experimenting on a quite simple toy problem where the swimmer is a set of articulated rigid bodies and sheds no vorticity in $\mathscr{V}_f$. This potential flow benchmark has the twofold advantage of first extending the model to locomotion without the complexity associated with vortex dynamics and of presenting reference from which one can replicate results.

2.2.1 Geometry and swimming gait

Let us consider a swimmer composed of a series of N articulated elliptic links. Each ellipse has length L and width e and is virtually attached to one or two rotoid articulations lying on its main axis at a distance d from either extremity. This design with $N = 3$ is presented in Fig. 2.1. In the rest of this manuscript, we will refer to this design as an N-link swimmer.

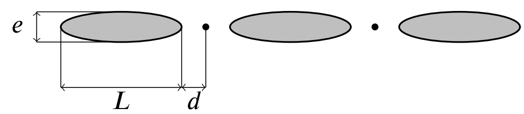

Figure 2.1: A 3-link swimmer composed of rigid ellipses at rest.

Considering a neutrally buoyant swimmer in a fluid of unitary density, ellipse i has mass $m_i = \frac{\pi}{4}Le$ and moment of inertia $I_i = \frac{\pi}{16}m_i(L^2 + e^2)$ defined around its center of mass $\boldsymbol{x}_i$ located at the intersection of its main axes.

The swimmer embeds $N+2$ degrees of freedom: $N-1$ internal ones corresponding to the relative angles θ_i, $\forall i = 2, ..., N$ between link i and $i-1$, and 3 external ones accounting for the position of the overall center of mass $\boldsymbol{x}_{cm}$ and the orientation of the first link θ_1. These are all shown in Fig. 2.2.

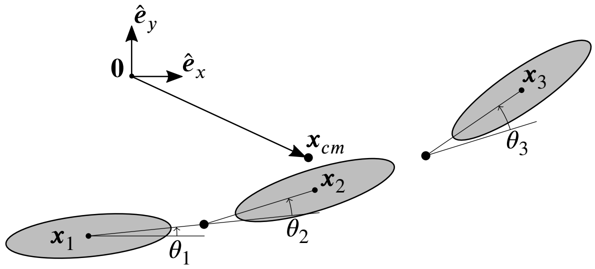

Figure 2.2: Parametrization of a 3-link swimmer.

This parametrization of the swimmer allows to retrieve the center of mass of every link with respect to the global center of mass:

$$\begin{aligned}
\boldsymbol{x}_1 &= \frac{1}{N}\left(\frac{1}{2}L+d\right)\left[(N-1)\boldsymbol{f}(1)+\sum_{j=2}^{N}(2N-2j+1)\boldsymbol{f}(j)\right],\\
\boldsymbol{x}_i &= \frac{1}{N}\left(\frac{1}{2}L+d\right)\left[\sum_{j=1}^{i-1}(2j-1)\boldsymbol{f}(j)+(2i-1-N)\boldsymbol{f}(i)+\sum_{j=i+1}^{N}(2j-1-2N)\boldsymbol{f}(j)\right],
\end{aligned} \tag{2.18}$$

where $i \in \{2, ..., N\}$ and $\boldsymbol{f}(j) = [\cos\sum_{k=1}^{j}\theta_k, \sin\sum_{k=1}^{j}\theta_k]^T$. On the other hand, the position of the i-th rotoid joint is simply:

$$\hat{\boldsymbol{x}}_i = \boldsymbol{x}_i + \left(\frac{1}{2}L+d\right)\boldsymbol{f}(i) \quad \forall i = 1, ..., N-1. \tag{2.19}$$

Eqs. (2.18) can actually be combined to obtain a formula for function $\mathbb{R}^N \to \mathbb{R}^{2\times N} : \boldsymbol{\theta} \mapsto \boldsymbol{X}(\boldsymbol{\theta})$ returning a matrix containing all centers of mass

$$\boldsymbol{X}(\boldsymbol{\theta}) = \frac{1}{N}\left(\frac{1}{2}L+d\right)\boldsymbol{F}(\boldsymbol{\theta})\boldsymbol{C}, \tag{2.20}$$

where the j-th column of $\boldsymbol{F}$ is $\boldsymbol{f}(j)$ and where we define

$$\boldsymbol{C} = \begin{bmatrix} 1-N & 1 & 1 & 1 & \dots & 1 & \dots & 1 \\ 3-2N & 3-N & 3 & 3 & \dots & 3 & \dots & 3 \\ 5-2N & 5-2N & 5-N & 5 & \dots & 5 & \dots & 5 \\ \vdots & \dots & \vdots & \ddots & \dots & \vdots & \dots & \vdots \\ (2i-1)-2N & \dots & (2i-1)-2N & & (2i-1)-N & 2i-1 & \dots & 2i-1 \\ \vdots & \dots & \dots & \dots & \dots & \ddots & & \vdots \\ -3 & \dots & -3 & \dots & \dots & -3 & N-3 & 2N-3 \\ -1 & \dots & -1 & \dots & \dots & -1 & -1 & N-1 \end{bmatrix}. \tag{2.21}$$

This formalism greatly reduces the amount of function evaluations and floating point operations in comparison to a more naive approach. This statement is especially true given the symmetry in the latter matrix: $C_{i,j} = -C_{N-i+1,N-j+1}$ which is computed only once.

As defined by Lighthill [42], any deformation of a swimmer in vacuum causes *recoil*. That is the rigid translational and rotational velocities required to conserve overall linear and angular momenta. Because the global center of mass is attached to the origin of the inertial frame of reference, there is no linear recoil. This is not the case for the angular position of the body. The correct angular velocity must be applied to the body $\dot{\theta}_1$ such that the total angular momentum is conserved regardless of the motion of the articulations and no spurious momentum is injected in the fluid-body system during the swimming motion. The global angular momentum due to the body deformation is given by

$$L_z = \sum_{i=1}^{N} \left(m_i \sum_{k=1}^{N} \left(x_i \frac{\partial y_i}{\partial \theta_k} - y_i \frac{\partial x_i}{\partial \theta_k} \right) \dot{\theta}_k + I_i \sum_{k=1}^{i} \dot{\theta}_k \right) = 0, \tag{2.22}$$

and by regrouping all factors of $\dot{\theta}_1$, we obtain

$$\dot{\theta}_1 = -\frac{\sum_{i=1}^{N} m_i \sum_{k=2}^{N} \left(x_i \frac{\partial y_i}{\partial \theta_k} - y_i \frac{\partial x_i}{\partial \theta_k} \right) \dot{\theta}_k + \sum_{i=2}^{N} I_i \sum_{k=2}^{i} \dot{\theta}_k}{\sum_{i=1}^{N} m_i \left(\left(x_i \frac{\partial y_i}{\partial \theta_1} - y_i \frac{\partial x_i}{\partial \theta_1} \right) \right) + N I_1}. \tag{2.23}$$

Provided trajectories of θ_i and $\dot{\theta}_i$, $\forall i = 2, ..., N$ are known, the time integration of $\dot{\theta}_1$ is used to obtain the new and corrected angular position θ_1 of the first link and hence, the entire chain.

2.2.2 Numerical methods

For these N-link swimmers involving only ellipses, there is no trailing edge with finite-angle from which vorticity can emerge in the flow. The flow surrounding the swimmer is purely irrotational and the numerical framework must be adapted accordingly to account for that major difference. Moreover, the body discretization is slightly different: the end of the last panel composing the surface of the ellipse matches with the position of the start of the first panel.

These changes result in a linear system to solve for the bound vorticity with $N \times N_p$ unknowns and $N \times (N_p + 1)$ constraints, namely the non-penetration condition on each panel along with Kelvin's conservation of circulation for each link. This over constrained linear problem is solved with a least-square approximation.

Additionally, the added mass is used to damp the dynamical system in the way described in Section 2.1.2. Time integration is performed once again with the standard RK4 scheme, for similar reasons as given in Section 1.6.

The pseudocode for this irrotational framework is presented in Algorithm 2 where we introduce the three degrees of freedom $\boldsymbol{q} = [x_{cm}, y_{cm}, \theta_1]^T$.

2.2.3 Validation and results

In this Section, the potential flow model is assessed on the results of Kanso et al. [32] where they simulate the displacement of a 3-link body. They discriminate two different sets of simulations: with and without inter-link hydrodynamic coupling. What they call coupling is how the motion of a given ellipse affects the equilibrium equation of the others. Given the definition of the added mass given in Section 2.1.1, there is no such coupling because our added mass only accounts for the rigid motion of the global articulated system. Hence, this Section focuses on replicating results for the *hydrodynamically decoupled* system.

We use a similar geometry with $L = 1$ and $e = d = 0.1L$. They start by imposing the following trajectories for the two actuated joints:

$$\theta_2(t) = -\sin t/T, \qquad \theta_3(t) = -\cos t/T. \tag{2.24}$$

Each ellipse is discretized with $N_p = 200$ panels using a Chebyshev distribution. The simulation parameters are $\Delta t = .01T/2\pi$ and $t_{max} = 3T$. Furthermore, the swimming motion is initiated from the configuration at rest depicted in Fig. 2.1 by multi-

Input:
Geometric parameters
$\mathbb{R}^n \to \mathbb{R}^{2,N\times N_p} : \boldsymbol{q} \mapsto f_x(\boldsymbol{q}) = \boldsymbol{x}$ where $\boldsymbol{x} \in \mathcal{S}_b$
$\mathbb{R}^n \times \mathbb{R}^n \to \mathbb{R}^{2,N\times N_p} : (\boldsymbol{q}, \dot{\boldsymbol{q}}) \mapsto f_u(\boldsymbol{q}, \dot{\boldsymbol{q}}) = \boldsymbol{u}_b$
Swimming gait $\mathbb{R} \to \mathbb{R}^{n-3} : t \mapsto f_s(t) = \boldsymbol{s}$
Simulation parameters $\mathscr{P}$
Result:
Runs the simulation
Procedure `run_potential_flow_model(`$f_x, f_u, f_s, \mathscr{P}$`)`
  $(\Delta t, T) \leftarrow \mathscr{P}$
  $t := 0$
  $(\boldsymbol{f}, \boldsymbol{m}_{\boldsymbol{x}_{cm}}) := (\boldsymbol{0}, \boldsymbol{0})$
  $(\boldsymbol{q}, \dot{\boldsymbol{q}}, \ddot{\boldsymbol{q}}) := (\boldsymbol{0}, \boldsymbol{0}, \boldsymbol{0})$
  Initialize surface $(\boldsymbol{x}, \boldsymbol{u}_b) \leftarrow (\boldsymbol{q}, \dot{\boldsymbol{q}})$
  Initialize added mass $\boldsymbol{M}_a \leftarrow \boldsymbol{x}$
  Procedure `updateProc(`t`)`
    Update deformation $\boldsymbol{s} := f_s(t)$
    Update $\ddot{\boldsymbol{q}} \leftarrow (\boldsymbol{f}, \boldsymbol{m}_{\boldsymbol{x}_{cm}}, \boldsymbol{s})$
    Update generalized coordinates $(\boldsymbol{q}, \dot{\boldsymbol{q}}) \leftarrow (\ddot{\boldsymbol{q}}, \boldsymbol{M}_a)$
    Update surface $(\boldsymbol{x}, \boldsymbol{u}_b) \leftarrow (\boldsymbol{q}, \dot{\boldsymbol{q}})$
    Update added mass $\boldsymbol{M}_a \leftarrow \boldsymbol{x}$
    Solve linear system for $\boldsymbol{\gamma} \leftarrow (\boldsymbol{x}, \boldsymbol{u}_b)$
    Compute hydrodynamic loads and pressure $(\boldsymbol{f}, \boldsymbol{m}_{\boldsymbol{x}_{cm}}, p) \leftarrow (\boldsymbol{\gamma}, \boldsymbol{x}, \boldsymbol{u}_b)$
  end
  while $t < T$ **do**
    `RK4Proc(`$x \to$ `updateProc(`x`)`, t, Δt`)`
    $t := t + \Delta t$
  end
end

Algorithm 2: Pseudocode for the unsteady potential flow solver for swimmers made of rigid articulated elliptoid segments.

plying the angles of the internal joints θ_2 and θ_3 with the sigmoid function

$$\sigma(t/\tau) = \frac{\exp\left(3\pi(2t/\tau - 1)\right)}{1 - \exp\left(3\pi(2t/\tau - 1)\right)}, \tag{2.25}$$

with $\tau = T/2\pi$. This sigmoid function is displayed on Fig. 2.3. This allows to smoothly increase the amplitude of deformation from 0 to 1 at the early stage of the simulation when $t < \tau$ and avoid propagating errors due to numerical derivatives. This initiation process is the only thing that differentiates our simulation from the reference.

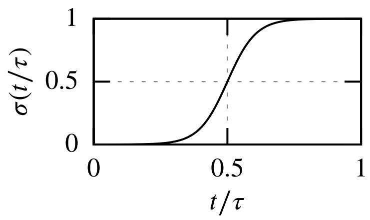

Figure 2.3: Sigmoid function used to initialize the swimming gait from a rest position.

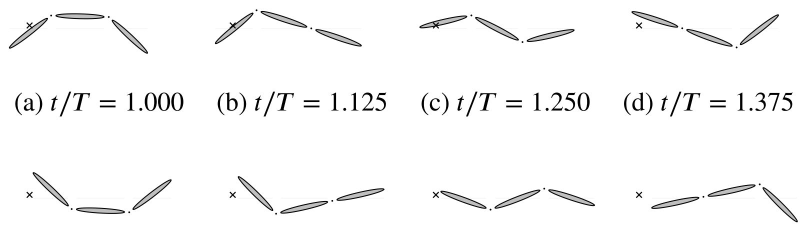

(a) $t/T = 1.000$ (b) $t/T = 1.125$ (c) $t/T = 1.250$ (d) $t/T = 1.375$

(e) $t/T = 1.500$ (f) $t/T = 1.625$ (g) $t/T = 1.750$ (h) $t/T = 1.875$

Figure 2.4: Snapshots of the swimming gait over one swimming period when $\theta_2(t) = -\sin t/T$ and $\theta_3(t) = -\cos t/T$. The origin of the inertial frame of reference is represented with $\times$.

Results are shown in Fig. 2.4 displaying snapshots during one swimming period and Fig. 2.5 where the trajectory of the center of mass and the angular position of the central segment of the swimmer are displayed. Because of the difference in initialization, we rotate the trajectory resulting from our framework to match best the cruise regime of the reference. Even though results do not exactly overlap, their difference is minor and we successfully retrieve the overall allure of the trajectory. The angle of the middle link closely matches the reference. One can observe the increasing character of the error as time marching is performed. In Fig. 2.6, we show the hydrodynamic loads propelling the swimmer.

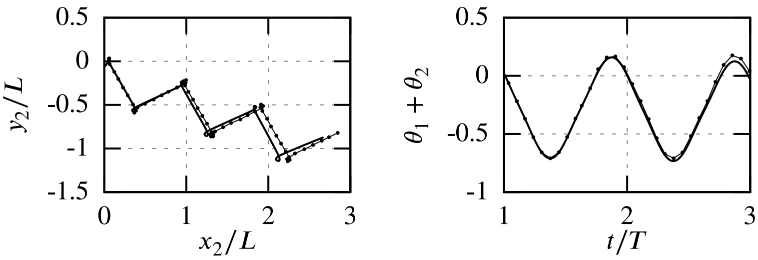

Figure 2.5: Trajectory of the center of mass (left) and evolution of the angle of the middle segment of the 3-link swimmer (right) when $\theta_2(t) = -\sin t/T$ and $\theta_3(t) = -\cos t/T$. Comparison of our model (—–) rotated to match Kanso et al. [32] (–•–).

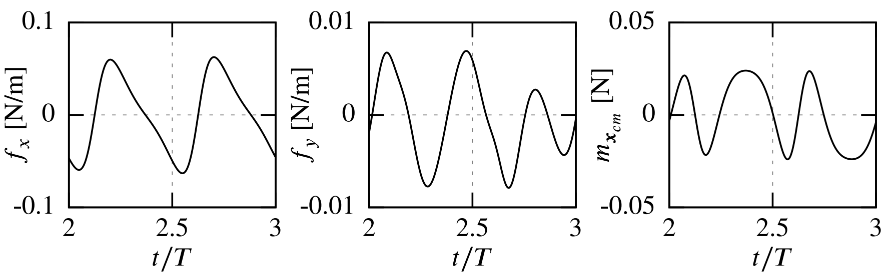

Figure 2.6: Hydrodynamic loads on the 3-link swimmer over one swimming period with imposed kinematics $\theta_2(t) = -\sin t/T$ and $\theta_3(t) = -\cos t/T$.

Another simulation is run with the imposed dynamics

$$\theta_2(t) = 1 - \sin t/T, \qquad \theta_3(t) = 1 - \cos t/T. \tag{2.26}$$

The main difference with the previous benchmark is an offset of 1 in the average actuation angle. The average curvature of the swimmer is positive and the swimmer is therefore expected to perform a turning maneuver to the left. Snapshots over a swimming period are shown in Fig. 2.7

All parameters of the simulation are identical. The trajectory and absolute angle of the middle link are shown in Fig. 2.8 where they are compared with [32]. The com-

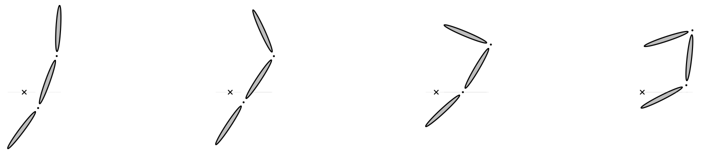

(a) $t/T = 1.125$ (b) $t/T = 1.250$ (c) $t/T = 1.375$ (d) $t/T = 1.500$

(e) $t/T = 1.625$ (f) $t/T = 1.750$ (g) $t/T = 1.875$ (h) $t/T = 2.000$

Figure 2.7: Snapshots of the swimming gait over one swimming period when $\theta_2(t) = 1 - \sin t/T$ and $\theta_3(t) = 1 - \cos t/T$. The origin of the inertial frame of reference is represented with ×.

parison highlights two already stated elements: the difference during the initialization phase and the scaling with elapsed time of the error in cruise regime.

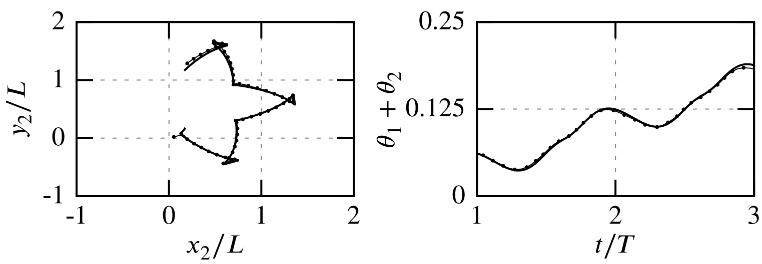

Figure 2.8: Trajectory of the center of mass (left) and evolution of the angle of the middle segment of the 3-link swimmer (right) when $\theta_2(t) = 1 - \sin t/T$ and $\theta_3(t) = 1 - \cos t/T$. Comparison of our model (—) rotated to match Kanso et al. [32] (–•–).

2.3 An anguilliform swimmer

We now go back to our original model with vortex shedding at the trailing edge of the body characterized by a finite-angle. The model is extended to account for self-propulsion of continuous flexible bodies of fish-like profile under undulatory deformation. The adequacy of our model to this application is supported by experiments of Triantafyllou et al. [66] and Eloy [19] where they characterized the optimal swimming regimes for different species of swimming animals. For most marine mammals, anguilliform and caranguiform fish species, they report optimal kinematics of the caudal fin and/or vortical patterns in the wake characterized by $\mathcal{S}t \in [0.25, 0.35]$, as summarized in Fig. 2.9.

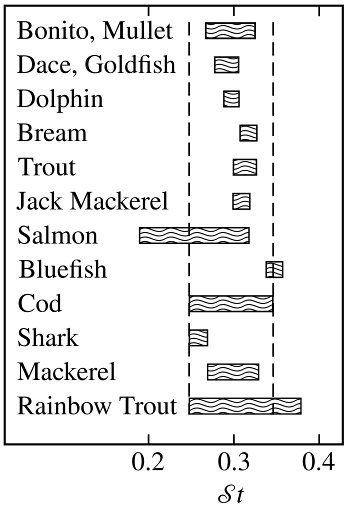

Figure 2.9: Range of Strouhal numbers of the caudal fin of different species in their optimal swimming regime.

The swimmer is now a connected volume $\mathcal{V}_b \subset \mathbb{R}^2$ composed of a series of trapezoidal links successively attached to one another. As the swimmer deforms, these links articulate and deform. We now present the methodology used to define mathematically both the body surface and its deformation.

2.3.1 Geometry and swimming gait

As performed by Gazzola et al. [22], the surface of the swimming body at rest is defined along the body-coordinate $s \in [0, L]$ by the half-thickness function

$$w(s) = \begin{cases} \sqrt{2w_h s - s^2}, & \text{if } 0 \leq s \leq s_b, \\ w_h - (w_h - w_t)\left(\frac{s-s_b}{s_t-s_b}\right), & \text{if } s_b < s \leq s_t, \\ w_t \frac{L-s}{L-s_t}, & \text{if } s_t < s \leq L, \end{cases} \tag{2.27}$$

where L is the body length, $w_h = s_b = 0.04L$, $s_t = 0.95L$ and $w_t = 0.01L$. The full thickness resulting from Eq. (2.27) and representing the body surface of the swimmer is shown in Fig. 2.10.

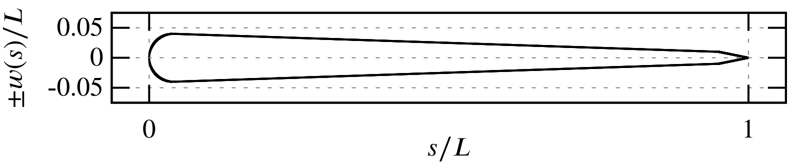

Figure 2.10: Thickness function used to determine the surface of a swimmer.

In this work as well as in the aforementioned references, the lateral displacement of the spine is imposed in a frame of reference attached to the head of the swimmer according to the following waveform

$$y_s(s,t) = \frac{L + 32s}{264} \sin\left(2\pi\left(\frac{s}{L} - \frac{t}{T}\right)\right). \tag{2.28}$$

This motion implies a wave speed $v = L/T$[m/s] through the spine of the swimmer. However, directly imposing the spine deformation makes the constraint of a constant body length L difficult to comply with numerically. On the other hand, imposing the curvature of the spine fully characterizes the deformation too and alleviates this issue. Its general expression is

$$\kappa_s(s,t) = \frac{\frac{\partial^2 y_s}{\partial s^2}}{\left(1 + \left(\frac{\partial y_s}{\partial s}\right)^2\right)^{3/2}}. \tag{2.29}$$

The integration along coordinate s from 0 to L of the Frenet-Serret [see 21] system of equations and their time derivatives provides one with the instantaneous position and velocity of the spine

$$\begin{cases} \frac{\partial \boldsymbol{t}}{\partial s} = \kappa_s \boldsymbol{n}, \\ \frac{\partial \boldsymbol{n}}{\partial s} = -\kappa_s \boldsymbol{t}, \\ \frac{\partial \boldsymbol{r}}{\partial s} = \boldsymbol{t}, \end{cases} \qquad \begin{cases} \frac{\partial \dot{\boldsymbol{t}}}{\partial s} = \dot{\kappa}_s \boldsymbol{n} + \kappa_s \dot{\boldsymbol{n}}, \\ \frac{\partial \dot{\boldsymbol{n}}}{\partial s} = -\dot{\kappa}_s \boldsymbol{t} - \kappa_s \dot{\boldsymbol{t}}, \\ \frac{\partial \dot{\boldsymbol{r}}}{\partial s} = \dot{\boldsymbol{t}}, \end{cases} \tag{2.30}$$

where $\boldsymbol{t}$, $\boldsymbol{n}$ and $\boldsymbol{r}$ are the tangent, normal and position vectors along the spine, respectively. The boundary conditions are $\boldsymbol{t}(0,t) = [1,0]^T$, $\boldsymbol{n}(0,t) = [0,1]^T$, $\boldsymbol{r}(0,t) = \dot{\boldsymbol{t}}(0,t) = \dot{\boldsymbol{n}}(0,t) = \dot{\boldsymbol{r}}(0,t) = [0,0]^T$.

This spine deformation defines an envelope shown in Fig. 2.11 where the vertical tail-beat amplitude is close to $0.16L$. Using this information and under the assumption that the regime velocity of the fish is close to its deformation wave speed, we find a Strouhal number $\mathcal{S}t = 0.32$ at the tail of the fish complying with experimental observations of [66] and within the range of validity of the simulation framework defined in the previous Chapter.

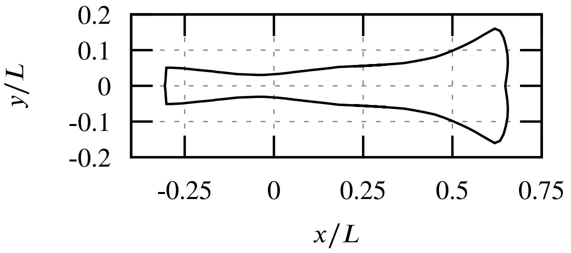

Figure 2.11: Amplitude enveloppe of the spine of a swimmer performing the deformation motion given in Eq. (2.28).

From the position and velocity of the spine, one can retrieve the position and velocity of the body surface $\mathcal{S}_b$ in the head-attached frame of reference

$$\boldsymbol{r}_{\mathcal{S}_b}(s) = \boldsymbol{r}(s) \pm w(s)\boldsymbol{n}(s), \tag{2.31}$$

$$\dot{\boldsymbol{r}}_{\mathcal{S}_b}(s) = \dot{\boldsymbol{r}}(s) \pm w(s)\dot{\boldsymbol{n}}(s). \tag{2.32}$$

This surface encloses the body volume $\mathcal{V}_b$ shown in Fig. 2.12 when the thickness defined by Eq. (2.27) and the periodic deformation of (2.28) are used to determine $\mathcal{S}_b$.

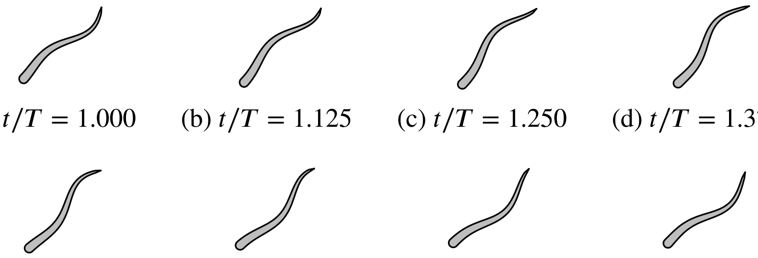

(a) $t/T = 1.000$ (b) $t/T = 1.125$ (c) $t/T = 1.250$ (d) $t/T = 1.375$

(e) $t/T = 1.500$ (f) $t/T = 1.625$ (g) $t/T = 1.750$ (h) $t/T = 1.875$

Figure 2.12: Swimming body over one deformation period.

Following [22], applying the recoil velocity correction is done first by a change of reference frame from the head to the instantaneous center of mass of the body

$$\boldsymbol{x}' = \boldsymbol{r}_{\mathcal{S}_b} - \boldsymbol{r}_{cm}, \tag{2.33}$$

$$\dot{\tilde{\boldsymbol{x}}}' = \dot{\boldsymbol{r}}_{\mathcal{S}_b} - \dot{\boldsymbol{r}}_{cm}, \tag{2.34}$$

where the position and velocity of the center of mass in the frame of reference attached to the head are

$$\boldsymbol{r}_{cm} = \frac{\int_{\mathcal{V}_b} \boldsymbol{y} \, \mathrm{d}V(\boldsymbol{y})}{\int_{\mathcal{V}_b} \mathrm{d}V(\boldsymbol{y})}, \tag{2.35}$$

$$\dot{\boldsymbol{r}}_{cm} = \frac{\int_{\mathcal{V}_b} \dot{\tilde{\boldsymbol{x}}}'(\boldsymbol{y}) \, \mathrm{d}V(\boldsymbol{y})}{\int_{\mathcal{V}_b} \mathrm{d}V(\boldsymbol{y})}. \tag{2.36}$$

Then by cancelling the angular momentum, yielding the surface velocity

$$\dot{\boldsymbol{x}}' = \dot{\tilde{\boldsymbol{x}}}' - \frac{\int_{\mathcal{V}_b} \boldsymbol{y} \times \dot{\tilde{\boldsymbol{x}}}'(\boldsymbol{y}) \, \mathrm{d}V(\boldsymbol{y})}{\int_{\mathcal{V}_b} |\boldsymbol{y}|^2 \, \mathrm{d}V(\boldsymbol{y})} \times \boldsymbol{x}', \tag{2.37}$$

in the frame attached to the center of mass. Thus, the body surface velocity expressed in the inertial frame of reference is

$$\boldsymbol{u}_b = \dot{\boldsymbol{x}}' + (\dot{\boldsymbol{x}}_{cm} + \Omega \hat{\boldsymbol{e}}_z \times \boldsymbol{x}'), \tag{2.38}$$

where $\dot{\boldsymbol{x}}'$ is a momentum-free deformation velocity and where the velocity terms $\dot{\boldsymbol{x}}_{cm}$ and Ω in equation (2.38) account for the rigid motion of the swimmer integrated from the hydrodynamic force and moment.

2.3.2 Numerical methods

The system of ODEs (2.30) is solved using the `ODE45` utility from the `DifferentialEquations.jl` [56] *julia* package.

Where an analytic integration is impossible (i.e. for volume integrals for which no surface integral can be obtained with Green's theorems) like in Eq. (2.37) or for computing the body mass, the position or the velocity of the center of mass, numerical integration is performed: the swimmer is discretized with N_p triangles on each of which a 25-point Gauss-Legendre integration scheme is applied.

The original framework with vortex shedding of Chapter 1 is now extended with the time integration of Newton's second law. The added mass is used in a similar way as in Section 2.1.2. The pseudocode is presented in Algorithm 3.

2.3.3 Convergence, comparison with CFD and other results

The spine of the fish is segmented in such a way to guarantee a uniform discretization over the surface of the body at rest, such that:

$$\Delta s(s) = \frac{2\int_0^L \sqrt{1+\left(\frac{\mathrm{d}w}{\mathrm{d}x}\right)^2}\mathrm{d}x}{N_p\sqrt{1+\left(\frac{\mathrm{d}w}{\mathrm{d}s}\right)^2}}. \tag{2.39}$$

We choose $N_p = 128$ resulting in an articulated system of 64 links and the time step is set to $\Delta t = 0.01T$. Other simulation parameters are $t_{max} = 12T$, $\delta = 0.01L$.

This choice results from a convergence analysis carried out using four different refinement levels, at a constant CFL number. The examined quantities are the integral over a swimming period of the overall energy spent in the actuators (see Chapter 3) of the swimmer as well as the moduli of its displacement and velocity. The absolute errors of these quantities are presented in Fig. 2.13 and their evolution is shown in Fig. 2.14. The order of convergence is approximately of $\mathcal{O}(\Delta t^{1.7})$ for energy, position and velocity and the selected set of parameters yields relative errors lying within a 2.5% margin with respect to the most refined solution at $t = T$.

We compare our framework with the data obtained by Kern and Koumoutsakos [34] using a commercial finite volume software for viscous simulations. Fig. 2.15 presents the tangential and normal components of the swimming velocity. For both components, it takes the swimmer approximately six full swimming periods to reach

Input:

Geometric parameters

$\mathbb{R}^n \to \mathbb{R}^{2,N_p+1} : \boldsymbol{q} \mapsto f_x(\boldsymbol{q}) = \boldsymbol{x}$ where $\boldsymbol{x} \in \mathcal{S}_b$

$\mathbb{R}^n \times \mathbb{R}^n \to \mathbb{R}^{2,N_p+1} : (\boldsymbol{q}, \dot{\boldsymbol{q}}) \mapsto f_u(\boldsymbol{q}, \dot{\boldsymbol{q}}) = \boldsymbol{u}_b$

Swimming gait $\mathbb{R} \to \mathbb{R}^{n-3} : t \mapsto f_s(t) = \boldsymbol{s}$

Simulation parameters $\mathscr{P}$

Result:

Runs the simulation

Procedure `run_flow_model`$(f_x, f_u, f_s, \mathscr{P})$

- $(\Delta t, T) \leftarrow \mathscr{P}$
- $t := 0$
- $(\boldsymbol{f}, \boldsymbol{m}_{\boldsymbol{x}_{cm}}) := (\boldsymbol{0}, \boldsymbol{0})$
- $(\boldsymbol{q}, \dot{\boldsymbol{q}}, \ddot{\boldsymbol{q}}) := (\boldsymbol{0}, \boldsymbol{0}, \boldsymbol{0})$
- Initialize surface $(\boldsymbol{x}, \boldsymbol{u}_b) \leftarrow (\boldsymbol{q}, \dot{\boldsymbol{q}})$
- Initialize added mass $\boldsymbol{M}_a \leftarrow \boldsymbol{x}$
- Initialize trailing panel $\mathcal{S}_u \leftarrow (b_s, \beta) \leftarrow \mathscr{P}$
- Initialize vortex sheet set $\mathcal{S}_s = \mathcal{S}_v \cup \mathcal{S}_u = \mathcal{S}_u$
- **Procedure** `updateProc`(t)
  - Update deformation $\boldsymbol{s} := f_s(t)$
  - Update $\ddot{\boldsymbol{q}} \leftarrow (\boldsymbol{f}, \boldsymbol{m}_{\boldsymbol{x}_{cm}}, \boldsymbol{s})$
  - Update generalized coordinates $(\boldsymbol{q}, \dot{\boldsymbol{q}}) \leftarrow (\ddot{\boldsymbol{q}}, \boldsymbol{M}_a)$
  - Update surface $(\boldsymbol{x}, \boldsymbol{u}_b) \leftarrow (\boldsymbol{q}, \dot{\boldsymbol{q}})$
  - Update free vortex sheet $\mathcal{S}_v \leftarrow (\boldsymbol{\gamma}, \mathcal{S}_s, \boldsymbol{x}, \boldsymbol{u}_b)$
  - Create uniform panel at TE $(\mathcal{S}_u, \gamma_s) \leftarrow (\boldsymbol{\gamma}, \mathcal{S}_s, \boldsymbol{x}, \boldsymbol{u}_b, \beta)$
  - Update added mass $\boldsymbol{M}_a \leftarrow \boldsymbol{x}$
  - Solve linear system for $(\boldsymbol{\gamma}, \gamma_s) \leftarrow (\mathcal{S}_s, \boldsymbol{x}, \boldsymbol{u}_b)$
  - Compute shedding direction $\beta \leftarrow (\boldsymbol{\gamma})$
  - Compute hydro. loads and pressure $(\boldsymbol{f}, \boldsymbol{m}_{\boldsymbol{x}_{cm}}, p) \leftarrow (\boldsymbol{\gamma}, \mathcal{S}_s, \boldsymbol{x}, \boldsymbol{u}_b)$
- **end**
- **while** $t < T$ **do**
  - `RK4Proc(`$x \to$ `updateProc(`x`)`, t, Δt`)`
  - Coalesce uniform panel into new point vortex of $\mathcal{S}_s$
  - Solve linear system for $\boldsymbol{\gamma} \leftarrow (\mathcal{S}_s, \boldsymbol{x}, \boldsymbol{u}_b)$
  - Compute hydro. loads and pressure $(\boldsymbol{f}, \boldsymbol{m}_{\boldsymbol{x}_{cm}}, p) \leftarrow (\boldsymbol{\gamma}, \mathcal{S}_s, \boldsymbol{x}, \boldsymbol{u}_b)$
  - $t := t + \Delta t$
- **end**

end

Algorithm 3: Pseudocode for the unsteady flow solver for a continuous swimmer.

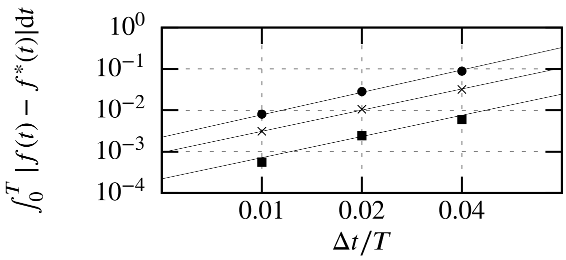

Figure 2.13: Log-log chart of the absolute error on the integral from $t = 0$ to $t = T$ of quantities $f(t) = E(t)$ (×), $f(t) = |\boldsymbol{x}|(t)$ (■) and $f(t) = |\boldsymbol{u}|(t)$ (•) obtained with a uniform discretization using the following sets of parameters: $\{\Delta t = 0.01T, N_p = 128\}$, $\{\Delta t = 0.02T, N_p = 64\}$ and $\{\Delta t = 0.04T, N_p = 32\}$ compared to a reference solution $f^*(t)$ computed using $\{\Delta t = 0.005T, N_p = 256\}$.

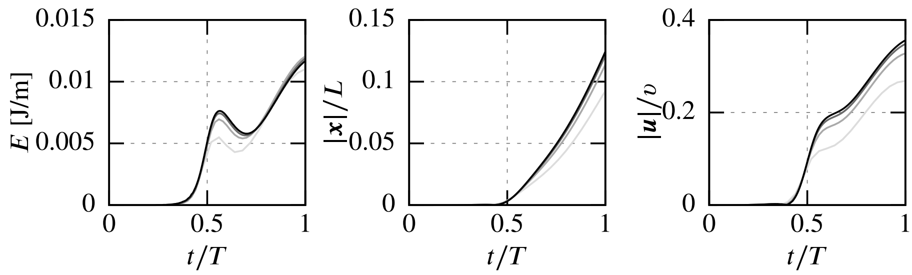

Figure 2.14: Evolution of spent actuation energy, absolute position and velocity of the swimmer obtained with different sets of parameters: $\{\Delta t = 0.04T, N_p = 32\}$ (—), $\{\Delta t = 0.02T, N_p = 64\}$ (—), $\{\Delta t = 0.01T, N_p = 128\}$ (—) and $\{\Delta t = 0.005T, N_p = 256\}$ (—).

its established swimming cycle. At that state, the velocity component parallel to the swimming direction obtained with our inviscid model surpasses the reference velocity by a margin exceeding 30%. Notably, the amplitude of the velocity component perpendicular to the swimming direction is nearly twofold when compared to the reference velocity. Our setting assumes an infinite Reynolds number for this flow, and hence an absence of friction forces, whereas the reference setup corresponds to $\mathscr{Re}_L = 3857$. Despite the significance of the aforementioned discrepancies in magnitude, the overall appearances of the velocity components are comparable.

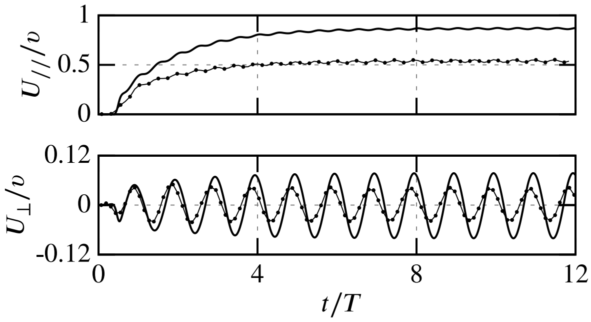

Figure 2.15: Simulation of a self-propelled anguilliform swimmer. Comparison of velocities between our model (——) and Kern and Koumoutsakos [34] (–•–).

In Fig. 2.16, aerodynamic coefficients are presented. The reference velocity used for their computation is defined as

$$U_\infty = \frac{1}{T} \int_{t_{max}-T}^{t_{max}} |\boldsymbol{u}| \, \mathrm{d}\tau. \tag{2.40}$$

The force and moment coefficients exhibit a closer agreement. The first peak of force aligned with the swimming direction is more than twice as large in our simulation as in the reference, the difference is then reversed but less significant in the second half-period. Past that time, both curves fall in better agreement with an observable difference in amplitude: the force has to compensate for added mass effect, vorticity and viscous friction in the reference case whereas added mass and vorticity constitute the only flow resistance in our model. Given the amplitude difference, assuming the swimming dynamics are mostly governed by added mass and vorticity seems reasonable. The perpendicular force coefficient exhibits the same behaviour as its parallel counterpart: a two-fold overshoot during the first half-period followed by a sinusoidal regime where the amplitude is lower than the reference. Finally, the moment coefficient is in good agreement with the reference after the initialization. This implies that viscous forces do not affect the rotation of the swimmer given this specific swimming gait. This is an expected result as viscous friction on both sides of a slender body should produce opposite moment contributions in a given section; the total moment is then logically dominated by pressure forces.

In Fig. 2.17, snapshots of our simulation up to $t/T = 12$ are presented. A close up view of the near-wake is shown in Fig. 2.18 and is compared with the vorticity field

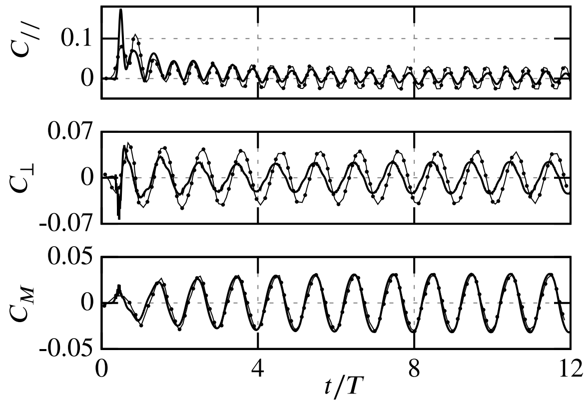

Figure 2.16: Simulation of a self-propelled anguilliform swimmer. Comparison of hydrodynamic coefficients between our model (——) and Kern and Koumoutsakos [34] (—•—).

obtained in [22] where more roll-up occurs. Although not exactly identical, the illustrations exhibit an analogous distribution pattern of vorticity. Furthermore, we notice the absence of any leading edge separation, supporting the reduction of the boundary layer to an infinitely thin vortex sheet used in our flow model. We consequently conclude from this comparison that our framework is able to capture the principal vortical structures in the wake of self-propelled anguilliform swimmers and is therefore a suitable tool to study the fundamental dynamics of schools consisting of a few swimming individuals. Any discrepancy with the reference is most likely associated with the reduction in model representativeness implied by the inviscid character of the proposed framework.

2.3.4 A turning maneuver

One of the principal reasons why the swimming gait was characterized by the instantaneous curvature $\kappa(s,t)$ along the body length coordinate was to easily maintain a constant body length L. Another important reason is to ease the maneuverability of the swimmer. Indeed, by adding or subtracting to κ a uniform curvature κ_0 along the spine of the swimmer, one can perform a turning maneuver to the right or left of the body, respectively. We show in Fig. 2.19 the swimming gait when $L\kappa_0 = 1$ and the swimmer therefore bends naturally more towards its right side.

(a) $t/T = 2$

(b) $t/T = 4$

(c) $t/T = 8$

(d) $t/T = 12$

Figure 2.17: A self-propelled anguilliform swimmer.

Figure 2.18: Snapshot of a self-propelled anguilliform swimmer at $t/T = n \in \mathbb{N}$, comparison between our model (left) and [22] (right).

As the body swims, the radius of the circle described by its center of mass is inversely proportional to κ_0. To make our point, we perform simulations of these maneuvers with $L\kappa_0 = 1/2$ and $L\kappa_0 = 1$. At initialization and until the end the swimming period, we maintain $\kappa_0 = 0$. At $t/T = 2$, we smoothly but quickly increase it to its target value using a sigmoid function with a characteristic time shorter than a swimming period. Snapshots of these simulations are presented in Fig. 2.20 and Fig. 2.21. In Fig. 2.22, we plot the followed trajectory in each scenario as well as the evolution of the main orientation of the swimmer. The radii of the trajectories are as predicted very close to the inverse of the average body curvature. Moreover, after the turn is initiated, the main body orientation oscillates around a straight line of slope $-L\kappa_0$/T.

(a) $t/T = 1.000$ (b) $t/T = 1.125$ (c) $t/T = 1.250$ (d) $t/T = 1.375$

(e) $t/T = 1.500$ (f) $t/T = 1.625$ (g) $t/T = 1.750$ (h) $t/T = 1.875$

Figure 2.19: Swimming gait over one period when $L\kappa_0 = 1$.

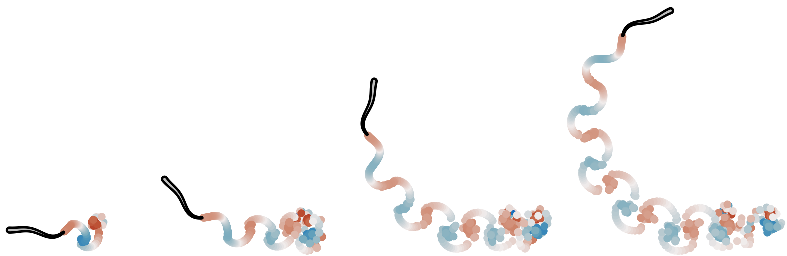

(a) $t/T = 2$ (b) $t/T = 4$ (c) $t/T = 6$ (d) $t/T = 8$

Figure 2.20: A self-propelled anguilliform swimmer executing a turning maneuver with $L\kappa_0 = 1/2$.

This is confirmed in Fig. 2.23 which displays the velocity components of the fish aligned with the swimming direction. As a reference, we also prompt the reference case where the eel swims straight ahead. In the established regime, the angular velocity oscillates well around the value stated above. As we increase κ_0, the terminal longitudinal velocity decreases while the transversal velocity oscillates around a higher value.

We also monitor the hydrodynamic coefficients for each level of κ_0. As one can observe, the shape of $C_{//}$ is altered and its amplitude follows the increase of κ_0. In the reference configuration, tail-beats occurring twice per period, one to the left and one to the right, contribute equally to thrust generation. Turning breaks this symmetry and

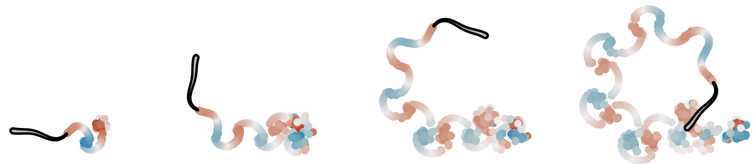

(a) $t/T = 2$ (b) $t/T = 4$ (c) $t/T = 6$ (d) $t/T = 8$

Figure 2.21: A self-propelled anguilliform swimmer executing a turning maneuver with $L\kappa_0 = 1$.

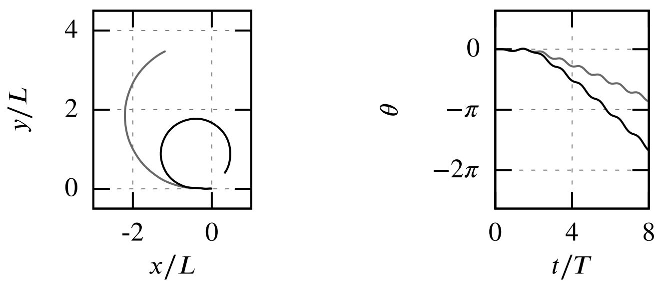

Figure 2.22: Trajectory and orientation of turning maneuvers with $L\kappa_0 = 1/2$ (—) and $L\kappa_0 = 1$ (—).

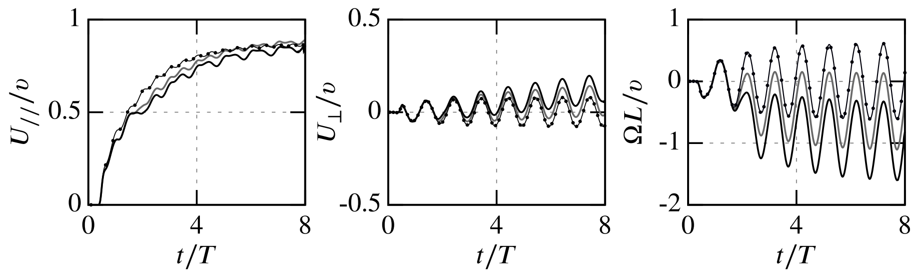

Figure 2.23: Velocity components aligned with the swimmer during turning maneuvers with $L\kappa_0 = 1/2$ (—) and $L\kappa_0 = 1$ (—) and $L\kappa_0 = 0$ (-•-).

restricts the thrust production to time intervals when the swimmer beats its tail to the left ($t/T = n \in \mathbb{N}$). On the other hand, right tail-beats drag the body backward and at the same time generate the least sideways force. Remarkably enough, the average value of $C_\perp$ plateaus to a value close to $0.1L\kappa_0$. This result agrees with basic mechanics since the centripetal acceleration of the swimmer directly relates to its angular velocity. After noting that the mass of the swimmer is close to $0.048L$[kg/m], observing the radius of the trajectory and the reference velocity in Figs. 2.22 and 2.23 allows to validate the relationship stated above. Increasing the average curvature has no significant impact on the moment coefficient except during the short period in which κ_0 increases from 0 to its target value. This is surprising as one would expect a change in body inertia and hereby of moment coefficient due to the shortening of the body as it wraps around itself. To conclude, as we approach $t/T = 8$, hydrodynamic forces start to deviate from there pattern in the case where $L/\kappa_0 = 1$. This happens because the swimmer comes into very close interaction with its own wake once its trajectory loops over itself. We avoid further complications by terminating simulations at that critical time.

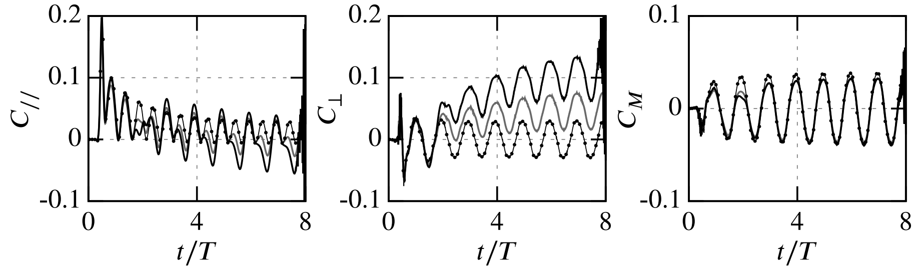

Figure 2.24: Hydrodynamic coefficients during turning maneuvers with $L\kappa_0 = 1/2$ (——), $L\kappa_0 = 1$ (——) and $L\kappa_0 = 0$ (–•–).

To push things further, we examine what happens when the target curvature evolves with time. We impose the following curvature:

$$\kappa_0(t) = \mathbb{1}_{t/T \geq 2} \sin\left(\frac{\pi}{2}(t/T - 2)\right), \tag{2.41}$$

where the value of $\mathbb{1}_x$ is either one if the boolean condition x is true or zero otherwise. The frequency of that signal is set on purpose to a value smaller than the main propelling gait to give the swimmer enough time to maneuver. To keep a horizontal overall swimming trajectory, the swimmer is initiated at an angle $\theta = \pi/9$ and all other simulation parameters are kept identical to previous simulations. Snapshots of this simulation are presented in Fig. 2.25.

Fig. 2.26 compares velocity components aligned with the anguilla undergoing the curvature modulation of Eq. (2.41) to the already familiar reference swimming motion. If nothing stands out for the linear velocities, the angular velocity displays the same behaviour as in the steady turning maneuvers. In this unsteady case, we have

$$\int_{t-T}^{t} \Omega(\tau)\, \mathrm{d}\tau = -L\kappa_0(t). \tag{2.42}$$

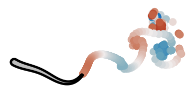

(a) $t/T = 3$

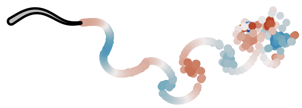

(b) $t/T = 5$

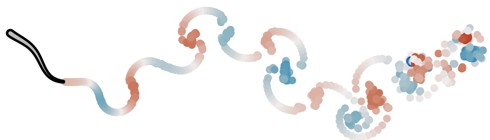

(c) $t/T = 8$

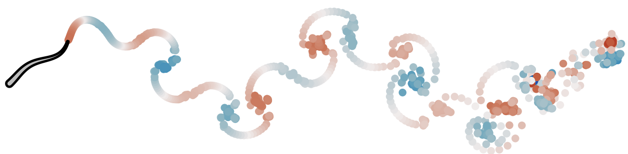

(d) $t/T = 10$

Figure 2.25: A self-propelled anguilliform swimmer with average curvature modulated with $L\kappa_0 = \mathbb{1}_{t/T\geq 2}\sin(\pi(t/T-2)/2)$.

Similarly, we also observe that

$$\frac{1}{T}\int_{t-T}^{t} C_{\perp}(\tau)\,\mathrm{d}\tau \approx 0.1 L\kappa_0(t), \tag{2.43}$$

when examining the hydrodynamic coefficients in Fig. 2.27. There does not seem to be any noticeable trend to extract from the thrust coefficient. Once again, the moment

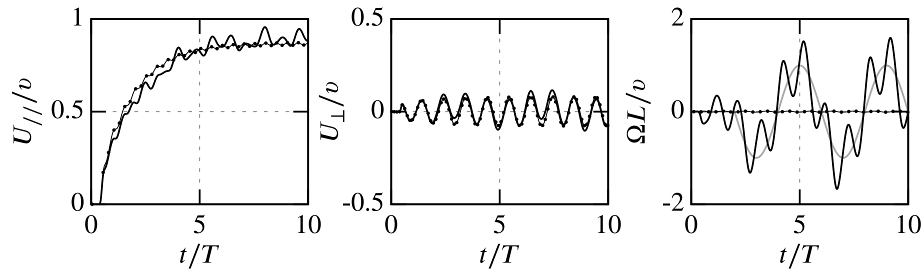

Figure 2.26: Velocity components aligned with the swimmer of average curvature modulated with $L\kappa_0 = \mathbb{1}_{t/T\geq 2}\sin(\pi(t/T-2)/2)$ (——) compared to the unmodulated case (—•—). Also shown is the quantity $-L\kappa_0/T$ (——) as a reference for Ω.

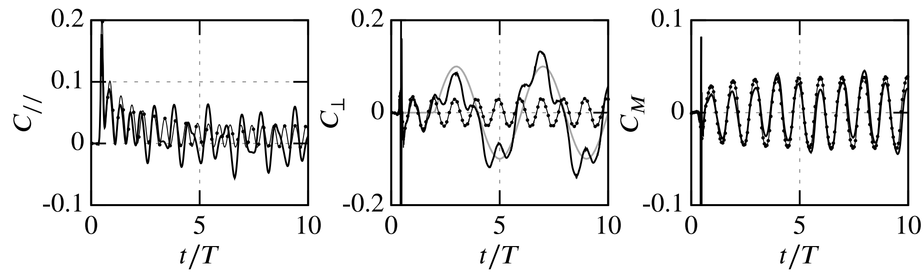

Figure 2.27: Hydrodynamic coefficients of the swimmer with average curvature modulated with $L\kappa_0 = \mathbb{1}_{t/T\geq 2}\sin(\pi(t/T-2)/2)$ (——) compared to the unmodulated case (—•—). Also shown is the quantity $0.1L\kappa_0$ (——) as a reference for $C_{\perp}$.

coefficient is barely affected by the addition of uniform curvature to the spine of the swimmer.

Though quite simple, these investigations teach us valuable lessons on maneuvering in inviscid flows. Enabling the control of average body curvature being the first step towards maneuverability of a fully controlled swimmer, it unveils straightforward relationships between the curvature and the swimming dynamics and hereby kinematics. This kind of relationships is a key element for predictive navigation, paving the way for the design of obstacle avoidance and wake energy harvesting strategies.

2.3.5 Encountering dipoles

Until now, trajectories followed by swimmers have all been internally driven. In other terms, the kinematics were the pure result of body deformation only since the swimmer evolved in a fluid at rest. However, swimming in a peaceful environment remains a rare event and actual *anguillae* have to cope with the vortical turmoil of agitated flows most of the time. A realistic model should account for such external perturbations. The simplest way our framework naturally enables this is through the injection of ambient vorticity at initialization of the fluid-body system. Of course, such injection should not lead to the creation of any linear and angular momenta in the flow. Vorticity is therefore added under the form of vortex dipoles.

We analyze the introduction of these perturbations in a simple test case in which the swimmer performs its usual swimming pattern in between a pair of incoming dipoles. All other things being equal, dipoles composed of point vortices of circulation $\Gamma T/L^2 = 2$ separated by a distance of $L/8$ are placed at positions $x/L = \{-3/2, -4\}$ and $y/L = \pm 1/2$. Their polarity is such that the dipoles naturally approach towards the swimmer. This is shown in Fig. 2.28 where snapshots of the simulation are displayed.

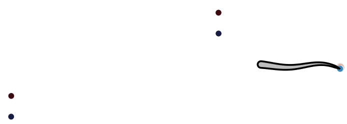

(a) $t/T = 0.5$

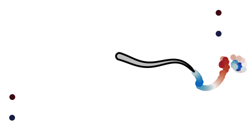

(b) $t/T = 1.5$

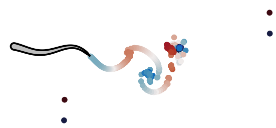

(c) $t/T = 2.5$

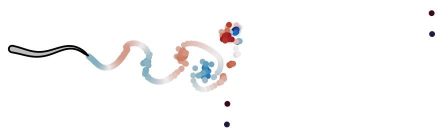

(d) $t/T = 3.5$

Figure 2.28: Swimmer passing through a pair of dipoles.

Given the path followed by the swimmer relative to the dipoles and their orientation. The swimming motion is expected to be eased by the free thrust resulting from the proximity of the dipoles. This is visible in Fig. 2.29 where the trajectory and orientation of the swimmer are presented and compared with the reference case. The trajectory is longer by a third of the body length thanks to velocity gains induced by the dipoles. These gains are shown in Fig. 2.30 where we analyze the velocity components aligned with the swimmer as well as its angular velocity. Passing by the first dipole (at $t/T \approx 1$) doubles both the parallel and the perpendicular velocity components, the effect on Ω is less pronounced. Between both dipoles, the swimmer benefits from an up wash resulting from the combined effect of both dipoles. Passing by the second dipole (at $t/T \approx 2.25$) also gives the swimmer a significant boost in the swimming direction but affects to a smaller extend the other velocity components. After $t/T = 2.5$, the swimmer gets far enough from the dipoles and their effect progressively vanishes.

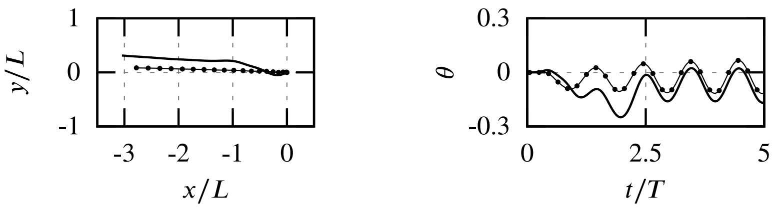

Figure 2.29: Trajectory and orientation of a swimmer encountering a pair of dipoles (—). Comparison with the unperturbed case (—•—).

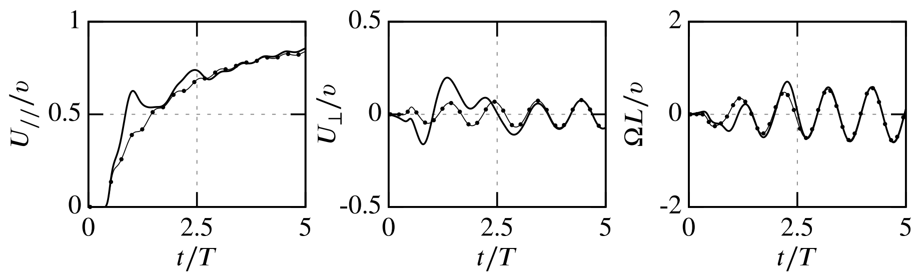

Figure 2.30: Velocity components aligned with a swimmer encountering a pair of dipoles (—). Comparison with the unperturbed case (—•—).

Fig. 2.31 gives even more insight by exhibiting the hydrodynamic coefficients. Indeed, the thrust coefficient shows two phases as we pass an incoming dipole: there is a thrust phase as the dipole attracts the body swimming towards it. However, as soon as the swimmer gets away from the dipole, its attraction has an adverse effect on the swimming effort and even produces drag for a limited time. As one might presume, the body is carried along the concentric streamlines around the dipole. The force perpendicular to the swimmer shows this behaviour as larger peaks occur a small time after the swimmer reaches the x-coordinate of the dipoles. The swimmer is first slightly pushed down and then strongly pulled up after crossing the first dipole. The second dipole first pushes it upwards slightly before sucking it back down. Curiously, the moment coefficient remains altered even after having crossed the dipoles.

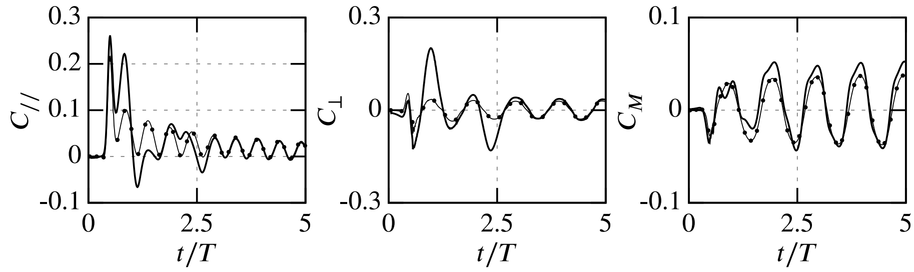

Figure 2.31: Hydrodynamic coefficients of a swimmer encountering a pair of dipoles (—). Comparison with the unperturbed case (—•—).

We show the pressure distribution on the surface of the swimmer at different times in Fig. 2.32 and compare it again with the case where no dipole perturbs the swimmer. At early times, the effect of the dipoles is only visible at the head of the swimmer where the pressure differs most from the reference distribution. As time progresses and as the dipoles and the fish approach each other, the whole distribution is strongly affected with a clear suction peak as the dipole passes very close to the middle of the swimmer at $t/T \approx 1$. As was the case for the other quantities, the second dipole shows a smaller effect than the first one on the pressure distribution.

To conclude this small experiment, we can say that perturbations in the flow in which a numerical fish is swimming may have a significant effect on its dynamics and kinematics. This effect also manifests on less observable characteristics of the system like the pressure distributed on the body surface. From a more practical point of view, it means that sensing the flow using accelerometers and pressure sensors might equip the swimmer with enough information to navigate in its environment in a controlled or optimized way.

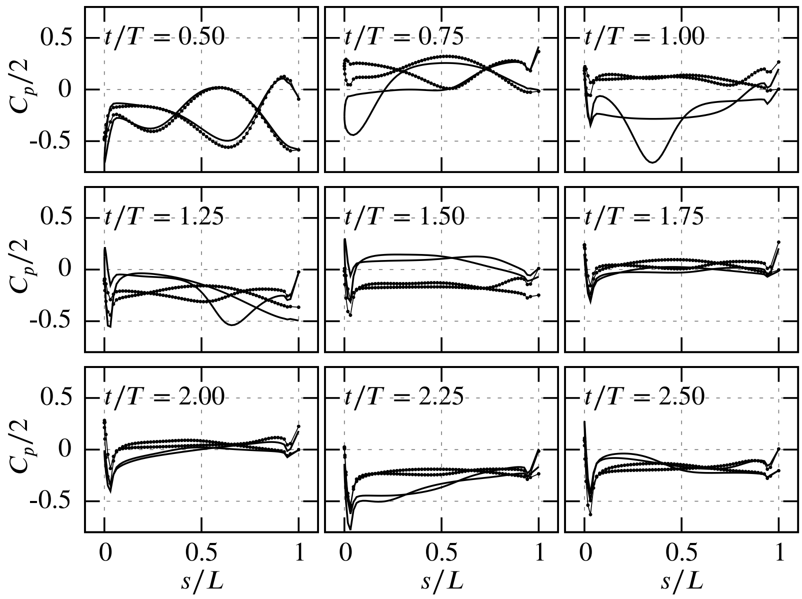

Figure 2.32: Pressure distribution on the body surface. Comparison between the swimmer encountering dipoles (—) and the reference case (–•–).

2.4 Multiple anguilliform swimmers

In this section, we further extend the framework to deal with N self-propelled eel-like swimmers each being discretized with N_p panels. To achieve this, we build a linear system to solve for bound vorticity resulting from $N \times (N_p + 2)$ constraints (non-penetration, Kutta and Kelvin for each individual). In addition, the size of the dynamical system to integrate in time increases to $3N$, each body having 3 degrees of freedom.

To account for the hydrodynamic interactions between all immersed bodies, the added mass matrix is extended to a size $3N$ as well. Following the methodology provided in Section 2.1.1, each line of the extended added mass matrix represents the linear and angular momenta computed for each body (in the frame of reference centered at their respective center of mass) caused by the unitary actuation of each degree of freedom.

2.4.1 A pair of swimmers

Two experiments are conducted with a pair of swimmers. In both cases, the fish are initially at rest, their body is fully extended and they are separated by a vertical distance of $0.6L$. They share the same swimming gait as was provided in Section 2.3.1. The surface of the swimmers is discretized with 128 panels and the time step is $\Delta t = 0.01T$. All other parameters are kept identical to the values given in previous Sections. The fish swim in phase in the first experiment and in phase opposition in the second.

Figs. 2.33 and 2.34 present snapshots of the swimmers until $t/T = 8.5$ in both situations. In addition, Fig. 2.35 shows the trajectories followed by the swimmers in each case. As a general comment, we observe that trajectories of our model are significantly longer than the reference. This is explained by the higher forward velocity already observed and discussed in 2.3.3. When the swimmers swim in phase, they tend to drift apart from one another and the global direction of the pair bends upwards. This change of direction is much more pronounced in [22] than in our model even though the trajectory of the bottom fish is very close to the reference simulation. When the swimmers swim in phase opposition, they first get closer to each other before swimming apart. This behaviour creates a more contained pair of trajectories.

2.4.2 A school of five swimmers

The second pair of experiments considers the school of five swimmers presented in [22]. In the first test case, fish are vertically aligned and separated by a distance of $0.4L$. In the second one, they form a V-shape and are offset by $1.5L$ in the x-direction and $0.4L$ in the y-direction. They all swim in phase and following the same gait as defined in Eq. (2.28). All other simulation parameters are also kept identical to previous experiments.

Trajectories of the fish in both inline and staggered simulations are shown in Fig. 2.36 and compared to [22]. We can see that our model produces very similar swimming routes. However, in the case of the aligned swimmers, trajectories resulting from our model are longer and show a less pronounced spread. Trajectories for the staggered formation are very similar to their reference but differ in length. Indeed, if the range of top swimmers is significantly shorter than the range of their bottom counterpart in the reference case, our model yields a more even set of ranges regardless of the initial positioning of an individual in the school. In both swimming formations, both models display an upward trend because of the already mentioned asymmetry inherent to the initialization of the swimming gaits.

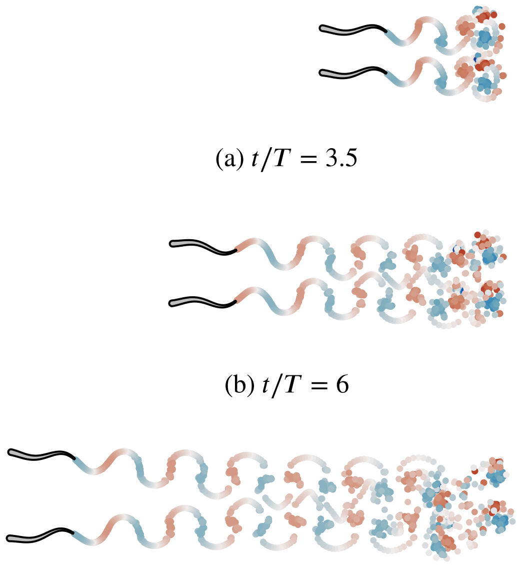

(a) $t/T = 3.5$

(b) $t/T = 6$

(c) $t/T = 8.5$

Figure 2.33: A pair of self-propelled anguilliform swimmers swimming in phase.

Fig. 2.37 presents snapshots of the school formation of five fish initially aligned and swimming in phase until $t/T = 7.2$. Similarly, Fig. 2.38 shows the simulation of the staggered school.

2.5 Discussion

This Chapter extended the inviscid vorticity-based simulation framework to locomotion of flexible bodies presenting a finite-angle trailing edge. We introduced the concept of added mass and how it is used to stabilize the equilibrium equation of the fluid-body dynamical system.

A first pair of simulations were run on the simplified setup of a 3-link swimmer composed of rigid ellipses. They present the particularity of using a purely potential-flow-driven variant of the framework for the sake of validation. Both simulations yielded results closely inline with their respective reference benchmark.

Then, we switched to a locomotion model with vortex shedding dedicated to the case of a continuous anguilliform swimmer. We performed a comparison with viscous

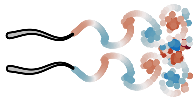

(a) $t/T = 3.5$

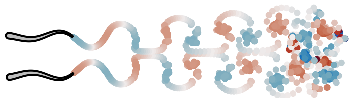

(b) $t/T = 6$

(c) $t/T = 8.5$

Figure 2.34: A pair of self-propelled anguilliform swimmers swimming in anti-phase.

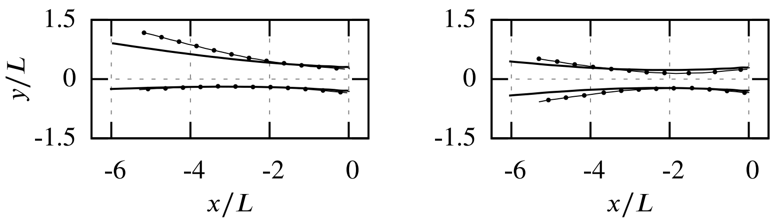

Figure 2.35: Trajectories of a pair of swimmers swimming in-phase (left) and anti-phase (right) up to $t/T = 8.5$. Comparison between our model (—) and Gazzola et al. [22] (–•–).

vortex-based CFD models after a quick convergence analysis in the case of straight-line swimming. The model displayed a convergence order of $\mathcal{O}(1.7)$ on this benchmark. It showed similar patterns in terms of velocity and hydrodynamic loads between our model and more precise CFD. However, our results were characterized by a much higher terminal speed and amplitude of the velocity perpendicular to the body. The

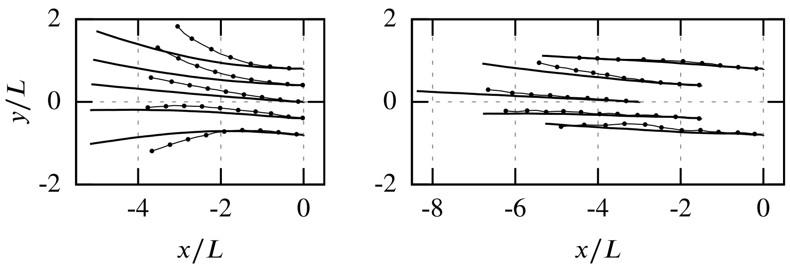

Figure 2.36: Trajectories of five swimmers swimming in an aligned (left) and staggered (right) formation up to $t/T = 7.2$. Comparison between our model (——) and Gazzola et al. [22] (—•—).

same component of the force coefficient showed a similar difference. These differences emerge from the absence of dissipative viscous forces in our model.

Next, three turning maneuvers were examined: they showed that we can modulate the trajectory of a swimmer in a straightforward way by adding a uniform curvature distribution to the spine of the swimmer. This is a simple and easy way to introduce controllability in the swimming system without the need for modeling the internal mechanics of the swimmer.

The last analysis carried out on the single swimmer regards the effect of external perturbations under the form of incoming vortex dipoles. They exert a significant influence on the swimmer when they are in its close vicinity. This effect is observable on the trajectory, velocity, pressure distribution and hydrodynamic loads exerted on the body. This means that we could elaborate sensing strategies to try to identify or locate vortical structures in the surrounding flow. These sensing strategies could be useful for load alleviation or efficient navigation purposes.

Finally, the framework was extended to multiple swimmers and simulations involving two or five fish in different setups were presented and compared with results obtained with the CFD model of [22]. They showed similar trajectory patterns in spite of the absence of viscous friction.

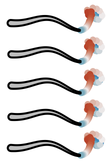

(a) $t/T = 1$

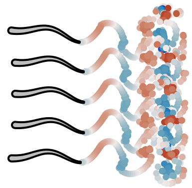

(b) $t/T = 3.5$

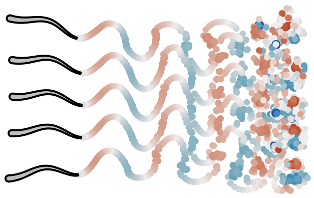

(c) $t/T = 6$

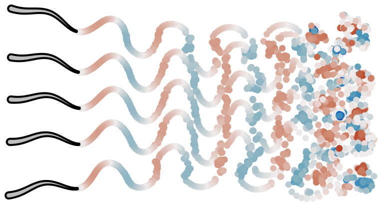

(d) $t/T = 7.2$

Figure 2.37: A school of five aligned self-propelled anguilliform swimmers.

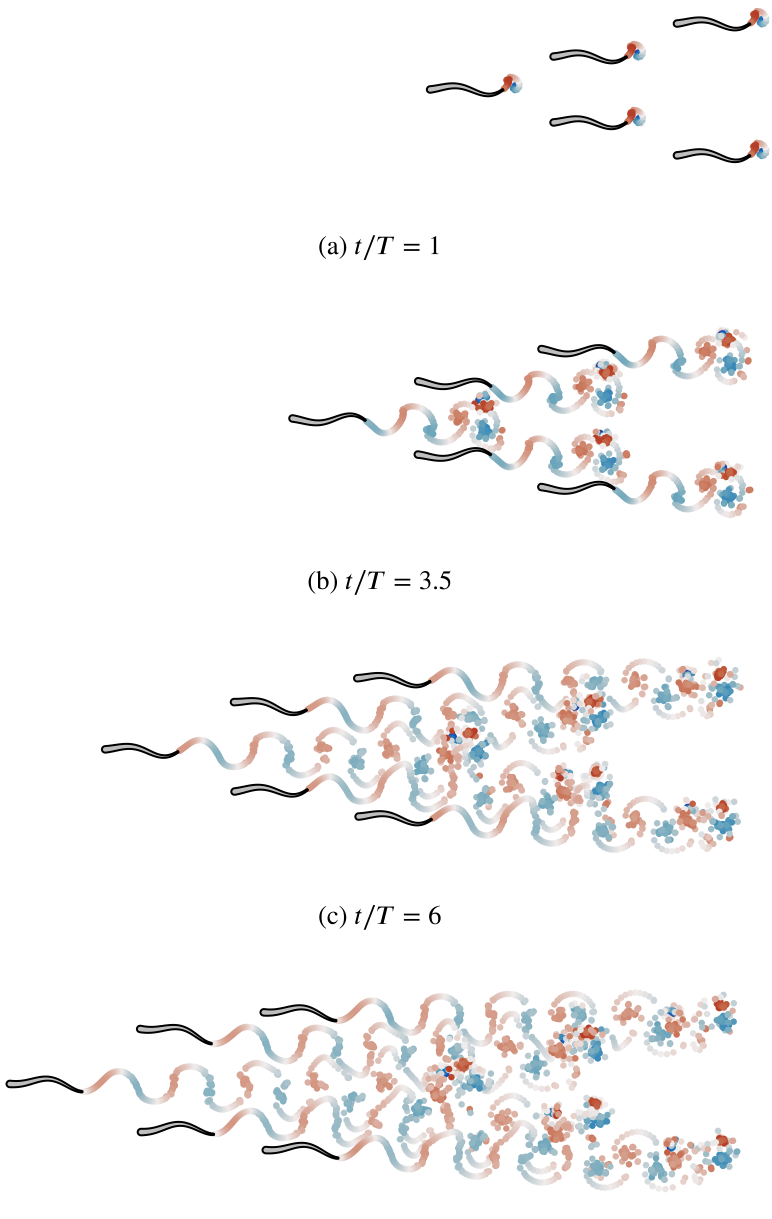

(a) $t/T = 1$

(b) $t/T = 3.5$

(c) $t/T = 6$

(d) $t/T = 7.2$

Figure 2.38: A school of five staggered self-propelled anguilliform swimmers.

CHAPTER 3

Swimmers as multi-body systems

This Chapter exposes the swimming problem from a roboticist point of view. This step is necessary to enable the control of a swimmer by means of rotary actuators located at each of its articulations, as would be the case in an actual swimming robot. We begin by deriving a few generalities on Lagrangian mechanics prior to their application to both ellipse-made and continuous flexible swimmers.

After a presentation of the mathematical framework for studying the dynamics of multi-body systems [see 51, 62] in Section 3.1. Then we transpose the MBS formalism to the swimming problem in Section 3.2 and treat the numerical aspects in Section 3.3. As an intermediary step towards direct control through joints of a swimmer, we first put our focus on inverse dynamics, i.e. observing the actuation moments of a swimmer when its kinematics are imposed and a validation benchmark in Section 3.4 before addressing the direct dynamics in Section 3.5.

3.1 Lagrangian mechanics

Consider a set $\mathscr{B}$ of N bodies. Body i has mass m_i and inertia matrix $\boldsymbol{I}_i$ and is defined with the position of its center of mass $\boldsymbol{x}_i$ and its orientation $\boldsymbol{\theta}_i$. It undergoes external force $\boldsymbol{f}_i$ and torque $\boldsymbol{l}_i$ as well as constraint loads $\boldsymbol{f}_i^c$ and $\boldsymbol{l}_i^c$ (such as internal physical constraints and reaction to external loads). In addition, let us define the virtual displacement $\delta\boldsymbol{x}_i$ as an instantaneous and infinitesimal displacement obeying physical constraints. The same definition applies for the virtual angular displacement $\delta\boldsymbol{\theta}_i$.

D'Alembert's principle states that the virtual work exerted on $\mathscr{B}$ by the constraint forces and torques is zero, in other terms

$$\sum_{i=1}^{N} \left(\boldsymbol{f}_i^c \cdot \delta \boldsymbol{x}_i + \boldsymbol{l}_i^c \cdot \delta \boldsymbol{\theta}_i \right) = 0. \tag{3.1}$$

Therefore, starting from the equilibrium of momentum of body i and its first moment relative to the i-th center of mass

$$\frac{\mathrm{d}}{\mathrm{d}t} \left(m_i \dot{\boldsymbol{x}}_i \right) = \boldsymbol{f}_i + \boldsymbol{f}_i^c, \tag{3.2}$$

$$\frac{\mathrm{d}}{\mathrm{d}t} \left(\boldsymbol{I}_i \dot{\boldsymbol{\theta}}_i \right) = \boldsymbol{l}_i + \boldsymbol{l}_i^c, \tag{3.3}$$

we can calculate the total virtual work on $\mathscr{B}$ and obtain

$$\sum_{i=1}^{N} \left[\left(\frac{\mathrm{d}}{\mathrm{d}t} \left(m_i \dot{\boldsymbol{x}}_i \right) - \boldsymbol{f}_i \right) \cdot \delta \boldsymbol{x}_i + \left(\frac{\mathrm{d}}{\mathrm{d}t} \left(\boldsymbol{I}_i \dot{\boldsymbol{\theta}}_i \right) - \boldsymbol{l}_i \right) \cdot \delta \boldsymbol{\theta}_i \right] = 0. \tag{3.4}$$

Next, we define the generalized coordinates $\boldsymbol{q}$ as the set of variables that suffices to fully determine the system $\mathscr{B}$ while satisfying the physical constraints. These n variables can take the form of relative positions or angles. Taking advantage of the physical constraints to represent $\mathscr{B}$ often offers a significant reduction in the system dimensionality: $n \leq 3N(\mathscr{N}_d - 1)$.

Therefore, applying the chain rule on the virtual displacements:

$$\delta \boldsymbol{x}_i = \sum_{j=1}^{n} \frac{\partial \boldsymbol{x}_i}{\partial q_j} \delta q_j, \quad \delta \boldsymbol{\theta}_i = \sum_{j=1}^{n} \frac{\partial \boldsymbol{\theta}_i}{\partial q_j} \delta q_j, \tag{3.5}$$

we can reduce the dimensionality of Eq. (3.4) and find

$$\sum_{j=1}^{n} \left(a_j - \tau_j \right) \delta q_j = 0, \tag{3.6}$$

where a_j and τ_j are the j-th generalized acceleration and force, respectively.

While it is straightforward to show that

$$\tau_j = \sum_{i=1}^{N} \left(\boldsymbol{f}_i \cdot \frac{\partial \boldsymbol{x}_i}{\partial q_j} + \boldsymbol{l}_i \cdot \frac{\partial \boldsymbol{\theta}_i}{\partial q_j} \right), \tag{3.7}$$

a bit more work (see [62]) is required to find

$$a_j = \sum_{k=1}^{n} d_{jk}\ddot{q}_k + \sum_{k=1}^{n} c_{jk}\dot{q}_k, \tag{3.8}$$

where the j,k-th generalized inertia is

$$d_{jk} = \sum_{i=1}^{N} \left(m_i \frac{\partial \boldsymbol{x}_i}{\partial q_j}^T \frac{\partial \boldsymbol{x}_i}{\partial q_k} + \frac{\partial \boldsymbol{\theta}_i}{\partial q_j}^T \boldsymbol{R}_i \boldsymbol{I}_i \boldsymbol{R}_i^T \frac{\partial \boldsymbol{\theta}_i}{\partial q_k} \right), \tag{3.9}$$

$\boldsymbol{R}_i \in \mathfrak{so}(3)$ is the rotation matrix of body i. When $\mathcal{N}_d = 2$, only the rotational degree of freedom around $\hat{\boldsymbol{e}}_z$ is relaxed and $\boldsymbol{\theta}_i$ and $\boldsymbol{I}_i$ become scalar quantities, releasing the dependency on any rotation matrix.

The j,k-th Christoffel symbol of the 1st kind is

$$c_{jk} = \sum_{i=1}^{n} \frac{1}{2} \left(\frac{\partial d_{jk}}{\partial q_i} + \frac{\partial d_{ji}}{\partial q_k} - \frac{\partial d_{ik}}{\partial q_j} \right) \dot{q}_i. \tag{3.10}$$

Finally, noting that the virtual displacement is non-zero in Eq. (3.6), we end up with the set of Euler-Lagrange equations:

$$\boldsymbol{D}(\boldsymbol{q})\ddot{\boldsymbol{q}} + \boldsymbol{C}(\boldsymbol{q}, \dot{\boldsymbol{q}})\dot{\boldsymbol{q}} = \boldsymbol{\tau}. \tag{3.11}$$

3.2 Dynamics of a swimmer

It is now possible to use the Euler-Lagrange formalism to represent the dynamics of a swimmer. One adequate way of defining generalized coordinates is to use the absolute position of the center of mass of the swimmer as well of the angles between two consecutive links. This choice is used in our MBS model and illustrated in the case of the 3-ellipsoidal-link swimmer in Fig. 3.1, represented by $n = 5$ generalized coordinates. Because the center of mass is not rigidly attached to any material point of the body, a more practical choice is to use the position of the center of mass of the first segment of the swimmer to define the two translational generalized coordinates. Even though either convention does yield the same actuation moments, the latter formalism is better suited to a replication of the results using *Robotran* [see 14, 60], a software for solving MBS problems developed at UCLouvain.

To enable the discrimination between external and actuation loads, it is necessary to split generalized forces into a contribution coming from the hydrodynamic pressure

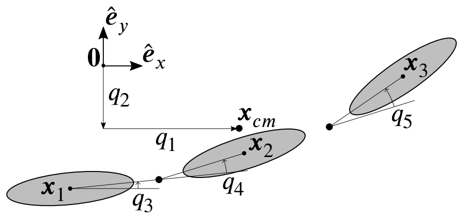

Figure 3.1: A 3-link swimmer composed of rigid ellipses.

on the surface of the swimmer and a term accounting for the torques imposed at the actuators. Equation (3.11) becomes

$$\boldsymbol{D}(\boldsymbol{q})\ddot{\boldsymbol{q}} + \boldsymbol{C}(\boldsymbol{q}, \dot{\boldsymbol{q}})\dot{\boldsymbol{q}} = \boldsymbol{\tau}_h + \boldsymbol{\tau}_a, \tag{3.12}$$

where $\boldsymbol{\tau}_h$ are the generalized forces resulting from the hydrodynamic loads on each segment and $\boldsymbol{\tau}_a$ contains the actuation torques.

The hydrodynamic generalized forces in Eq. (3.7) require the loads derived from the pressure distribution on the surface $\mathcal{S}_i$ of each articulated segment of the swimmer

$$\boldsymbol{f}_i = -\int_{\mathcal{S}_i} p_i \boldsymbol{n} \, \mathrm{d}S, \tag{3.13}$$

$$\boldsymbol{l}_i = -\int_{\mathcal{S}_i} (\boldsymbol{x} - \boldsymbol{x}_i) \times p_i \boldsymbol{n} \, \mathrm{d}S, \tag{3.14}$$

where the surface of the entire swimmer is partitioned as $\cup_i \mathcal{S}_i = \mathcal{S}_b$. An illustration is provided in Fig. 3.2 in the case of the 3-ellipsoidal-link swimmer and in Fig. 3.3 in the case of a single continuous swimming body. In that latter case, inter-link stresses are not involved in the computation of external loads on segment i, the origin of which is limited to the pressure on the interface between the segment and the fluid surrounding it. Because of the bipartite nature of that fluid-link interface, it appears clear why the pressure distribution is used to compute hydrodynamic loads instead of approaches based on closed volumes like the momentum budget Eq. (1.36) or the so-called Noca formulas Eqs. (1.40) and (1.41).

3.3 Numerical methods

We develop an extension to the original flow model enabling the study of multi-body systems in *julia* using the `ForwardDiff.jl` package [57]. This package allows to

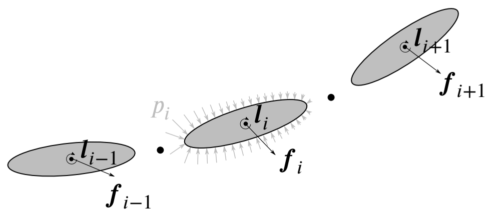

Figure 3.2: External loads on a 3-link swimmer.

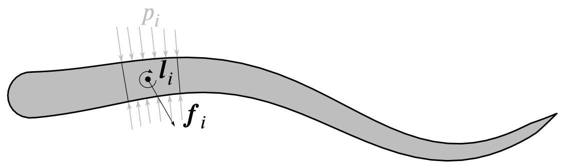

Figure 3.3: External loads on a segment of a continuous swimmer.

effortlessly compute any function derivative by overloading the basic mathematical functions and operators it uses with their associated derivation rules.

The package is essentially used to compute $\boldsymbol{D}$ and $\boldsymbol{C}$ matrices in Eq. (3.11) from the N mappings $\mathbb{R}^n \to \mathbb{R}^2 : \boldsymbol{q} \mapsto \boldsymbol{x}_i$ giving the centers of mass of all links from the generalized coordinates. Under this strategy, the specific mapping for the chain-like swimmer of Eq. (2.20) is just an input to the framework which can be reused and provided with the mapping associated with any other multi-body system.

3.4 Validation: inverse dynamics

The first task of the new model extension is to enable the computation of actuation loads $\boldsymbol{\tau}_a$ in the joints of the swimmer under the imposed kinematics $(\boldsymbol{q}, \dot{\boldsymbol{q}}, \ddot{\boldsymbol{q}})$. These moments are what would be necessary to apply to actuators to observe the given kinematics of the body under the resulting hydrodynamic loads τ_h. We use the symbolic MBS software *Robotran* to validate our results.

3.4.1 The 3-link body

We start with the validation of the Euler-Lagrange multi-body system framework on the 3-link body. Under these circumstances, we can confidently validate the model using *Robotran* because the main characteristics of this set up comply with the requirements of the software, namely the invariability of the geometry, mass and inertia of every link composing the swimmer.

The reference swimming gait used in Chapter 2 is used in two distinct experiments: the swimmer first deforms in a domain exempt of fluid and therefore undergoes no external load and then evolves in the perfect fluid considered in every other Chapter of this manuscript.

In both benchmarks, geometric parameters of the swimmer are $L = 1$, $e = d = L/10$. Once again, each segment is discretized using Chebyshev's distribution with $N_p = 200$ panels and the time step is set to $\Delta t = 0.02T/2\pi$. The swimming gait is determined by the relative angles between the segments dictated by the motion of period $T = 2\pi$

$$q_4(t) = -\sin t/T, \qquad q_5(t) = -\cos t/T, \tag{3.15}$$

and their time derivatives.

In vacuum

The 3-link body first swims in free space where it undergoes no external force. In that case, there is no exchange of momentum between the body and its environment and the center of mass of the swimmer therefore remains immobile. Snapshots of eight configurations taken over the course of a deformation period are presented in Fig. 3.4.

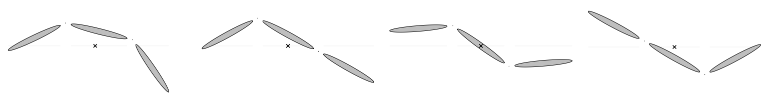

(a) $t/T = 1.125$ (b) $t/T = 1.250$ (c) $t/T = 1.375$ (d) $t/T = 1.500$

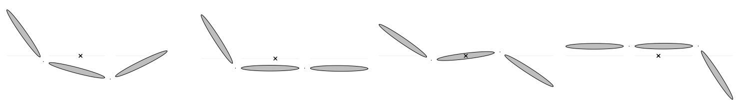

(e) $t/T = 1.625$ (f) $t/T = 1.750$ (g) $t/T = 1.875$ (h) $t/T = 2.000$

Figure 3.4: Snapshots of the swimming gait in vacuum over one deformation period when $q_4(t) = -\sin t/T$ and $q_5(t) = -\cos t/T$. The origin of the inertial frame of reference is represented with $\times$.

As one can observe in Fig. 3.5 where the measured actuation moments at both articulations are shown, *Robotran* and our model agree perfectly. Generalized forces

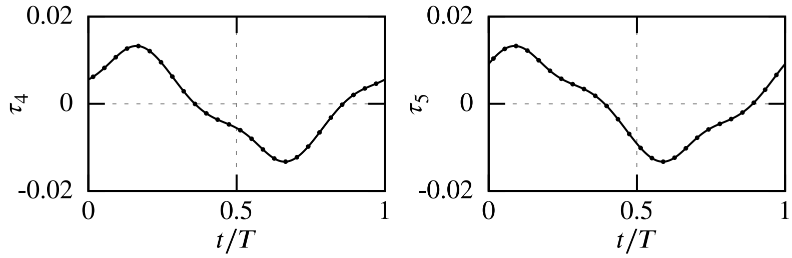

Figure 3.5: Actuation moments at each articulation of the 3-link swimmer in vacuum. Comparison between our framework based on Euler-Lagrange (—–) and *Robotran*(–•–).

for the 3 external – and in this case relaxed – degrees of freedom ($\tau_1 = f_x$, $\tau_2 = f_y$ and $\tau_3 = m_{\mathbf{x}_{cm}}$) are shown in Fig. 3.6 where both models agree on a force of zero magnitude (up to machine precision) applied on the global center of mass of the swimmer and a negligible hydrodynamic moment due to the error in angular position associated with the numerical integration of the velocity computed in Eq. (2.23) for *recoil correction*.

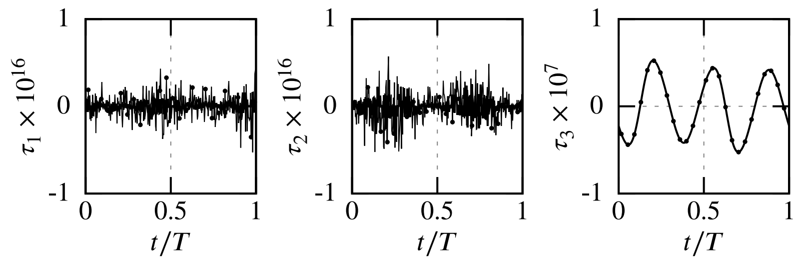

Figure 3.6: Generalized forces on the first three degrees of freedom of the 3-link swimmer in vacuum. Comparison between our framework based on Euler-Lagrange (—–) and *Robotran*(–•–).

In a surrounding fluid

We replicate the experiment but this time, hydrodynamic forces interact with and propels the deforming assembly. They yield actuation moments of order of magnitude approximately 5 times higher than the torques required to deform the swimmer in vacuum. This is visible in Fig. 3.7.

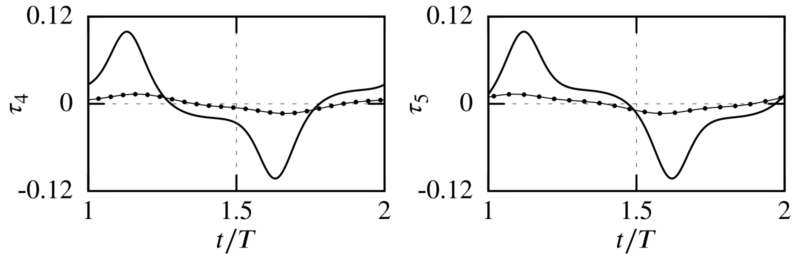

Figure 3.7: Actuation moments at each articulation of the 3-link swimmer obtained with the Euler-Lagrange MBS model. Comparison of the swimmer in fluid (——) and in vacuum (—•—).

Again, we validate the moments at the articulations of the swimmer in Fig. 3.8 with *Robotran*. Both MBS models agree and produce overlapping results. Figure 3.9 shows the 3 external generalized forces when hydrodynamic forces are accounted for. Even though we still expect to see a flat line at 0, the divergences are this time reasonably more significant than in vacuum with an order of magnitude still smaller than 1% of the hydrodynamic forces and moment responsible for the body displacement (see Fig. 2.6). Both frameworks display the same forces but they disagree on the global moment. This is actually due to the difference in application points: the body rotates around the overall center of mass according to the Euler-Lagrange framework whereas *Robotran* defines the rotation around the center of mass of the first ellipse. This difference is given by

$$\delta\tau_3 = (\boldsymbol{x}_{cm} - \boldsymbol{x}_1) \times \boldsymbol{\tau}_{1:2} \cdot \hat{\boldsymbol{e}}_z, \tag{3.16}$$

and was not observed in vacuum because the magnitudes of hydrodynamic forces were virtually zero and had no impact on the change of application point. Applying this change of point of reference point leads to matching results.

3.4.2 The anguilliform swimmer

In vacuum

We now examine the anguilliform swimmer in vacuum to completely assess our MBS solver regardless of the effect of the fluid. We justify this last validation step by the following fact: in this setup, segments composing the swimmer deform. They change shape as well as moment of inertia. We make the assumption that under small deformation, each trapezoidal link conserves its mass. Under the validity of this hypothesis,

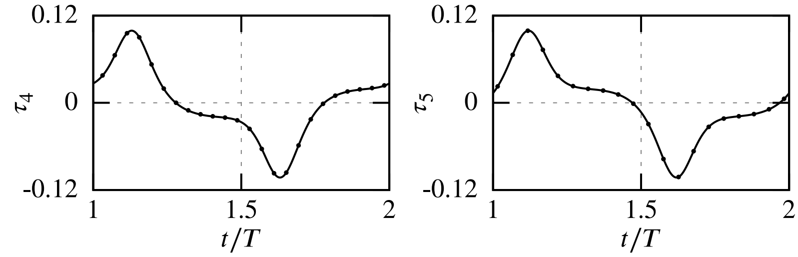

Figure 3.8: Actuation moments at each articulation of the 3-link swimmer surrounded by fluid. Comparison between our framework based on Euler-Lagrange (—) and *Robotran*(—•—).

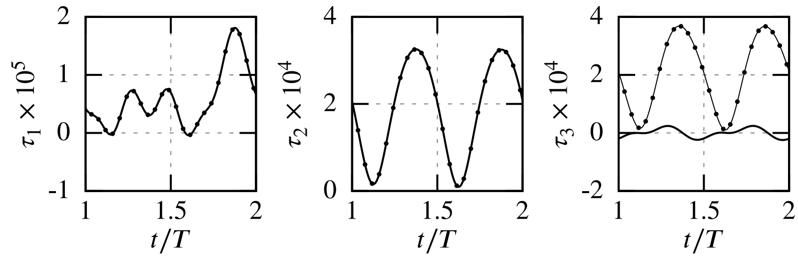

Figure 3.9: Generalized forces on the first three degrees of freedom of the 3-link swimmer surrounded by fluid. Comparison between our framework based on Euler-Lagrange (—) and *Robotran*(—•—).

the aforementioned consequences of link deformation should not wreak havoc on the accuracy of our model which by design extends the abilities of *Robotran*.

The swimmer already described in the previous Chapter performs the oscillatory gait given by Eq. (2.28) in vacuum and the actuation torques are evaluated by means of the Euler-Lagrange Eq. (3.11). The spatio-temporal discretization is defined in the same fashion as in Section 2.3.3.

For validation purposes, the inverse dynamics experiment is also carried out using *Robotran*. This software relies on the assumption that every link of a MBS is rigid (i.e., it has a constant inertia matrix and a center of mass fixed in the link-attached frame of reference). This assumption is violated in the case of the flexible swimmer because its sections deform. Hence, we expect *Robotran* not to perform as well as our framework in which the internal transfers of inertia induced by the deformation are accounted for.

Snapshots of actuation torques over one deformation period are provided in Fig. 3.10. They show that our model is in good agreement with *Robotran* near the trailing-edge of the swimmer. At both extremities of the body, no internal torque shall be observed when the swimmer freely moves in vacuum. However, as we approach the head, discrepancies appear and *Robotran* fails to converge to zero at the head. Our model on the other hand demonstrates a superior ability to corroborate a free condition at the head. This difference agrees with the limitation of *Robotran* mentioned in the previous paragraph. Finally, the fact that the actuation moment at the head tends to zero with Euler-Lagrange also allows to validate the recoil correction step applied in equation (2.37). Indeed, a non-zero moment at the head would imply the swimmer exchanges angular momentum with its environment through a spurious dissipative hinge.

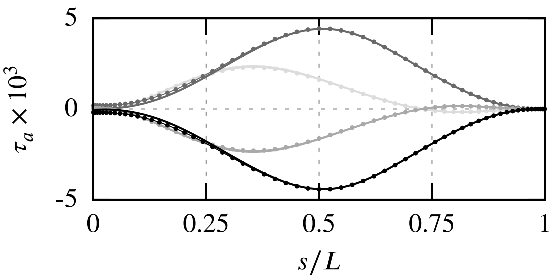

Figure 3.10: Distribution of the actuation torques on the spine of a swimmer in vacuum. Comparison between our framework based on Euler-Lagrange (—) and *Robotran*(—•—). Snapshots are taken at $t = T$ (—), $t = 1.25T$ (—), $t = 1.5T$ (—) and $t = 1.75T$ (—).

In a surrounding fluid

Then, we switch to the more interesting case where the body undergoes hydrodynamic loads from the surrounding flow. We present the actuation moments in figure 3.11. We observe that they act as a single-mode quasi-standing wave with nodes at the extremities of the swimmer, as experiments led by Voesenek et al. [71] confirm. Over the course of the first swimming period, the amplitude of the wave is approximately tenfold what is observed in regime where it falls back to an amplitude comparable to what was observed in vacuum (see figure 3.10). Another remarkable fact is that, at the head of the swimmer ($s = 0L$), measured actuation loads are not exactly zero but close to 20% of their maximal amplitude (reached at $s \approx 0.5L$). This means that the flow model poorly conserves overall angular momentum. In order to identify the contributions of the flow-induced stresses, we subtract in figure 3.12 the inertia-induced moments of the swimmer in vacuum from the actuation moments of the present established swimming regime. These contributions to the actuation moments can be seen to lag behind the inertia-induced ones by $\sim \pi/3$.

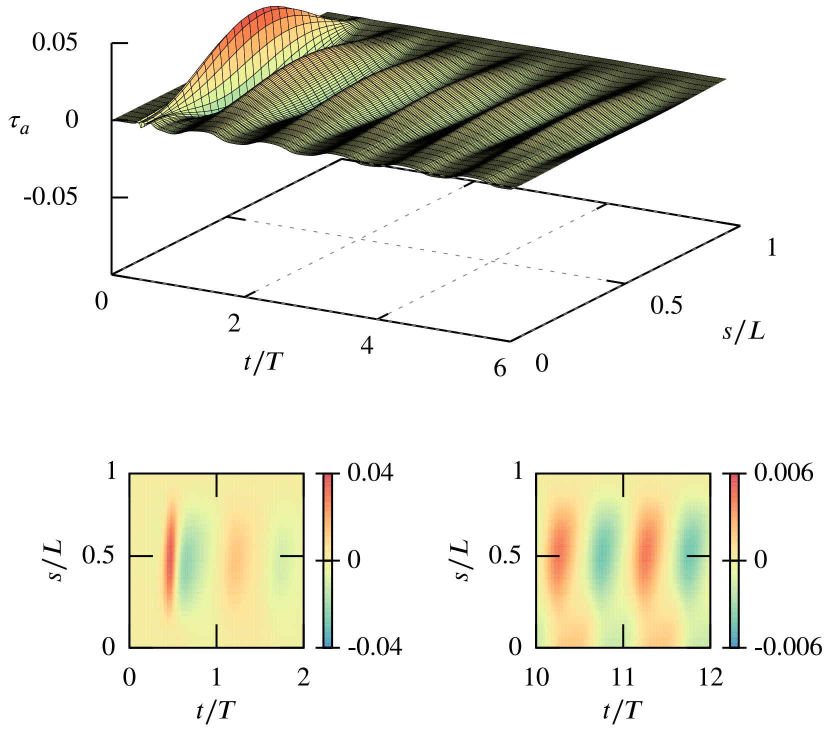

Figure 3.11: Surface plot of the actuation moments along the spine of a starting swimmer (top). Color contours of the actuation moments during two swimming periods at the start (left) and in regime (right).

Knowing the torques in the actuations enables the computation of the internal power and hence energy spent by the fish when swimming. We have indeed

$$P = \boldsymbol{\tau}_a \cdot \dot{\boldsymbol{q}}, \tag{3.17}$$

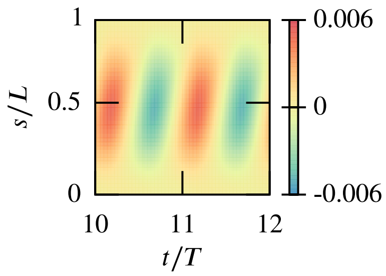

Figure 3.12: Color contours of actuation moment components during two periods of established swimming regime: inertia-induced (left) and flow-induced (right).

where the contribution of the 3 first components of $\boldsymbol{\tau}_a$ should in theory be zero. In practice, they are not so we discard them from the result as they represent some instantaneous power dissipated during the overall body displacement. With the actuation power in hands, we can define the cost of transport, a metric to assess the swimming performance of the anguilla given by

$$CoT(t) = \frac{E(t)}{md(t)} = \frac{\int_0^t P(\tau)\,\mathrm{d}\tau}{m\int_0^t \|\boldsymbol{u}(\tau)\|\,\mathrm{d}\tau}, \tag{3.18}$$

where E is the total energy spent in the actuators and d is the energy required by the force of gravity to displace the swimmer from its origin to its current position.

Fig. 3.13 displays the evolution of the CoT as the anguilliform swimmer progresses through the fluid. We hide the first swimming period when the fish is very close to its initial position to avoid presenting results of a division by numbers close to zero. It seems to converge to a value close to 20%. The cost of transport of this specific simulation will serve as a reference for the experiments of the next Section.

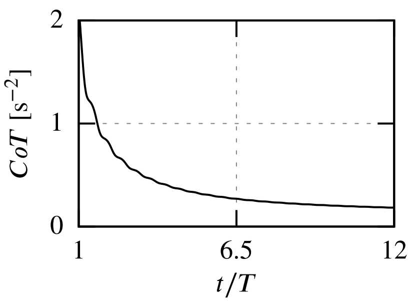

Figure 3.13: CoT of the anguilliform swimmer swimming in a straight line.

3.4.3 Multiple swimmers

To complete the analysis of the cohesive swimming experiments, we compare the travelled distance, spent energy and cost of transport of each individual of a school to the reference case of the individual swimmer performing the deformation given by Eq. (2.28).

We start by having a look at the CoT of the pair of swimmers following an in-phase and anti-phase deformation signal. In both configurations, swimming in pair results in a range increase close to 2.5%. Swimmers of both tests also end up saving energy in comparison to the single swimmer experiment. In the in-phase case, the energy of the top swimmer settles to a higher level relative to the reference case than the bottom swimmer. The difference is close to 0.5%. This asymmetry emerges from the asymmetry inherent to the initial swimming period where the beating amplitude continuously increases and misaligns the swimming direction from the initial orientation of the fish. The energy savings result in an improvement in CoT of around 3% in the established swimming regime. In the in-phase situation, this difference even increases to 4% for the bottom swimmer swimming in phase with its partner. On the other hand, the anti-phase swimming couple of swimmers display an almost perfect symmetry, as would be expected. In that case however, during the first half of the simulation, both fish must supply more energy to their actuators to perform the reference swimming gait. Ultimately, they demonstrate marginally better energy gains but travel further than would a single swimmer.

We also examine these indicators for both schools of five swimmers studied in Chapter 2. They are presented in Fig. 3.15. Once again, swimming in a group increases the traveled distance and enhances the swimming efficiency.

The aligned swimmers all go 9% further than would a single swimmer in the same conditions. However, the energy expenditures, although being smaller than reference, depend on the relative position of the swimmer with respect to the school: fish located at the sides of the formation display higher energy levels than individuals having a neighbour on each of their sides. The penalty of having a single neighbour represents approximately 0.5% of the energy budget of a single swimmer. This penalty is quite similar if we examine the cost of transport. However, the same asymmetry appears between the bottom and the top individuals as was the case in the pair of in phase swimmers.

The staggered formation swims 11% – 12% further than a single fish. A remarkable phenomenon appears on the energy ratio: a bit sooner than the middle of the

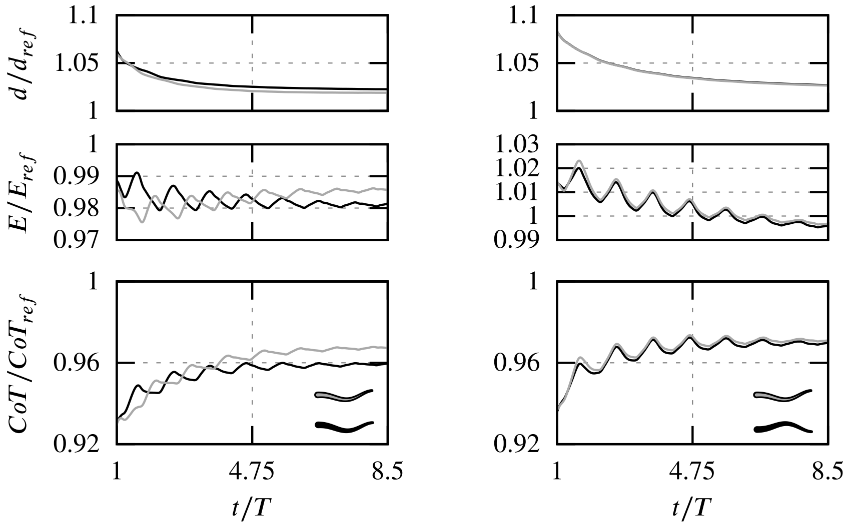

Figure 3.14: Ratio of travelled distance, spent energy and CoT's between the individuals of a pair of numerical anguillas swimming in phase (left) and anti-phase (right) and the reference case involving a single swimmer.

simulation, both bottom follower swimmers must suddenly provide more energy than the leader while top individual require less energy to go that far. This asymmetry is actually caused by the swimmers having to pass over the starting vortex shed by their leading neighbours (see Fig. 2.38b). Once this vortex is overcome, all members of the school exhibit smaller energy expenditures than reference, even the leader of the school which is somehow pushed by its followers in the incompressible flow. The inter-swimmer spread of energy spendings is lower than the spread observed in the inline formation and looks convergent after the starting vortices are passed. The spread in CoT is also contained in closer bounds than in the inline formation where both energy and CoT spreads are divergent.

3.5 Direct control through joint actuators

Controlling a swimmer through its articulations is a much more cumbersome task than imposing its kinematics and measuring the resulting actuation moments. This is because the system of equations involved in the time integration becomes much larger and much less stable, since Eq. (3.11) needs to be solved for the second derivatives of

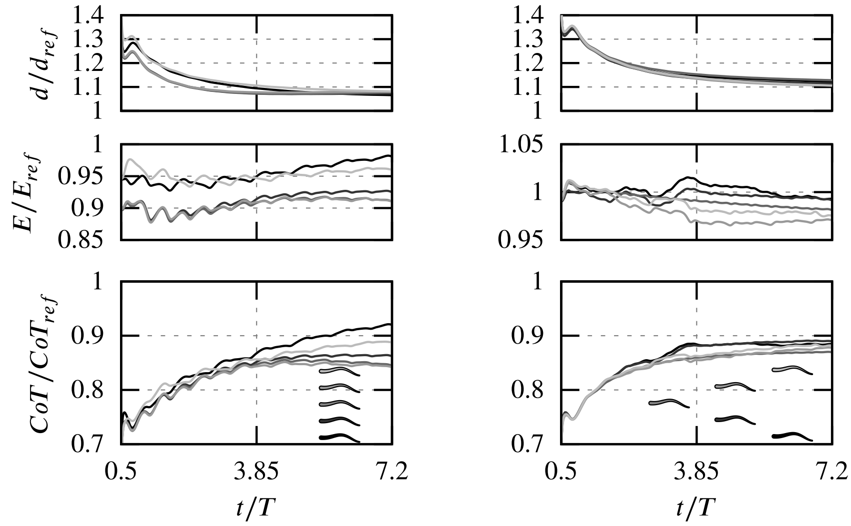

Figure 3.15: Ratio of travelled distance, spent energy and CoT's between the individuals of a school of five numerical anguillas swimming in phase from an initially aligned (left) and staggered (right) position and the reference case involving a single swimmer.

the generalized coordinates:

$$\ddot{\boldsymbol{q}} = \boldsymbol{D}^{-1}\big((\boldsymbol{\tau}_h + \boldsymbol{\tau}_a) - \boldsymbol{C}(\boldsymbol{q}, \dot{\boldsymbol{q}})\dot{\boldsymbol{q}}\big), \tag{3.19}$$

where the first two equations in that system actually represent the equilibrium of linear momentum of the entire swimmer and all others represent the angular equilibrium of every link of the swimmer.

The absence of any dissipative term in Eq. (3.19) is presumably responsible for its instability and confronts the numericist with a substantial challenge. To overcome this instability, we use the same strategy with the added mass, as was done in Chapter 2, to artificially introduce dissipation into the system.

This time however, the added mass matrix has rank $n = N + 2$ as the actuation of each degree of freedom has an impact on the impulse associated with each other degree of freedom. This is what Kanso et al. [32] referred to as *hydrodynamic coupling*; their definition formally defines the added mass terms as the influence of the motion of one given link on the impulse around any other while satisfying physical constraints. This effectively results in an added mass matrix with a rank equal to the number of degrees of freedom of the system. Finding an expression for this added mass matrix is the endeavour of the following Section. However, the matrix is input in the equilibrium equation for numerical stabilization purposes only, as shown in Eq. (2.17), which is not equivalent to the physically sound equilibrium of Eq. (2.16) (and of Appendix D). This difference is physically materialized by the absence of a significant term in Eq. (2.17) and can affect the coupling between degrees of freedom. With this in mind, we now modify the derivation of Section 2.1.1 to take internal degrees of freedom into account.

3.5.1 Added mass for an N-link articulated body

In the forthcoming development, the swimmer has internal degrees of freedom $\boldsymbol{\theta}$, where θ_1 is the global angular position of the body. The velocity potential decomposition becomes

$$\varphi(\boldsymbol{x}) = \dot{\boldsymbol{x}}_{cm} \cdot \boldsymbol{\zeta}(\boldsymbol{x}) + \dot{\boldsymbol{\theta}} \cdot \boldsymbol{\chi}(\boldsymbol{x}). \tag{3.20}$$

The first step to rewrite a boundary condition for the velocity potential is to give an expression for the body surface velocity as a function of all degrees of freedoms. We have:

$$\boldsymbol{u}_b(\boldsymbol{x}) = \left(\dot{\boldsymbol{x}}_{cm} + \sum_{i=1}^{j} \dot{\theta}_i \hat{\boldsymbol{e}}_z \times (\boldsymbol{x} - \boldsymbol{x}_{r,i}) - \dot{\boldsymbol{x}}(\dot{\boldsymbol{\theta}}) \right), \tag{3.21}$$

where $\boldsymbol{x} \in \mathcal{S}_j$, i.e. the surface of the j-th link. In other words, the velocity of a material point on the surface of the j-th link depends on: (i) the translation of the overall center of mass, (ii) the angular velocity of link j cumulated from all preceding links and (iii) the linear recoil correction denoted by the term $\dot{\boldsymbol{x}}(\dot{\boldsymbol{\theta}})$. This time it accounts for the translation velocity to superimpose to the deformation velocity of all segments to guarantee the whole system has zero momentum, the angular recoil being already taken care of by $\dot{\theta}_1$. The linear recoil has a linear dependency on the rate of change of the internal degrees of freedom

$$\frac{\mathrm{d}}{\mathrm{d}t} \boldsymbol{x}(\boldsymbol{\theta}(t)) = \frac{\partial \boldsymbol{x}}{\partial \boldsymbol{\theta}} \dot{\boldsymbol{\theta}} = -\boldsymbol{A} \cdot \dot{\boldsymbol{\theta}}, \tag{3.22}$$

obtained by manipulating the time derivative of expression Eq. (2.20). We draw the reader's attention to the fact that this linear dependency is mathematically sound in the case of the N-link swimmer but remains approximative for the continuous swimmer.

Injecting Eq. (3.22) into Eq. (3.21), the boundary condition becomes

$$\frac{\partial \varphi}{\partial n} = \left(\dot{\boldsymbol{x}}_{cm} \cdot \frac{\partial \boldsymbol{\zeta}}{\partial n} + \dot{\boldsymbol{\theta}} \frac{\partial \boldsymbol{\chi}}{\partial n} \right) = \left(\dot{\boldsymbol{x}}_{cm} + \sum_{i=1}^{j} \dot{\theta}_i \left(\boldsymbol{a}_i + \hat{\boldsymbol{e}}_z \times (\boldsymbol{x} - \boldsymbol{x}_{r,i}) \right) + \sum_{i=j+1}^{N} \dot{\theta}_i \boldsymbol{a}_i \right) \cdot \boldsymbol{n}, \tag{3.23}$$

where $\boldsymbol{a}_i$ is the i-th column of Jacobian $\boldsymbol{A}$. We can now write

$$\frac{\partial \boldsymbol{\zeta}}{\partial n} = \boldsymbol{n}, \tag{3.24}$$

$$\frac{\partial \chi_k}{\partial n} = \begin{cases} \boldsymbol{a}_k \cdot \boldsymbol{n} + [(\boldsymbol{x} - \boldsymbol{x}_{r,k}) \times \boldsymbol{n}] \cdot \hat{\boldsymbol{e}}_z & \text{if } k \leq j, \\ \boldsymbol{a}_k \cdot \boldsymbol{n} & \text{otherwise.} \end{cases} \tag{3.25}$$

Finally, we obtain the added mass matrices:

$$M^{\zeta\zeta}_{kl} = - \oint_{\mathcal{S}_b} \zeta_l \boldsymbol{n} \, \mathrm{d}S \cdot \hat{\boldsymbol{e}}_k, \tag{3.26}$$

$$M^{\zeta\chi}_{kl} = - \oint_{\mathcal{S}_b} \chi_l \boldsymbol{n} \, \mathrm{d}S \cdot \hat{\boldsymbol{e}}_k, \tag{3.27}$$

$$M^{\chi\zeta}_{kl} = - \oint_{\mathcal{S}_b} \zeta_l \boldsymbol{n} \, \mathrm{d}S \cdot \boldsymbol{a}_k - \oint_{\cup_j \mathcal{S}_{j \geq k}} (\boldsymbol{x} - \boldsymbol{x}_{r,k}) \times \zeta_l \boldsymbol{n} \, \mathrm{d}S \cdot \hat{\boldsymbol{e}}_z, \tag{3.28}$$

$$M^{\chi\chi}_{kl} = - \oint_{\mathcal{S}_b} \chi_l \boldsymbol{n} \, \mathrm{d}S \cdot \boldsymbol{a}_k - \oint_{\cup_j \mathcal{S}_{j \geq k}} (\boldsymbol{x} - \boldsymbol{x}_{r,k}) \times \chi_l \boldsymbol{n} \, \mathrm{d}S \cdot \hat{\boldsymbol{e}}_z, \tag{3.29}$$

where both $\boldsymbol{M}^{\zeta\zeta} \in \mathbb{R}^{2\times 2}$ and $\boldsymbol{M}^{\chi\chi} \in \mathbb{R}^{N \times N}$ are symmetric and $M^{\zeta\chi}_{kl} = M^{\chi\zeta}_{lk}$.

The interpretation of these terms is the following: the first two lines of the global added mass matrix represent the linear impulse of the whole swimmer when each degree of freedom has a unitary input. The third line ($k = 1$ and $\boldsymbol{a}_k = \boldsymbol{0}$) represents the angular impulse of the whole swimmer expressed in its global center of mass when each degree of freedom has a unitary input. Finally, subsequent lines ($k > 1$) consist in the superposition of the angular impulse of the rotating links ($j \geq k$) expressed in a frame centered at joint k and the dot product of the linear impulse of the whole articulated chain with the position vector $\boldsymbol{a}_k$. This vector, when multiplied with $\dot{\theta}_k$ gives the translational velocity of the global center of mass of the body to guarantee linear recoil when θ_k only is actuated.

3.5.2 Open loop control of the 3-link swimmer

We now try out this more entangled dynamical system with a simple open-loop control law with the already familiar 3-link swimmer. To keep things as simple as possible, we will attempt to replicate the results obtained in Section 2.2 by imposing the loads observed in Section 3.4.1 in the actuators of the multi-body system.

The way this is achieved relies on approximating the reference actuation signal with a Fourier series, hereby creating a mapping $\mathbb{R} \to \mathbb{R} : t \mapsto \tau_i(t)$ for each articulation. 150 pairs of coefficients were kept for each mapping. The reason for this mapping is the elimination of the need for reading data from files at each time step.

Because of the chaotic nature of the fluid-body dynamical system, the open-loop control law will inevitably produce collisions between the segments. To avoid this, the simulation is run for two swimming periods only. Snapshots are presented in Fig. 3.16.

(a) $t/T = 1.125$ (b) $t/T = 1.250$ (c) $t/T = 1.375$ (d) $t/T = 1.500$

(e) $t/T = 1.625$ (f) $t/T = 1.750$ (g) $t/T = 1.875$ (h) $t/T = 2.000$

Figure 3.16: Snapshots of the swimming gait over one swimming period when imposing actuation loads trying to replicate $\theta_2(t) = -\sin t/T$ and $\theta_3(t) = -\cos t/T$. The origin of the inertial frame of reference is represented with $\times$.

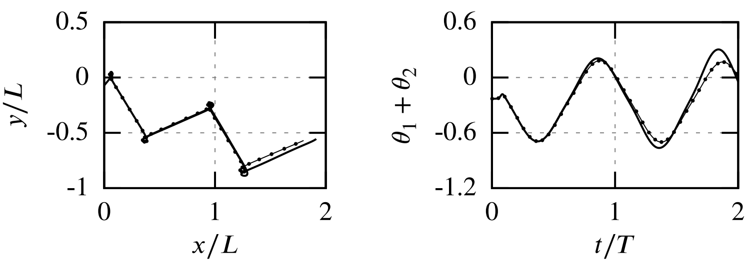

Figure 3.17: Trajectory followed by the 3-link swimmer and orientation of its middle segment when actuation moments are imposed. Comparison between direct (——) and inverse (—•—) dynamics.

The trajectory followed by the swimmer over this horizon time is very close to the trajectory observed in the inverse dynamics problem. This is shown in Fig. 3.17 where we also see the orientation of the middle segment of the swimmer. The similarity between trajectories in inverse and direct dynamics confirms the importance of the missing term in Eq. (2.17), responsible for the hydrodynamic coupling of internal degrees of freedom.

The exponential character of the error as time elapses is not only observable in the orientation of the middle link of the swimmer, but also on the right panel of Fig. 3.18 where the evolution of the generalized coordinates and their references are displayed along with their absolute difference.

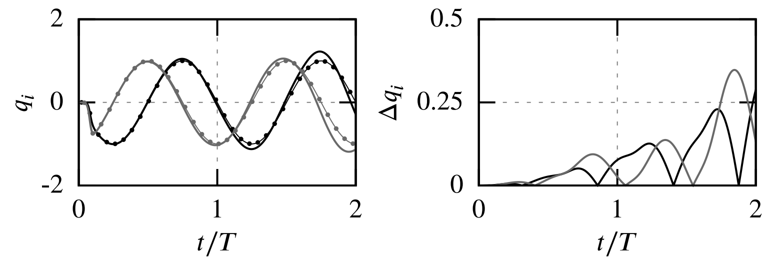

Figure 3.18: Comparison between the generalized coordinates q_4 (—) and q_5 (—) and their errors with the coordinates imposed in inverse dynamics (-•-).

We also compare the hydrodynamic forces and moments applied on the center of mass of all ellipses between the direct and inverse dynamics cases in Fig. 3.19. As one can see, all signals stay very close to their respective reference but start to significantly deviate during the second half of the second swimming period. This really exhibits the chaotic character of the system where only small external perturbations suffice to generate a very large difference in outcome, i.e. in the generalized coordinates of the multi-body system. However, simple closed-loop control strategies (like the use PID controllers [see 36]) can quite easily be introduced in the framework and make this specific swimming gait a stable orbit of the dynamical system.

3.5.3 Direct dynamics of a continuous anguilliform swimmer

The main difficulty of enabling the direct dynamics of the eel-like swimmer resides in the computation of the added mass matrix. Even though the proposed framework allows it, we have not managed to produce convincing simulations.

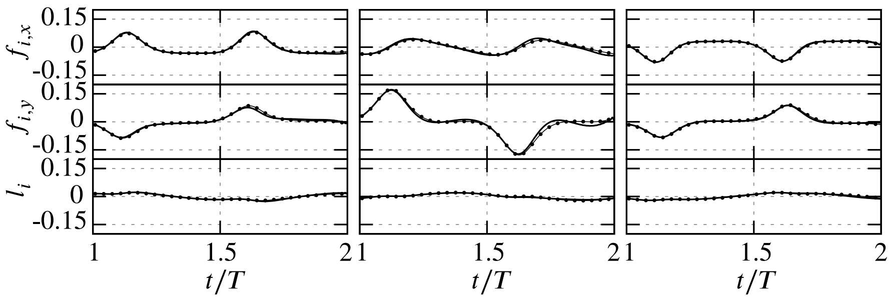

Figure 3.19: Hydrodynamic loads applied on the center of mass of segment 1 (left), segment 2 (middle), and segment 3 (right) of the 3-link swimmer. Comparison between direct (——) and inverse (—•—) dynamics.

The size increase and complexity inherent to the case of the continuous swimmer makes simulations very tedious. Their sensitivity is not only amplified by the smaller inertia of the thin segments composing the body, their number critically shift the eigenvalues of the system much further away from the stability region. In addition, the now flexible links can generate an imbalance in the added-mass matrix that can lose its symmetry as well as its semi-positive-definite property. This phenomenon leads to failure very fast when the imposed controls are inadequate. Additionally, trying to map simulation time with the observed actuation loads during inverse dynamics simulations by finding Fourier coefficients for as many as 63 articulations seemed impractical.

However, we still believe direct dynamics of one ore more anguilliform swimmers is possible with our framework but will still require much time and effort.

3.6 Discussion

This Chapter introduced a model for solving the internal mechanics of a swimmer. To be more specific, it creates a mapping between the kinematics of the multi-body system and the moments exerted on its actuators. The model was validated with *Robotran* and even outperforms it in the case of the anguilliform swimmer.

Using this model, we showed that the bending moments of a continuous eel-like swimmer follow are very close to a single-mode standing wave along the spine of the body. Additionally, we could recover the power and energy dissipated in the actuators of the swimmers and use a well-known a metric for assessing swimming efficiency.

We discovered that swimming with others is always a better alternative than swimming alone, both in terms of travelled distance and energy expenditure. This is true for both parallel and staggered formations, in phase or phase opposition swimming gaits. According to our model, swimmers benefit from interacting with peers even in the absence of any control law. We could easily imagine how even simple control laws could further optimize groups of swimmers. We think for instance of a leader-follower formation where the follower navigates in the wake of the leader in order to extract forward momentum.

We closed the Chapter by running direct dynamics simulations of the 3-ellipse swimmer. The proximity between results of inverse and direct dynamics happens to be very promising for direct dynamics control frameworks relying on reference trajectories and actuation signals extracted from their inverse dynamics counterpart, even though further experiments are still necessary to introduce some hydrodynamic coupling between internal degrees of freedom.

CHAPTER 4

Aggregating free vorticity

The flow model presented in Chapter 1 has a significant drawback: the ambient vorticity in the flow is represented by an ever increasing number of elements: as time marches, more and more point vortices are produced in the unbounded domain. This linearly growing number of vortex elements implies the resolution of increasingly larger N-body problems, making the investigation of long-term flow behaviour impractical.

To alleviate the increase in complexity, Tchieu and Leonard [64] and Wang and Eldredge [74] proposed to avoid the production of a vortex element at each time step by a process called impulse matching, i.e. feeding vorticity into already existing point vortices, keeping the most coherent vortical structures only. Because the natural instability of shear layers favours the formation of larger scale structures, such models fail at representing flows at long horizon times with accuracy. Another technique relies on merging a pair of neighbouring vortices into one another. In the work of Xia and Mohseni [79], the merging operation is carried out under the condition that the Taylor expansions of both near and far-field are not altered by the aggregation. This double condition translates into a modification of both position and velocity of the point vortex resulting from the merging operation. More recently, Darakananda and Eldredge [13] corrected the velocity of the resulting vortex in order to exactly cancel the spurious force induced by the local change of circulation around the vortex pair. They qualified their model as hybrid since the proportion of the vortex sheet to lump into the roll-up point vortex depends on a parameter left at the discretion of the user. Even though this model seems more attractive because it does not rely on Taylor expansions of the velocity field, a spurious moment on the flat plate appears. With this framework, spurious force and moment cannot be cancelled simultaneously.

All of the aforementioned efforts have led to lower-order models that are applicable to the case of a flat plate. To our knowledge, the sole effort toward the handling of a generic airfoil geometry is the derivation by Eldredge [18] of a complex analysis expression for vorticity aggregation (see Eq. (7.45) of aforementioned reference). The present Chapter aims at filling this gap through a work on the real-valued expressions of impulse matching and from there, the construction of a numerical scheme capable of handling generic airfoil geometries with a finite angle trailing edge. This work has been published in [15]. For the sake of straightforwardness, we only treat the case of a single shedding source, i.e. at the trailing edge; this allows us to base our shedding scheme on the unsteady Kutta condition derived by Xia and Mohseni [80].

The remainder of this Chapter is organized as follows: In Section 4.1, we present the transfer of circulation between the wake vortex sheet and the aggregated roll-up vortex generalized for flows around airfoils with a wedge-shaped trailing edge. Section 4.2 shows the validation of our framework through comparisons with computational and experimental results: cases of an impulsively started and a heaving and pitching airfoils are studied. We summarize and discuss these results in Section 4.3.

4.1 Impulse matching for general wedged-trailing-edge geometries

In previous studies, Wang and Eldredge [74] and Darakananda and Eldredge [13] have developed low-order models for the roll-up of the vortex sheets shed by a moving flat plate. The second of these studies has shown that transferring vorticity from source point $\boldsymbol{x}_s$ to target point $\boldsymbol{x}_t$ induces a spurious force due to the local violation of Kelvin's conservation of circulation around both points. Indeed, point $\boldsymbol{x}_t$ undergoes a change of circulation of rate $\dot{\Gamma}_t$ and point $\boldsymbol{x}_s$ a change of opposite rate. Therefore, they proposed to cancel the resulting parasitic force by correcting the velocity of the target particle

$$\Delta\dot{\boldsymbol{x}}_t = \frac{\dot{\Gamma}_t}{\Gamma_t}\left(\frac{\mathrm{d}\hat{\boldsymbol{p}}(\boldsymbol{x}_t)}{\mathrm{d}\boldsymbol{x}_t}\right)^{-1}\left[\hat{\boldsymbol{p}}(\boldsymbol{x}_s) - \hat{\boldsymbol{p}}(\boldsymbol{x}_t)\right], \tag{4.1}$$

where $\hat{\boldsymbol{p}}(\boldsymbol{\xi})$ is introduced as the impulse due to a point vortex of unit circulation located at $\boldsymbol{\xi}$

$$\hat{\boldsymbol{p}}(\boldsymbol{\xi}) = \boldsymbol{\xi}\times\hat{\boldsymbol{e}}_z + \int_{\mathcal{S}_b} \boldsymbol{x}(s)\times\hat{\boldsymbol{\gamma}}(s)\,\mathrm{d}S, \tag{4.2}$$

$\hat{\boldsymbol{\gamma}}(s)$ being the so-called unit image vortex sheet associated to this point vortex on $\mathcal{S}_b$.

The main drawback of this strategy is the impossibility to cancel both the spurious force and moment caused by the displacement of vorticity. Hence, cancelling the spurious force will inevitably result in a spurious moment with respect to the origin of the inertial frame given by

$$\Delta \boldsymbol{m}_{\mathbf{0}} = -\frac{\rho \dot{\Gamma}_t}{2} \left[\frac{\mathrm{d}\hat{\boldsymbol{l}}_{\mathbf{0}}(\boldsymbol{x}_t)}{\mathrm{d}\boldsymbol{x}_t} \left(\frac{\mathrm{d}\hat{\boldsymbol{p}}(\boldsymbol{x}_t)}{\mathrm{d}\boldsymbol{x}_t} \right)^{-1} [\hat{\boldsymbol{p}}(\boldsymbol{x}_s) - \hat{\boldsymbol{p}}(\boldsymbol{x}_t)] + [\hat{\boldsymbol{l}}_{\mathbf{0}}(\boldsymbol{x}_t) - \hat{\boldsymbol{l}}_{\mathbf{0}}(\boldsymbol{x}_s)] \right], \tag{4.3}$$

where the unit angular impulse at the origin due to a vortex located at $\boldsymbol{\xi}$ is

$$\hat{\boldsymbol{l}}_{\mathbf{0}}(\xi) = \boldsymbol{\xi} \times (\boldsymbol{\xi} \times \hat{\boldsymbol{e}}_z) + \int_{\mathcal{S}_b} \boldsymbol{x}(s) \times (\boldsymbol{x}(s) \times \hat{\boldsymbol{\gamma}}(s))\, \mathrm{d}S. \tag{4.4}$$

Darakananda and Eldredge [13] applied thin airfoil theory to derive the analytical velocity correction in the case of the flat plate. In the panel-based model we propose, however, such an analytical derivation is impossible for the Jacobian in Eq. (4.1) must be obtained numerically. The Jacobian of the unit impulse is the following:

$$\frac{\mathrm{d}\hat{\boldsymbol{p}}(\xi)}{\mathrm{d}\boldsymbol{\xi}} = \begin{bmatrix} 0 & 1 \\ -1 & 0 \end{bmatrix} + \int_{\mathcal{S}_b} \begin{bmatrix} y(s) \\ -x(s) \end{bmatrix} \nabla_{\xi} \hat{\boldsymbol{\gamma}}(s)\, \mathrm{d}S. \tag{4.5}$$

The only missing piece in this expression is the gradient of the bound sheet circulation $\hat{\boldsymbol{\gamma}}(s)$ on a contour $\mathcal{S}_b$ of general shape. It represents the sensitivity of the bound vortex sheet to a change in position of a free point vortex of unit circulation.

Because the lumping operation is performed at the end of a time step (i.e., when the shed panel is replaced by a point vortex), we can take the gradient of Eq. (1.31) to obtain $\nabla_{\xi}\hat{\boldsymbol{\gamma}}$. Since the total circulation is conserved throughout the merging of vortices and because matrix $\tilde{A}$ (see Eq. (1.31)) does not depend on $\boldsymbol{\xi}$ but solely on the relative positions of the bound panels, the gradient on the body surface reduces to

$$\left[\nabla_{\xi}\hat{\boldsymbol{\gamma}}\right] = \tilde{A}^{-1} \left[\frac{\nabla_{\xi}\hat{\chi}}{0} \right], \tag{4.6}$$

where $\tilde{A}^{-1}$ has already been computed in the no-flow-through condition determining the bound vortex strength and where the induced normal velocity gradient $\nabla_\xi \hat{\chi}$ has to be obtained at the collocation point of each panel. For panel j, we have

$$\nabla_\xi \hat{\chi}_j = \nabla_\xi \Big(\boldsymbol{n}_j \cdot \big(\boldsymbol{K}^*(\boldsymbol{x}_j - \xi) \times \hat{\boldsymbol{e}}_z \big) \Big), \tag{4.7}$$

which is obtained analytically in the frame of reference of panel j.

First of all, the lumping operation is only allowed between vortex elements of the same sign. Furthermore, even though the merging of point vortices itself is carried out in a way to cancel spurious forces, the main structure of the flow is altered in the vicinity of the transfer of vorticity. This change in flow topology results in a different solution for the motion of vortex elements computed over a time step. This in turn causes both the global impulse and the force on the airfoil to drift away from the values which would result from an unperturbed vorticity field. To control this discrepancy and in line with the work of [13], we use a parameter $\boldsymbol{B_F}$ that serves as a threshold on the scaled force discrepancy between the state of the system after a time step with vorticity transfer and the state observed after the same time step with equal initial condition but without transfer. For a rigorous definition for $\boldsymbol{B_F}$, consider a simulation at time $t = T$ whose representational state is defined by $\mathcal{S}(T)$. Then at time $t = T + \Delta t$, the simulation can reach two different states whether vorticity aggregation has occurred at $t = T$ or not. These states are respectively referred to as $\mathcal{S}'(T + \Delta t)$ and $\mathcal{S}(T + \Delta t)$. Then, the parameter $\boldsymbol{B_F}$ is an upper bound for the force discrepancy between both possible states.

$$\boldsymbol{B_F} \geq \frac{\frac{1}{2}\|\Delta \boldsymbol{f}\|}{\frac{1}{2}\rho c \boldsymbol{U}_\infty^2}, \tag{4.8}$$

where $\|\Delta \boldsymbol{f}\| = \|\boldsymbol{f}\big(\mathcal{S}'(T + \Delta t)\big) - \boldsymbol{f}\big(\mathcal{S}(T + \Delta t)\big)\|$. If inequality (4.8) holds, then the vorticity aggregation procedure is allowed: $\mathcal{S}'$ is kept and $\mathcal{S}$ is discarded. Otherwise, $\mathcal{S}$ is retained and no aggregation takes place. The choice in $\boldsymbol{B_F}$ balances the representational accuracy of the flow with the computational efficiency of the method. Indeed, low values of $\boldsymbol{B_F}$ will result in more resolved vortex sheets while large $\boldsymbol{B_F}$ values are associated with coarser wake structures. One can readily identify a lower bound for N_v: the number of lumped vortices can go as low as the number of sign changes in the shed vorticity plus an initial vortex. Once this bound is reached at a particular $\boldsymbol{B_F}$ level, further increasing the threshold has no effect on the structure of the wake anymore. It follows that the behavior of N_v with respect to $\boldsymbol{B_F}$ will be flow-specific.

This model embeds two other parameters: the minimal vortex sheet length, described by the minimum number of shed point vortices N_{min} before which no lumping can occur whatsoever and the minimum time interval T_{min} within which no new vortex can be shed from the tip of the vortex sheet. Parameter N_{min} allows to keep unaltered the coherent structure of the velocity close to the airfoil while T_{min} aims at avoiding instabilities in the vicinity of the vortex sheet tip. The influence of these two parameters on the resulting vortical structure of the wake is much less significant than the sensitivity on B_F. Therefore, in the following simulation, their value is fixed to $T_{min} = L_{min} = 25$.

4.2 Results and validation

The extension of the model presented above is now validated on the same benchmarks as in Chapter 1.

4.2.1 Impulsively started NACA0012

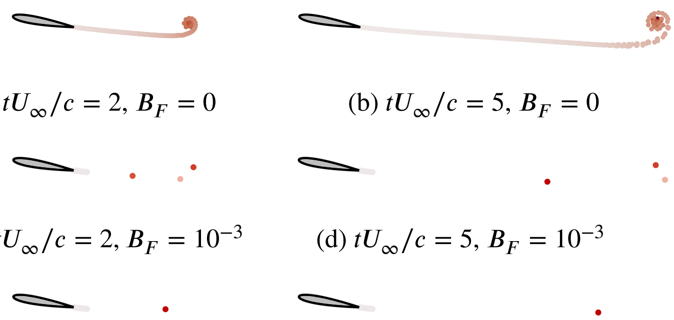

(a) $tU_\infty/c = 2$, $B_F = 0$ (b) $tU_\infty/c = 5$, $B_F = 0$

(c) $tU_\infty/c = 2$, $B_F = 10^{-3}$ (d) $tU_\infty/c = 5$, $B_F = 10^{-3}$

(e) $tU_\infty/c = 2$, $B_F = 10^{-2}$ (f) $tU_\infty/c = 5$, $B_F = 10^{-2}$

Figure 4.1: Impulsively started NACA0012 airfoil at $\alpha = \pi/18$. Effect of vorticity aggregation for different values of the error threshold B_F. Other parameters are fixed to $T_{min} = L_{min} = 25$.

We first compare the influence of the parameter B_F of the lumping model on the aerodynamic loads of the impulsively started NACA0012 at $\alpha = \pi/18$. Snapshots of simulations at two and five chord lengths of travel are presented in Fig. 4.1. The first case in which $B_F = 0$ corresponds to the standard unsteady panel method, later referred to as the baseline model. Increasing this parameter yields a dramatic reduction in the number of point vortices in the wake. At $B_F = 10^{-3}$, the wake is only captured by means of $L_{min} + 3$ point vortices. Increasing this parameter beyond $B_F = 10^{-2}$ results in the formation of a unique point vortex corresponding to the starting vortex of the airfoil. The location of this point vortex corresponds to the vorticity-centroid of the wake, its velocity being affected as soon as it is fed vorticity.

Fig. 4.2 shows the aerodynamic coefficients up to ten chord lengths of travel computed with these different values of B_F. Because the lumping operation affects the angular momentum budget in the computational domain, $\boldsymbol{f}$ and $\boldsymbol{m}_{\boldsymbol{x}_{cm}}$ are computed using Eq. (1.40) and Eq. (1.41) following the control volume approach. When the parameter B_F is equal to or higher than 10^{-2}, the error in drag coefficient is smaller than 10%. The model predicts a lift coefficient that is higher by less than 2% of its final value while the moment coefficient is not accurately predicted at the early stage of the simulation.

The small loss of accuracy in lift and drag coefficients comes with a significant speedup in computational efficiency. Since the time complexity per time step scales quadratically with the number of vortex particles, limiting their number to $L_{min} + 1$ (instead of a linear increase up to 1000 at the end of the baseline simulation) keeps the cost constant throughout the whole simulation. The total speedup is in this case is close to 3.5.

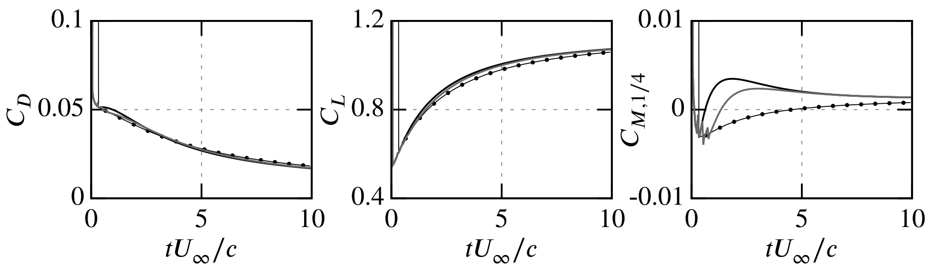

Figure 4.2: Impulsively started NACA0012 airfoil at $\alpha = \pi/18$. Aerodynamic coefficients obtained with the baseline model (—•—), and the lumping model with $T_{min} = L_{min} = 25$, $B_F = 10^{-2}$ (——) and $B_F = 10^{-3}$ (——).

Then, we present in Fig. 4.3 the scaled lift coefficient and bound circulation on the airfoil at different angles of attack when $B_F = 10^{-2}$ and compare them to the Wagner function. In both cases, results are in agreement with the theory.

Finally, results of computations at various angles of attack with $B_F = 10^{-2}$ are compared with the original model from [80] in Fig. 4.4. For any configuration, the lift coefficient agrees well even with a unique point vortex shed at the trailing edge.

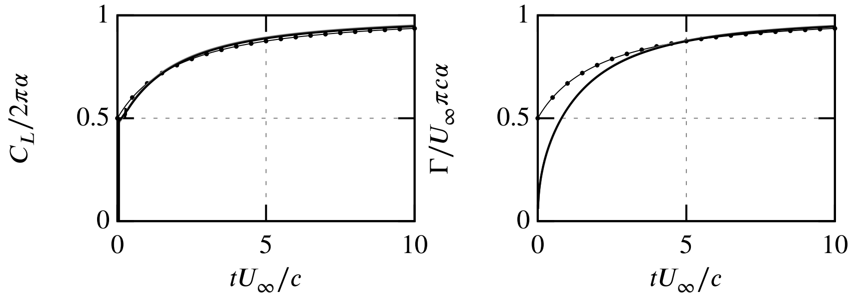

Figure 4.3: Impulsively started NACA0012 airfoil. Scaled lift coefficient and bound circulation with $T_{min} = L_{min} = 25$, $B_F = 10^{-2}$ at $\alpha = \pi/90$ (—), $\alpha = \pi/30$ (—) and $\alpha = \pi/18$ (—). Comparison with the Wagner function (-•-).

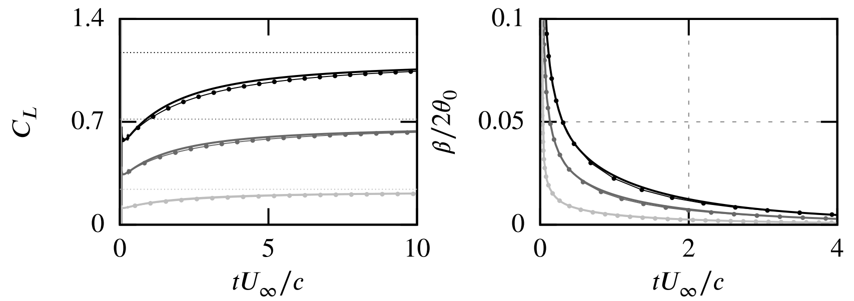

Figure 4.4: Impulsively started NACA0012 airfoil at $\alpha = \pi/90$ (—), $\alpha = \pi/30$ (—) and $\alpha = \pi/18$ (—). Comparison of the lift coefficient and the shedding angle between the lumping model with $T_{min} = L_{min} = 25$, $B_F = 10^{-2}$ (—) and the baseline model (-•-) along with steady values obtained with a potential flow solver (······). Shedding angle β is defined with respect to the bisector of the trailing edge; $\beta \in [-\theta_0, \theta_0]$.

4.2.2 Heaving and pitching NACA0012 and NACA0013

We first replicate the low amplitude experiment of Section 1.7.2 with $T_{min} = L_{min} = 25$ and $B_F = 10^{-1}$. The wake is compared to the baseline model in Fig. 4.5 where we can see how the aggregation model allows the reduction of the original 500-point-vortex wake into the coarsest possible representation of that vortical structure characterized by a single pair of point vortices per motion period. The aerodynamic coefficients are shown in Fig. 4.6 and suggest that, for all studied pitching amplitudes, the lumping procedure does not hinder the dynamics of the airfoil.

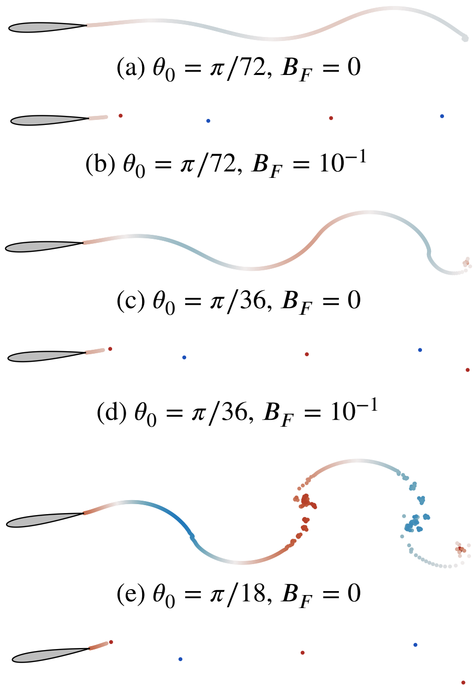

(a) $\theta_0 = \pi/72$, $B_F = 0$

(b) $\theta_0 = \pi/72$, $B_F = 10^{-1}$

(c) $\theta_0 = \pi/36$, $B_F = 0$

(d) $\theta_0 = \pi/36$, $B_F = 10^{-1}$

(e) $\theta_0 = \pi/18$, $B_F = 0$

(f) $\theta_0 = \pi/18$, $B_F = 10^{-1}$

Figure 4.5: Heaving and pitching NACA0012 airfoil towed at its quarter-chord with $\kappa = 1$ and $h = 1/40$ at $tU_\infty/c = 5$. Vortices colored by intensity for several aggregation parameters.

This last statement is reinforced by Fig. 4.7 where we show the thrust coefficient and efficiency obtained with vorticity aggregation and $B_F = 10^{-1}$ for all cases reproduced from [1] in Section 1.7.2.

We then move on to the heaving and pitching NACA0013 with parameters defined in [29]. First, we examine the effect of applying the lumping model on vorticity distribution in the wake of the airfoil. Fig. 4.8 shows snapshots of simulations where the error parameter B_F is set to either 0 , 10^{-3} or 10^{-1}, captured after one and a half motion periods. Past the highest tolerance level, the wake can once again be fully reduced to a pair of vortices of equal and opposite strength for each motion period. Their arrangement fits the characteristic structure of a thrust wake [see 53]. As a point of reference, the original model would generate 666 vortices per oscillation period with

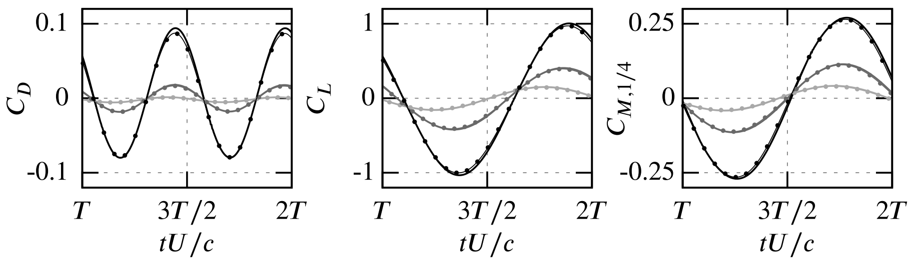

Figure 4.6: Heaving and pitching NACA0012 airfoil towed at its quarter-chord with $\kappa = 1$, $h = 1/40$ and $\theta_0 = \pi/72$ (—), $\theta_0 = \pi/36$ (—) and $\theta_0 = \pi/18$ (—). Aerodynamic coefficients for the vorticity aggregation model with $T_{min} = L_{min} = 25$ and $B_F = 10^{-1}$ and the baseline model (-•-).

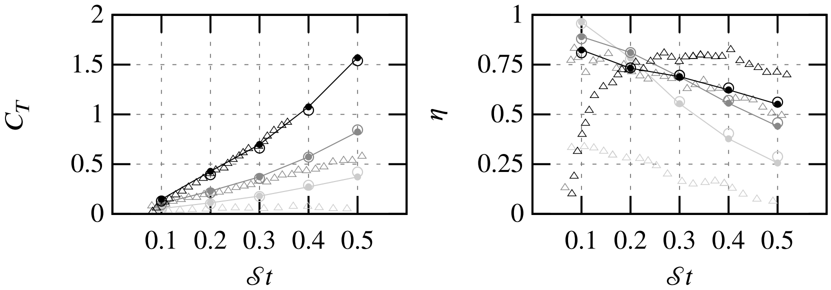

Figure 4.7: Heaving and pitching NACA0012 airfoil towed at its third-chord with $h = 0.75$, $\alpha_0 = \pi/36$ (-•-), $\alpha_0 = \pi/18$ (-•-) and $\alpha_0 = \pi/9$ (-•-). Thrust coefficient and efficiency as a function of the Strouhal number. Comparison of the vorticity aggregation model with $T_{min} = L_{min} = 25$ and $B_F = 10^{-1}$ (-•-) with the baseline model (∘) and experimental data of [1] (Δ).

the same set of simulation parameters (and 27 vortices per period with $B_F = 10^{-3}$). This allows a maximal reduction in the number of vortices by a factor larger than 300 compared to the baseline model, at the cost of slightly affecting the aerodynamic coefficients. This is shown in Fig. 4.9 where the lightest model is compared with the baseline. The error due to the most severe lumping procedure does not exceed 10% of the amplitude of the curves obtained with the baseline. Hence, independently of the choice of the force error threshold B_F and given the specific motion under examination, our lumping-enabled model is able to capture accurately the dynamics of the airfoil (see Fig. 4.8).

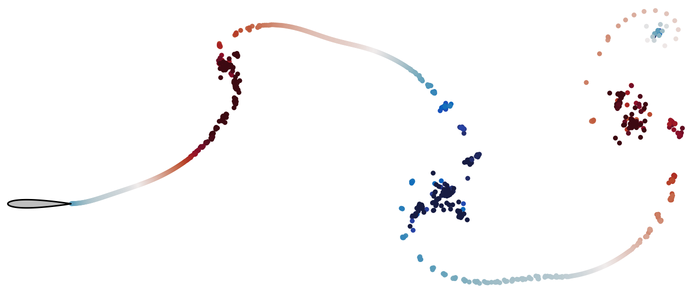

(a) $B_F = 0$

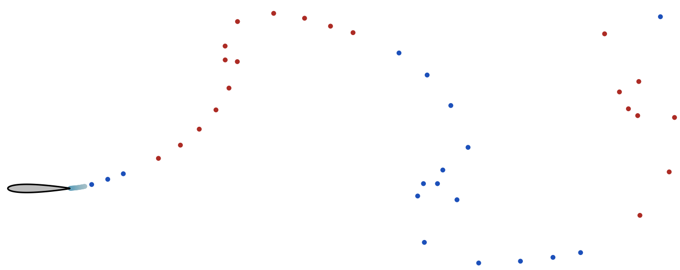

(b) $B_F = 10^{-3}$

(c) $B_F = 10^{-1}$

Figure 4.8: Heaving and pitching NACA0013 airfoil towed at its quarter-chord with $St = 0.3$, $h = 1$ and $\alpha_{max} = 5\pi/36$, $T_{min} = L_{min} = 25$. Vortices colored by intensity.

4.3 Discussion

In this Chapter, we have developed and validated the generalization of the hybrid model of Darakananda and Eldredge [13] for modeling flows separating from the trailing edge of general airfoils in unsteady motions. The model enables a user-controlled reduction of computational complexity by lumping circulation from one vortex element to an-

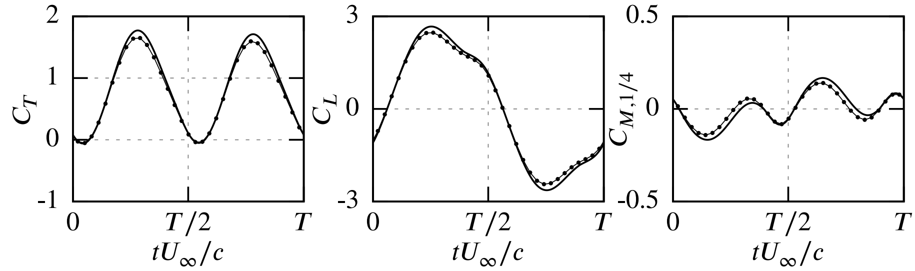

Figure 4.9: Heaving and pitching NACA0013 airfoil towed at its quarter-chord with $St = 0.3$, $h = 1$ and $\alpha_{max} = 5\pi/36$. Aerodynamic coefficients for the vorticity aggregation model with $T_{min} = L_{min} = 25$, $B_F = 10^{-1}$ (——) and the baseline model (—•—).

other without introducing any instantaneous force imbalance on the airfoil. This transfer of circulation could be applied to richer models embedding multiple bodies or/and LEV separation. To achieve the model extension, we have determined the net effect of the shape of the airfoil on the impulse of a point vortex. This contribution is computed through a recycling of the inverse of the matrix used in the standard unsteady panel method to determine the vortex strength distribution on the profile. This recycling allows a fast computation of the velocity correction the target vortex has to undergo in order to avoid spurious forces on the body. The remaining computational effort lies in calculation of the force error caused by the transfer of circulation between vortices over a time step.

We have validated this model on several benchmarks: an impulsively started NACA0012 and heaving and pitching NACA0012 and NACA0013 airfoils with different motion parameters. In three of these cases, we showed the effect of lumping vortices on the vorticity distribution in the wake of the airfoils. The main structure of the wake was conserved even though far fewer vortex elements were required to describe it. In the limit of acceptable accuracy, one single point vortex per roll-up core of the wake vortex sheet is necessary. Such an important dimensionality reduction accompanies a significant speedup allowing for real-time simulations. In addition, aerodynamic forces corroborate results obtained with the original panel method presented in Chapter 1 for every case studied therein. The lumping operation has shown to only degrade accuracy in the moment coefficient at early stages of a simulation if a very large transfer of circulation occurs between the body and the starting vortex close to the body surface. This significant degradation was not observed in the case of the heaving and pitching airfoil because the airfoil is initially parallel to its towing motion and the generation of circulation in the flow is much more progressive than in the case of the impulsively started airfoil with a non-zero angle of attack. Therefore, in cases of unsteady motion of an airfoil shedding vorticity continuously from its trailing edge and without leading edge separation, our model is fully capable of capturing essential dynamics of the flow and predict the aerodynamic loads on the immersed body while offering the user the freedom to adjust balance between accuracy and computational time.

CHAPTER **5**

Conclusions and perspectives

Throughout this work, we designed and implemented block-by-block a complete framework for low-order simulations of planar eel-like swimmers. This computational system enables simulations of one or multiple flexible swimmers the control of which can either be governed by body curvature or through the internal bending moments of the swimmer. Such insight on internal mechanics of swimmers allowed us to reveal the energetic aspects of anguilliform locomotion and discover that even naive collective swimming strategies without control led to improvement in swimming performance.

We now summarize the contributions of the present Manuscript and propose prospective improvements of the methods in use and simulation framework.

5.1 Contributions

The first contribution is the development of a framework for unsteady airfoils with vortex shedding. It extended the model it builds on [see 80] by enabling 4-th order precision for both numerical derivation and time integration. In addition, in the impenetrable body equation as well as in the expressions for the fluid impulse and its first moment, it explicitly isolates the contribution of the bound image-vortex from the potential and rotational contributions resulting from the rigid motion of the airfoil. Finally, we made the aerodynamic force/moment computations more modular either by solving for the pressure distribution or through a control volume approach. Deriving an expression for the aerodynamic moment in the latter approach is to the author's knowledge a pioneering result.

The framework served as a basis for the development of a potential flow model for simulating the locomotion of an articulated swimmer composed of a set of rigid elliptic bodies. We validated this framework with data from [32] in a case where each segment of the swimmer are hydrodynamically decoupled. This locomotion model has also been extended with the introduction of the vortex shedding model of the above paragraph in order to study the locomotion of one or more anguilliform swimmers. In the limit of its representativeness, we validated the model using results obtained from high-accuracy CFD models. This leads us to answer positively to our first research question: a low-order model can indeed approximate the dynamics of a school of fish. Of course, we acknowledge the limitation of our model since it misses many flow structures and patterns associated with three-dimensional flows and viscous dissipation. For instance, it will never be able to represent the propulsive vortex rings typically observed in wakes of three-dimensional swimmers. However, given its modularity, models for phenomena such as leading-edge separation could be added into our framework but this addition would not really serve the needs of aquatic locomotion.

To answer to the second research question, we created a fast and generalist Euler-Lagrange solver enabling both direct and inverse dynamics of swimmers by creating a mapping between body kinematics and bending moments. Validated with *Robotran* on the 3-link swimmer swimming in vacuum and in a perfect fluid as well as on the case of a anguilliform swimmer in vacuum, the MBS solver revealed a lack of conservation of angular momentum under the form of nonzero bending moment at the head of the swimmer when it evolved inviscid flow. This error is thought to emerge from numerical errors associated with the imposition of angular recoil correction to the deformation gait. This mapping between deformation and bending moments completes the library by not only revealing the power and energy expenditures of swimmers having prescribed deformation pattern, but also by allowing realistic simulations where actuation moments directly feed the model, paving the way for real control applications for one or a multitude of swimmers. These two different approaches bring answers to the third and fourth research questions: by prescribing simple swimming gaits to a small school of fish, this extension revealed that swimming individuals can benefit from being part of a school, even in the absence of any control on their swimming pattern.

The last contribution of this Thesis is the further improvement brought to the rigid airfoil model by allowing lumping operations on free vorticity. This expansion enables close to real time simulations and keeps the computational cost fairly low even for large time horizons thanks to its inherent lower-order representation of the wake shed by airfoils. The accuracy of the model did not suffer much in spite of the nonconservation of the angular momentum in the fluid. This is an important step to be transposed to the case of flexible self-propelling bodies, especially if one wishes to see data-driven control strategies such as Reinforcement Learning shed more light on the hidden mechanisms involved in marine biolocomotion.

5.2 Perspectives

As many research projects, this Dissertation ends with as many questions as answers. Every Chapter of it comes with its load of possible enhancements, which we present now only a small sample of.

The new proposed approach for the computation of aero/hydrodynamic moment based on a control volume approach relies on two assumptions: (i) a two-dimensional domain and (ii) an inviscid surrounding flow. We suggest a generalization of the control-volume-based moment derivation to three-dimensional flows in presence of viscosity. Though it could seem straightforward, additional terms intrinsic to three-dimensional vorticity dynamics (since in that case, $\boldsymbol{\omega} \times \hat{\boldsymbol{e}}_z \neq \mathbf{0}$) significantly increase the complexity and quantity of required analytic derivation.

The lumping procedure could be improved by annihilating the spurious moment caused by the coalescence of the source vortex into the target vortex. We believe that it can be done by adjusting the end position of the latter vortex in addition to its already corrected velocity. In the absence of the undesired discrepancy in the moment, we could embed the lumping procedure to the locomotion framework to significantly reduce its time complexity.

Continuing on the self-propulsion simulation framework, in the case of the discontinuous 3-link swimmer, results in the case of hydrodynamic coupling presented in [32] could not be achieved despite the acknowledgment of the effect of all degrees of freedom of the swimming system on its overall momentum. Further investigation, revolving around a separation of circulatory and acceleration-linked forces and the developments of Appendix D, could bridge the gap between our treatment of the added mass and a physically sound representation of the equilibrium equations enabling hydrodynamic coupling between internal degrees of freedom.

Since the pressure distribution on a body surface is provided by our model, the immersed body – whether rigid or flexible, driven or self-propelling – is capable of sensing the flow and its effect on its surface. This flow sensing ability could be used in different circumstances: either in the realm of load alleviation or for navigation purposes.

In addition to the direct dynamics of anguilliform swimmers, basic control strategies have yet to be implemented in the model. Methods such as Linear Control [see 36], Optimal Control Theory [see 35], Central Pattern Generators [see 45] or Reinforcement Learning [see 63] have already demonstrated their power in similar endeavours including actual robots or more accurate CFD models and are already available in off the shelf *julia* libraries. Such control designs could be used for optimizing the swimming gait of a unique swimmer in the absence or presence of external vortical perturbations, or for optimizing the spent energy of a swimmer in a school or even the energy spent by the entire school.

As is the case in many numerical systems, there must be many ways to accelerate the code. This is especially true for the present program whose initial aim was an extreme portability for data-driven controllers (i.e. Reinforcement Learning). In the locomotion model, the way of determining the body surface currently relies on the resolution of an ODE determining the position and velocity of the spine of the swimmer in order to keep control on the length of the body. We believe there are other and faster ways to do so: solving for position instead of curvature, then cutting the spine at the correct length may be less computationally demanding than solving a new ODE at each time step. Moreover, in case of periodic deformation patterns, one might want to store the surface information in memory after it is computed once and never compute it again. Attempts at reducing the computational cost of the fluid model using the Fast-Multipole Method [26] emerged but aborted before leading to reliable and consistent results. Using GPUs to solve for bound vorticity and to compute hydrodynamic vectorial data structures has also been considered.

Our framework can be further assessed using other fish geometries to replicate the experimental observations of marine biologists. More thorough analyses of swimming patterns can also be performed to confirm that an inviscid flow model with vortex shedding suffices to study the locomotion of eel-like swimmers.

Bibliography

[1] J. M. Anderson, K. Streitlien, D. Barrett, M. S. Triantafyllou, Oscillating foils of high propulsive efficiency, Journal of Fluid mechanics 360 (1998) 41–72.

[2] G. K. Batchelor, An Introduction to Fluid Dynamics, Cambridge Mathematical Library, Cambridge University Press, 2000.

[3] C. Bernier, M. Gazzola, P. Chatelain, R. Ronsse, Numerical simulations and development of drafting strategies for robotic swimmers at low reynolds number, in: 2018 7th IEEE International Conference on Biomedical Robotics and Biomechatronics (Biorob), IEEE, 378–383, 2018.

[4] C. Bernier, M. Gazzola, R. Ronsse, P. Chatelain, Simulations of propelling and energy harvesting articulated bodies via vortex particle-mesh methods, Journal of Computational Physics 392 (2019) 34–55, doi: https://doi.org/10.1016/j.jcp.2019.04.036.

[5] J. Bezanson, A. Edelman, S. Karpinski, V. B. Shah, Julia: A fresh approach to numerical computing, SIAM Review 59 (1) (2017) 65–98, doi: 10.1137/141000671.

[6] A. R. Blight, Undulatory swimming with and without waves of contraction, Nature 264 (5584) (1976) 352–354.

[7] F. Boyer, M. Porez, A. Leroyer, Poincaré–Cosserat equations for the Lighthill three-dimensional large amplitude elongated body theory: application to robotics, Journal of Nonlinear Science 20 (2010) 47–79.

[8] J. Carling, T. L. Williams, G. Bowtell, Self-propelled anguilliform swimming: simultaneous solution of the two-dimensional Navier–Stokes equations and Newton's laws of motion, Journal of experimental biology 201 (23) (1998) 3143–3166.

[9] J.-Y. Cheng, T. Pedley, J. Altringham, A continuous dynamic beam model for swimming fish, Philosophical Transactions of the Royal Society of London. Series B: Biological Sciences 353 (1371) (1998) 981–997.

[10] R. Clements, D. Maull, The representation of sheets of vorticity by discrete vortices, Progress in Aerospace Sciences 16 (2) (1975) 129–146, doi: https://doi.org/10.1016/0376-0421(75)90013-5.

[11] G.-H. Cottet, P. D. Koumoutsakos, et al., Vortex methods: theory and practice, vol. 313, Cambridge university press Cambridge, 2000.

[12] J. O. Dabiri, How fish feel the flow, Nature 547 (7664) (2017) 406–407.

[13] D. Darakananda, J. D. Eldredge, A versatile taxonomy of low-dimensional vortex models for unsteady aerodynamics, Journal of Fluid Mechanics 858 (2019) 917–948.

[14] N. Docquier, A. Poncelet, P. Fisette, ROBOTRAN: a powerful symbolic gnerator of multibody models, Mechanical Sciences 4 (1) (2013) 199–219, doi: 10.5194/ms-4-199-2013.

[15] D. Dumoulin, J. D. Eldredge, P. Chatelain, A lightweight vortex model for unsteady motion of airfoils, Journal of Fluid Mechanics 977 (2023) A22, doi: 10.1017/jfm.2023.997.

[16] J. D. Eldredge, Dynamically coupled fluid–body interactions in vorticity-based numerical simulations, Journal of Computational Physics 227 (21) (2008) 9170–9194.

[17] J. D. Eldredge, A reconciliation of viscous and inviscid approaches to computing locomotion of deforming bodies, Experimental Mechanics 50 (9) (2010) 1349–1353.

[18] J. D. Eldredge, Mathematical modeling of unsteady inviscid flows, vol. 50, Springer, 2019.

[19] C. Eloy, Optimal Strouhal number for swimming animals, Journal of Fluids and Structures 30 (2012) 205–218.

[20] L. Euler, Principes généraux du mouvement des fluides, Mémoires de l'académie des sciences de Berlin (1757) 274–315.

[21] F. Frenet, Sur les courbes à double courbure, Journal de mathématiques pures et appliquées 17 (1852) 437–447.

[22] M. Gazzola, P. Chatelain, W. M. Van Rees, P. Koumoutsakos, Simulations of single and multiple swimmers with non-divergence free deforming geometries, Journal of Computational Physics 230 (19) (2011) 7093–7114.

[23] M. Gazzola, A. A. Tchieu, D. Alexeev, A. de Brauer, P. Koumoutsakos, Learning to school in the presence of hydrodynamic interactions, Journal of Fluid Mechanics 789 (2016) 726–749.

[24] M. Gazzola, W. M. Van Rees, P. Koumoutsakos, C-start: optimal start of larval fish, Journal of Fluid Mechanics 698 (2012) 5–18.

[25] J. Gray, Studies in animal locomotion: I. The movement of fish with special reference to the eel, Journal of experimental biology 10 (1) (1933) 88–104.

[26] L. Greengard, V. Rokhlin, A fast algorithm for particle simulations, Journal of computational physics 73 (2) (1987) 325–348.

[27] P. Gunnarson, I. Mandralis, G. Novati, P. Koumoutsakos, J. O. Dabiri, Learning efficient navigation in vortical flow fields, Nature communications 12 (1) (2021) 7143.

[28] F. Hess, J. Videler, Fast continuous swimming of saithe (Pollachius virens): a dynamic analysis of bending moments and muscle power, Journal of Experimental Biology 109 (1) (1984) 229–251.

[29] J. S. Izraelevitz, M. S. Triantafyllou, Adding in-line motion and model-based optimization offers exceptional force control authority in flapping foils, Journal of Fluid Mechanics 742 (2014) 5–34.

[30] B. C. Jayne, G. V. Lauder, Are muscle fibers within fish myotomes activated synchronously? Patterns of recruitment within deep myomeric musculature during swimming in largemouth bass, Journal of Experimental Biology 198 (3) (1995) 805–815.

[31] E. Kanso, Swimming in an inviscid fluid, Theoretical and Computational Fluid Dynamics 24 (2010) 201–207.

[32] E. Kanso, J. E. Marsden, C. W. Rowley, J. B. Melli-Huber, Locomotion of articulated bodies in a perfect fluid, Journal of Nonlinear Science 15 (4) (2005) 255–289.

[33] J. Katz, A. Plotkin, Low-speed aerodynamics, vol. 13, Cambridge university press, 2001.

[34] S. Kern, P. Koumoutsakos, Simulations of optimized anguilliform swimming, Journal of Experimental Biology 209 (24) (2006) 4841–4857.

[35] D. E. Kirk, Optimal control theory: an introduction, Courier Corporation, 2004.

[36] H. Kwakernaak, R. Sivan, Linear optimal control systems, vol. 1, Wiley-interscience New York, 1972.

[37] H. Lamb, Hydrodynamics, 6th edition .

[38] G. Li, U. K. Müller, J. L. van Leeuwen, H. Liu, Body dynamics and hydrodynamics of swimming fish larvae: a computational study, Journal of Experimental Biology 215 (22) (2012) 4015–4033.

[39] R. Li, Q. Xiao, Y. Liu, J. Hu, L. Li, G. Li, H. Liu, K. Hu, L. Wen, A multi-body dynamics based numerical modelling tool for solving aquatic biomimetic problems, Bioinspiration & biomimetics 13 (5) (2018) 056001.

[40] M. J. Lighthill, Note on the swimming of slender fish, Journal of Fluid Mechanics 9 (2) (1960) 305–317, doi: 10.1017/S0022112060001110.

[41] M. J. Lighthill, Large-amplitude elongated-body theory of fish locomotion, Proceedings of the Royal Society of London. Series B. Biological Sciences 179 (1055) (1971) 125–138.

[42] S. J. Lighthill, Mathematical biofluiddynamics, SIAM, 1975.

[43] H. Liu, Integrated modeling of insect flight: from morphology, kinematics to aerodynamics, Journal of Computational Physics 228 (2) (2009) 439–459.

[44] I. Mandralis, P. Weber, G. Novati, P. Koumoutsakos, Learning swimming escape patterns for larval fish under energy constraints, Physical Review Fluids 6 (9) (2021) 093101.

[45] E. Marder, D. Bucher, Central pattern generators and the control of rhythmic movements, Current biology 11 (23) (2001) R986–R996.

[46] U. K. Muller, J. G. M. van den Boogaart, J. L. van Leeuwen, Flow patterns of larval fish: undulatory swimming in the intermediate flow regime, Journal of Experimental Biology 211 (2) (2008) 196–205, doi: 10.1242/jeb.005629.

[47] U. K. Muller, J. L. van Leeuwen, Swimming of larval zebrafish: ontogeny of body waves and implications for locomotory development, Journal of Experimental Biology 207 (5) (2004) 853–868, doi: 10.1242/jeb.00821.

[48] A. Munnier, B. Pinçon, Locomotion of articulated bodies in an ideal fluid: 2d model with buoyancy, circulation and collisions, Mathematical Models and Methods in Applied Sciences 20 (10) (2010) 1899–1940.

[49] F. Noca, On the evaluation of instantaneous fluid-dynamic forces on a bluff body, Galcit report .

[50] G. Novati, S. Verma, D. Alexeev, D. Rossinelli, W. M. Van Rees, P. Koumoutsakos, Synchronisation through learning for two self-propelled swimmers, Bioinspiration & biomimetics 12 (3) (2017) 036001.

[51] R. Ortega, A. Loria, P. J. Nicklasson, H. Sira-Ramirez, R. Ortega, A. Loría, P. J. Nicklasson, H. Sira-Ramírez, Euler-Lagrange systems, Springer, 1998.

[52] C. Oseen, Uber die wirbelbewegung in einer reibenden flussigkeit, Ark. Mat. Astro. Fys. 7.

[53] B. G. Oskouei, E. Kanso, Stability of passive locomotion in inviscid wakes, Physics of Fluids 25 (2) (2013) 021901.

[54] J. B. Pettigrew, Animal Locomotion: Or, Walking, Swimming, and Flying, with a Dissertation on Aëronautics, vol. 7, HS King & Company, 1873.

[55] M. Porez, F. Boyer, A. J. Ijspeert, Improved Lighthill fish swimming model for bio-inspired robots: Modeling, computational aspects and experimental comparisons, The International Journal of Robotics Research 33 (10) (2014) 1322–1341.

[56] C. Rackauckas, Q. Nie, Differentialequations.jl–a performant and feature-rich ecosystem for solving differential equations in julia, Journal of Open Research Software 5 (1) (2017) 15.

[57] J. Revels, M. Lubin, T. Papamarkou, Forward-Mode Automatic Differentiation in Julia, arXiv:1607.07892 [cs.MS] .

[58] L. Rosenhead, Proc. R. Soc. London Ser. A 127.

[59] L. Rosenhead, The formation of vortices from a surface of discontinuity, Proceedings of the Royal Society of London. Series A, Containing Papers of a Mathematical and Physical Character 134 (823) (1931) 170–192.

[60] J.-C. Samin, P. Fisette, Symbolic modeling of multibody systems, vol. 112, Springer Science & Business Media, 2003.

[61] J. Sherman, Adjustment of an inverse matrix corresponding to changes in the elements of a given column or a given row of the original matrix, Annals of mathematical statistics 20 (4) (1949) 621.

[62] M. W. Spong, S. Hutchinson, M. Vidyasagar, et al., Robot modeling and control, vol. 3, Wiley New York, 2006.

[63] R. S. Sutton, A. G. Barto, Reinforcement learning: An introduction, MIT press, 2018.

[64] A. A. Tchieu, A. Leonard, A discrete-vortex model for the arbitrary motion of a thin airfoil with fluidic control, Journal of fluids and structures 27 (5-6) (2011) 680–693.

[65] T. Theodorsen, General theory of aerodynamic instability and the mechanism of flutter, NASA reference publication .

[66] G. S. Triantafyllou, M. S. Triantafyllou, M. A. Grosenbaugh, Optimal thrust development in oscillating foils with application to fish propulsion, Journal of Fluids and Structures 7 (2) (1993) 205–224.

[67] M. S. Triantafyllou, G. S. Triantafyllou, An efficient swimming machine, Scientific american 272 (3) (1995) 64–70.

[68] J. Van Leeuwen, The action of muscles in swimming fish, Experimental Physiology: Translation and Integration 80 (2) (1995) 177–191.

[69] J. Van Leeuwen, M. Lankheet, H. Akster, J. Osse, Function of red axial muscles of carp (Cyprinus carpio): recruitment and normalized power output during swimming in different modes, Journal of Zoology 220 (1) (1990) 123–145.

[70] S. Verma, G. Novati, P. Koumoutsakos, Efficient collective swimming by harnessing vortices through deep reinforcement learning, Proceedings of the National Academy of Sciences 115 (23) (2018) 5849–5854.

[71] C. J. Voesenek, G. Li, F. T. Muijres, J. L. van Leeuwen, Experimental–numerical method for calculating bending moments in swimming fish shows that fish larvae control undulatory swimming with simple actuation, PLOS Biology 18 (7) (2020) 1–24, doi: 10.1371/journal.pbio.3000462.

[72] C. J. Voesenek, R. P. Pieters, J. L. van Leeuwen, Automated reconstruction of three-dimensional fish motion, forces, and torques, PloS one 11 (1) (2016) e0146682.

[73] H. Wagner, Über die Entstehung des dynamischen Auftriebes von Tragflügeln .

[74] C. Wang, J. D. Eldredge, Low-order phenomenological modeling of leading-edge vortex formation, Theoretical and Computational Fluid Dynamics 27 (5) (2013) 577–598.

[75] Z. J. Wang, J. M. Birch, M. H. Dickinson, Unsteady forces and flows in low Reynolds number hovering flight: two-dimensional computations vs robotic wing experiments, Journal of Experimental Biology 207 (3) (2004) 449–460.

[76] P. Weber, G. Arampatzis, G. Novati, S. Verma, C. Papadimitriou, P. Koumoutsakos, Optimal sensing for fish school identification, arXiv preprint arXiv:1910.09937 .

[77] G. Winckelmans, A. Leonard, Contributions to vortex particle methods for the computation of three-dimensional incompressible unsteady flows, Journal of Computational Physics 109 (2) (1993) 247–273.

[78] J.-Z. Wu, H.-Y. Ma, M.-D. Zhou, Vorticity and vortex dynamics, Springer Science & Business Media, 2007.

[79] X. Xia, K. Mohseni, Modeling of 2D unsteady motion of a flat plate using potential flow, in: 31st AIAA Applied Aerodynamics Conference, 2819, 2013.

[80] X. Xia, K. Mohseni, Unsteady aerodynamics and vortex-sheet formation of a two-dimensional airfoil, Journal of Fluid Mechanics 830 (2017) 439–478.

APPENDIX **A**

Mathematical tools

A.1 Useful integrals in 1D

Among the fundamental elements necessary to develop the framework described therein, a few unidimensional integrals are of key importance.

$$\begin{aligned}\int \frac{a\xi + b}{(x-\xi)^2 + y^2}\,\mathrm{d}\xi =& \frac{1}{y}(ax+b)\tan^{-1}\left(\frac{\xi - x}{y}\right) \\ &+ \frac{a}{2}a\log\left((x-\xi)^2 + y^2\right) + k \in \mathbb{R}\end{aligned} \tag{A.1}$$

$$\begin{aligned}\int \frac{a\xi^2 + b\xi + c}{(x-\xi)^2 + y^2}\,\mathrm{d}\xi =& \frac{1}{y}\left(a(x^2 - y^2) + bx + c\right)\tan^{-1}\left(\frac{\xi - x}{y}\right) \\ &+ \frac{1}{2}(2ax + b)\log\left((x-\xi)^2 + y^2\right) + a\xi + k \in \mathbb{R}\end{aligned} \tag{A.2}$$

A.2 Green's Identity

Consider a volume $\mathscr{V}_b$ bounded externally by a surface $\mathscr{S}_b$, as shown in Fig. A.1. We denote by $\mathscr{V}_f$ the remaining volume expanding to infinity. Then, if we define $\boldsymbol{n}$ as the unit normal on $\mathscr{S}_b$ pointing outside of $\mathscr{V}_b$, we can write the curl of Green's third identity

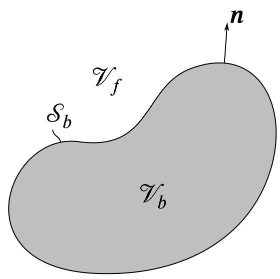

Figure A.1: An externally bounded volume $\mathscr{V}_b$ combined with an internally closed planar volume $\mathscr{V}_f$.

for a vector field $\boldsymbol{u}_b$ twice-differentiable in $\mathscr{V}_b$:

$$\begin{aligned}\overline{\boldsymbol{u}}_b(\boldsymbol{x}) = &\int_{\mathscr{V}_b} \left[\boldsymbol{K}(\boldsymbol{x}-\boldsymbol{y}) \times \left(\nabla \times \boldsymbol{u}_b(\boldsymbol{y})\right) + \boldsymbol{K}(\boldsymbol{x}-\boldsymbol{y})\left(\nabla \cdot \boldsymbol{u}_b(\boldsymbol{y})\right)\right] \mathrm{d}V(\boldsymbol{y}) \\ &- \fint_{\mathscr{S}_b} \left[\boldsymbol{K}(\boldsymbol{x}-\boldsymbol{y}) \times \left(\boldsymbol{n}(\boldsymbol{y}) \times \boldsymbol{u}_b(\boldsymbol{y})\right) - \boldsymbol{K}(\boldsymbol{x}-\boldsymbol{y})\left(\boldsymbol{n}(\boldsymbol{y}) \cdot \boldsymbol{u}_b(\boldsymbol{y})\right)\right] \mathrm{d}S(\boldsymbol{y}),\end{aligned} \tag{A.3}$$

where

$$\overline{\boldsymbol{u}}_b(\boldsymbol{x}) = \begin{cases} \boldsymbol{u}_b(\boldsymbol{x}), & \text{if } \boldsymbol{x} \in \mathscr{V}_b, \\ \frac{1}{2}\boldsymbol{u}_b(\boldsymbol{x}), & \text{if } \boldsymbol{x} \in \mathscr{S}_b, \\ \boldsymbol{0}, & \text{if } \boldsymbol{x} \in \mathscr{V}_f. \end{cases} \tag{A.4}$$

The dashed integral symbol stands for the principal value surface integral which is independent of the side from which we approach the surface. It represents the average of the limits of the surface integrals as $\boldsymbol{x}$ approaches $\mathscr{S}_b$ from either side.

We can expose an interesting result of Eq. (A.3) for a uniform vector field:

$$\frac{1}{2}\boldsymbol{u}_b = -\fint_{\mathscr{S}_b} \left[\boldsymbol{K}(\boldsymbol{x}-\boldsymbol{y}) \times \left(\boldsymbol{n}(\boldsymbol{y}) \times \boldsymbol{u}_b\right) - \boldsymbol{K}(\boldsymbol{x}-\boldsymbol{y})\left(\boldsymbol{n}(\boldsymbol{y}) \cdot \boldsymbol{u}_b\right)\right] \mathrm{d}S(\boldsymbol{y}), \tag{A.5}$$

when $\boldsymbol{x} \in \mathscr{S}_b$.

The fact that $\mathscr{V}_b$ is externally bounded is not critical, i.e. the same result holds for internally bounded volumes such as $\mathscr{V}_f$ too but there is one constraint: a boundary condition needs to be defined at infinity.

If we consider a field $\boldsymbol{u}$ in the external region $\mathscr{V}_f$ that vanishes at infinity, then we can superimpose the result of Eq. (A.3) applied both to $\boldsymbol{u}_b$ and $\boldsymbol{u}$, resulting in the following:

$$\begin{aligned}\overline{\boldsymbol{u}}(\boldsymbol{x}) = &\int_{\mathscr{V}_f} \left[\boldsymbol{K}\left(\boldsymbol{x}-\boldsymbol{y}\right)\times\left(\nabla\times\boldsymbol{u}\right)+\boldsymbol{K}\left(\boldsymbol{x}-\boldsymbol{y}\right)\left(\nabla\cdot\boldsymbol{u}\right)\right]\mathrm{d}V \\ &+\int_{\mathscr{V}_b}\left[\boldsymbol{K}\left(\boldsymbol{x}-\boldsymbol{y}\right)\times\left(\nabla\times\boldsymbol{u}_b\right)+\boldsymbol{K}\left(\boldsymbol{x}-\boldsymbol{y}\right)\left(\nabla\cdot\boldsymbol{u}_b\right)\right]\mathrm{d}V \\ &+\oint_{\mathscr{S}_b}\left[\boldsymbol{K}\left(\boldsymbol{x}-\boldsymbol{y}\right)\times\left(\boldsymbol{n}\times(\boldsymbol{u}-\boldsymbol{u}_b\right)-\boldsymbol{K}\left(\boldsymbol{x}-\boldsymbol{y}\right)\left(\boldsymbol{n}\cdot(\boldsymbol{u}-\boldsymbol{u}_b)\right)\right]\ \mathrm{d}S,\end{aligned} \tag{A.6}$$

where we dropped the dependency on $\boldsymbol{y}$ for legibility reasons,

$$\overline{\boldsymbol{u}}(\boldsymbol{x}) = \begin{cases}\boldsymbol{u}_b(\boldsymbol{x}), & \text{if } \boldsymbol{x}\in\mathscr{V}_b,\\ \frac{1}{2}\left(\boldsymbol{u}(\boldsymbol{x})+\boldsymbol{u}_b(\boldsymbol{x})\right), & \text{if } \boldsymbol{x}\in\mathscr{S}_b,\\ \boldsymbol{u}(\boldsymbol{x}), & \text{if } \boldsymbol{x}\in\mathscr{V}_f.\end{cases} \tag{A.7}$$

It is important to notice that because the normal vector points towards $\mathscr{V}_f$, instead of outside of it, there is a sign flip in the surface integral.

A.3 Integrals on vortex panels

This section focuses on analytic integration of key quantities enabling simulations to run. The reader can skip this part for it only provides tools for the developer willing to understand and/or expand the library.

Every integral in this work is computed analytically on each boundary element or panel on $\mathscr{S}_b$, see Fig. A.2. Let us begin with a few definitions; for some panel p undergoing a rigid motion, the following vectorial quantities are all expressed in a reference frame $\hat{\boldsymbol{e}}_\xi O\hat{\boldsymbol{e}}_\psi$ centered on the middle of the panel:

- b: half-length;
- $\boldsymbol{R}\in\mathfrak{so}(2)$: rotation matrix from $\hat{\boldsymbol{e}}_\xi O\hat{\boldsymbol{e}}_\psi$ to $\hat{\boldsymbol{e}}_x O\hat{\boldsymbol{e}}_y$;
- $\boldsymbol{T}\in\mathfrak{se}(2)$: transformation matrix from $\hat{\boldsymbol{e}}_\xi O\hat{\boldsymbol{e}}_\psi$ to $\hat{\boldsymbol{e}}_x O\hat{\boldsymbol{e}}_y$;
- $[\xi,\psi]^T = \boldsymbol{T}^{-1}\boldsymbol{x}$: system coordinates;
- $[x_r, y_r]^T = \boldsymbol{T}^{-1}\boldsymbol{x}_r$: center of rotation;
- $[x_0, y_0]^T = \boldsymbol{T}^{-1}\boldsymbol{x}_0$: location of the inertial frame of reference;

- Ω: angular velocity around the center of rotation;
- $[u, v]^T = \boldsymbol{R}^{-1}\dot{\boldsymbol{x}}_r$: velocity of the center of rotation;
- $[u_{cm}, v_{cm}]^T = \boldsymbol{R}^{-1}\dot{\boldsymbol{x}}_{cm}$: velocity of the body centroid;
- $[\frac{\tau_s}{2b}\xi, 0]^T$: stretching velocity.
- $\boldsymbol{\gamma}(\xi) = (\alpha\xi + \beta)\hat{\boldsymbol{e}}_z$: piecewise-linear vortex strength.

The surface velocity on panel p can then be written:

$$\begin{bmatrix} u_b \\ v_b \end{bmatrix} = \begin{bmatrix} \frac{\tau_s}{2b}\xi + u + \Omega y_r \\ \Omega\xi + v - \Omega x_r \end{bmatrix}, \tag{A.8}$$

and the normal vector $\boldsymbol{n}$ pointing outside of $\mathscr{V}_b$ becomes

$$\boldsymbol{R}^{-1}\boldsymbol{n} = -\hat{\boldsymbol{e}}_\psi. \tag{A.9}$$

Finally, two recurrent quantities can be written:

$$\boldsymbol{n} \cdot \boldsymbol{u} = \boldsymbol{n} \cdot \boldsymbol{u}_b = -v_b, \tag{A.10}$$

$$\boldsymbol{n} \times \boldsymbol{u}_b = u_b \hat{\boldsymbol{e}}_z. \tag{A.11}$$

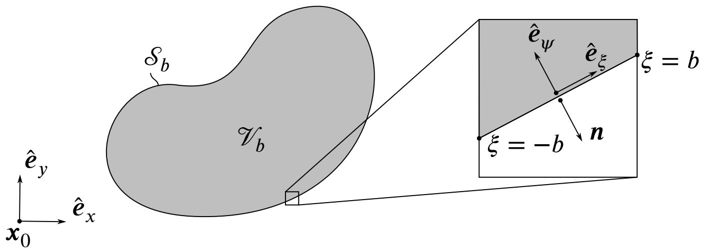

Figure A.2: An immersed body and a close up view of a boundary element on its surface. The coordinate vector $\hat{\boldsymbol{e}}_\psi$ points inside of the body and surface integration is performed in a counter-clockwise manner.

A.3.1 Airfoil geometry

Body volume

$$\begin{aligned} \mathscr{V}_b &= \oint_{\mathscr{V}_b} \mathrm{d}V = \frac{1}{\mathscr{N}_d}\oint_{\mathscr{V}_b} \nabla \cdot (\boldsymbol{x} - \boldsymbol{x}_0)\,\mathrm{d}V = \frac{1}{\mathscr{N}_d}\oint_{\mathscr{S}_b} \boldsymbol{n} \cdot (\boldsymbol{x} - \boldsymbol{x}_0)\,\mathrm{d}S \\ &= \frac{1}{2}\sum \int_{-b}^{b} y_0 \,\mathrm{d}\xi = \sum y_0 b \end{aligned} \tag{A.12}$$

Body Centroid

$$\begin{aligned} \boldsymbol{x}_{cm} - \boldsymbol{x}_0 =& \frac{1}{\mathscr{V}_b} \oint_{\mathscr{V}_b} (\boldsymbol{x} - \boldsymbol{x}_0)\, \mathrm{d}V = \frac{1}{2\mathscr{V}_b} \oint_{\mathscr{S}_b} |\boldsymbol{x} - \boldsymbol{x}_0|^2 \boldsymbol{n}\, \mathrm{d}S \\ =& -\frac{1}{\mathscr{V}_b} \sum b \left((x_0^2 + y_0^2) + \frac{1}{3} b^2 \right) \boldsymbol{T} \hat{\boldsymbol{e}}_\psi \end{aligned} \tag{A.13}$$

Body Inertia

$$\begin{aligned} I_3 =& \oint_{\mathscr{V}_b} |\boldsymbol{x} - \boldsymbol{x}_0|^2\, \mathrm{d}V = \frac{1}{4} \oint_{\mathscr{S}_b} |\boldsymbol{x} - \boldsymbol{x}_0|^2 (\boldsymbol{x} - \boldsymbol{x}_0) \cdot \boldsymbol{n}\, \mathrm{d}S \\ =& \frac{1}{2} \sum y_0 b \left((x_0^2 + y_0^2) + \frac{1}{3} b^2 \right) \end{aligned} \tag{A.14}$$

A.3.2 Elementary quantities from potential flow theory

Velocity potential on the body

$$\begin{aligned} \varphi(\boldsymbol{x}) - \varphi(\boldsymbol{x}_0) &= \int_{\boldsymbol{x}_0}^{\boldsymbol{x}} \boldsymbol{u} \cdot\, \mathrm{d}\boldsymbol{\tau} \\ &= \sum_{p(\boldsymbol{x}_1)}^{p(\boldsymbol{x})} \int_{-b}^{b} \left(\left(\alpha + \frac{\tau_s}{2b} \right) \xi + \beta + u + \Omega y_r \right) \mathrm{d}\xi \\ &= \sum_{p(\boldsymbol{x}_1)}^{p(\boldsymbol{x})} 2b(\beta + u + \Omega y_r) \end{aligned} \tag{A.15}$$

Stream function

$$\psi(\boldsymbol{x}) \hat{\boldsymbol{e}}_z = -\frac{1}{2\pi} \oint \left[\log |\boldsymbol{x} - \boldsymbol{y}| \left(\boldsymbol{\gamma} + \boldsymbol{n} \times \boldsymbol{u}_b \right) - \tan^{-1} \left(\frac{x_x - y_x}{x_y - y_y} \right) (\boldsymbol{n} \cdot \boldsymbol{u}_b) \right] \mathrm{d}S(\boldsymbol{y}) \tag{A.16}$$

Motion induced attached velocity

$$\boldsymbol{S}(\boldsymbol{x}) = -\!\!\!\!\!\!\int_{\mathscr{S}_b} \left[\boldsymbol{K}\,(\boldsymbol{x} - \boldsymbol{y}) \times \left(\boldsymbol{n} \times \boldsymbol{u}_b \right) - \boldsymbol{K}\,(\boldsymbol{x} - \boldsymbol{y}) \left(\boldsymbol{n} \cdot \boldsymbol{u}_b \right) \right] \mathrm{d}S(\boldsymbol{y}) = \sum RAB \tag{A.17}$$

$$A = \begin{bmatrix} \tan^{-1}\left(\frac{b-x_x}{x_y}\right) + \tan^{-1}\left(\frac{b+x_x}{x_y}\right) & -\frac{1}{2}\log\left(\frac{(b-x_x)^2+x_y^2}{(b+x_x)^2+x_y^2}\right) & -\alpha_2 \\ \frac{1}{2}\log\left(\frac{(b-x_x)^2+x_y^2}{(b+x_x)^2+x_y^2}\right) & \tan^{-1}\left(\frac{b-x_x}{x_y}\right) + \tan^{-1}\left(\frac{b+x_x}{x_y}\right) & \alpha_1 \end{bmatrix} \tag{A.18}$$

$$B = \begin{bmatrix} \beta_1 + \alpha_1 x_x + \alpha_2 x_y \\ \beta_2 + \alpha_2 x_x - \alpha_1 x_y \\ 2b \end{bmatrix} \tag{A.19}$$

$$\alpha_1 = \frac{\tau_s}{2b}, \tag{A.20}$$

$$\beta_1 = u + \Omega y_r, \tag{A.21}$$

$$\alpha_2 = \Omega, \tag{A.22}$$

$$\beta_2 = v - \Omega x_r. \tag{A.23}$$

Vortex sheet induced attached velocity

$$\boldsymbol{Q}[\boldsymbol{\gamma}](\boldsymbol{x}) = \fint_{\mathcal{S}_b} \boldsymbol{K}\,(\boldsymbol{x}-\boldsymbol{y}) \times \boldsymbol{\gamma}(\boldsymbol{y})\mathrm{d}S(\boldsymbol{y}) = \frac{1}{2}\sum \boldsymbol{R}AB \begin{bmatrix} \gamma(-b) \\ \gamma(b) \end{bmatrix} \tag{A.24}$$

$$A = \begin{bmatrix} \tan^{-1}\left(\frac{b-x_x}{x_y}\right) + \tan^{-1}\left(\frac{b+x_x}{x_y}\right) & -\frac{1}{2}\log\left(\frac{(b-x_x)^2+x_y^2}{(b+x_x)^2+x_y^2}\right) & 0 \\ \frac{1}{2}\log\left(\frac{(b-x_x)^2+x_y^2}{(b+x_x)^2+x_y^2}\right) & \tan^{-1}\left(\frac{b-x_x}{x_y}\right) + \tan^{-1}\left(\frac{b+x_x}{x_y}\right) & 2 \end{bmatrix} \tag{A.25}$$

$$B = \begin{bmatrix} \frac{x_x}{b} - 1 & -\left(\frac{x_x}{b} + 1\right) \\ -\frac{x_y}{b} & \frac{x_y}{b} \\ 1 & -1 \end{bmatrix} \tag{A.26}$$

A.3.3 Force and momentum

Momentum

$$\boldsymbol{P} = \oint_{\mathcal{S}_b} (\boldsymbol{x} - \boldsymbol{x}_0) \times (\boldsymbol{n} \times \boldsymbol{u})\, \mathrm{d}S = \oint_{\mathcal{S}_b} (\boldsymbol{x} - \boldsymbol{x}_0) \times (\boldsymbol{\gamma} + \boldsymbol{n} \times \boldsymbol{u}_b)\, \mathrm{d}S = \sum \boldsymbol{R}\boldsymbol{p} \tag{A.27}$$

$$\begin{aligned} p_\xi &= \int_{-b}^{b} -y_0 \left(\left(\alpha + \frac{\tau_s}{2b} \right) \xi + \beta + u + \Omega y_r \right) \, \mathrm{d}\xi \\ &= -2y_0 b(\beta + u + \Omega y_r) \end{aligned} \tag{A.28}$$

$$\begin{aligned} p_\psi &= \int_{-b}^{b} (x_0 - \xi) \left(\left(\alpha + \frac{\tau_s}{2b} \right) \xi + \beta + u + \Omega y_r \right) \, \mathrm{d}\xi \\ &= \left(2x_0 b(\beta + u + \Omega y_r) - \frac{1}{3} b^2 (2b\alpha + \tau_s) \right) \end{aligned} \tag{A.29}$$

Angular momentum

$$\begin{aligned} \boldsymbol{\Pi}_0 &= \frac{1}{2} \oint_{\mathcal{S}_b} (\boldsymbol{x} - \boldsymbol{x}_0) \times [(\boldsymbol{x} - \boldsymbol{x}_0) \times (\boldsymbol{n} \times \boldsymbol{u})] \, \mathrm{d}S \\ &= -\frac{1}{2} \sum \int_{-b}^{b} (y_0^2 + (x_0 - \xi)^2) \left(\left(\alpha + \frac{\tau_s}{2b} \right) \xi + \beta + u + \Omega y_r \right) \, \mathrm{d}\xi \\ &= \sum \left(\frac{1}{3} x_0 b^2 \left(2b\alpha + \tau_s \right) - b(\beta + u + \Omega y_r) \left(\frac{1}{3} b^2 + x_0^2 + y_0^2 \right) \right) \end{aligned} \tag{A.30}$$

Vorticity induced force

$$\boldsymbol{F}_\omega = \oint_{\mathcal{S}_b} \left(\frac{1}{2} \boldsymbol{u} \cdot \boldsymbol{u}\boldsymbol{n} - \boldsymbol{u}\boldsymbol{u} \cdot \boldsymbol{n} \right) \, \mathrm{d}S = \sum \boldsymbol{R}\boldsymbol{f}_\omega \tag{A.31}$$

$$\begin{aligned} f_{\omega,\xi} &= \int_{-b}^{b} \Big((v - \Omega x_r) + \Omega \xi \Big) \left(\left(\alpha + \frac{\tau_s}{2b} \right) \xi + (\beta + u + \Omega y_r) \right) \, \mathrm{d}\xi \\ &= \left(\frac{b^2}{3} \Omega (2\alpha b + \tau_s) + 2b(v - \Omega x_r)(\beta + u + \Omega y_r) \right) \end{aligned} \tag{A.32}$$

$$\begin{aligned} f_{\omega,\psi} &= \frac{1}{2} \int_{-b}^{b} \left(\Big((v - \Omega x_r) + \Omega \xi \Big)^2 - \Big(\alpha \xi + (\beta + u + \Omega y_r) \Big)^2 \right) \, \mathrm{d}\xi \\ &= \left(\frac{b^3}{3} \left(\Omega^2 - \left(\alpha + \frac{\tau_s}{2b} \right)^2 \right) + b \Big((v - \Omega x_r)^2 - (\beta + u + \Omega y_r)^2 \Big) \right) \end{aligned} \tag{A.33}$$

Vorticity induced moment

$$
\begin{aligned}
\boldsymbol{m}_{\omega,0} &= \oint_{\mathcal{S}_b} (\boldsymbol{x}-\boldsymbol{x}_0)\times\left(\frac{1}{2}\boldsymbol{u}\cdot\boldsymbol{u}\boldsymbol{n}-\boldsymbol{u}\boldsymbol{u}\cdot\boldsymbol{n}\right)\,\mathrm{d}S \\
&= \sum\left(y_0 f_{\omega,\xi}-x_0 f_{\omega,\psi}+\Big((v-\Omega x_r)\Omega-(\beta+u+\Omega y_r)\Big(\alpha+\frac{\tau_s}{2b}\Big)\Big)\int_{-b}^{b}\xi^2\,\mathrm{d}\xi\right) \\
&= \sum\left(y_0 f_{\omega,\xi}-x_0 f_{\omega,\psi}+\frac{2}{3}b^3\left((v-\Omega x_r)\Omega-(\beta+u+\Omega y_r)\Big(\alpha+\frac{\tau_s}{2b}\Big)\right)\right)
\end{aligned}
\tag{A.34}
$$

Correction due to point of application of moment in motion

$$
\begin{aligned}
\boldsymbol{m}_{\omega,0} &= \dot{\boldsymbol{x}}_{cm}\times\oint_{\mathcal{S}_b}\boldsymbol{n}\cdot\boldsymbol{u}_b(\boldsymbol{x}-\boldsymbol{x}_0)\,\mathrm{d}S \\
&= \sum\int_{-b}^{b}\Big((v-\Omega x_r)+\Omega\xi\Big)\big(u_{cm}y_0+v_{cm}(\xi-x_0)\big)\,\mathrm{d}\xi \\
&= -\sum 2b\left(\frac{1}{3}v_{cm}\Omega b^2+(v-\Omega x_r)(v_{cm}x_0-u_{cm}y_0)\right)
\end{aligned}
\tag{A.35}
$$

APPENDIX B

Unsteady Kutta Condition

We now expose the Unsteady Kutta Condition derived by Prof. Winckelmans in a private communication. This initiative originates from the lack of clarity in development and presentation of the results proposed by Xia and Mohseni [80].

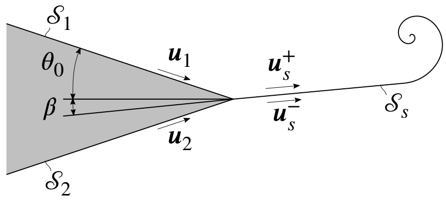

Figure B.1: Close up view at the trailing edge.

Without loss of generality, the trailing edge condition is derived in a frame of reference rigidly attached to the body (i.e. $\boldsymbol{u}_b = 0$). In such a configuration – shown in Fig. B.1 – the bisector of the trailing edge angle is aligned with $\hat{\boldsymbol{e}}_x$ and creates an angle $\pm\theta_0$ with the trailing edge panels $\mathcal{S}_1$ and $\mathcal{S}_2$. We define the angle β as the orientation of the free vortex sheet $\mathcal{S}_s$ just behind the trailing edge with respect to $\hat{\boldsymbol{e}}_x$. Finally, the vortex strengths on the body panels and on the free vortex sheet are given by

$$\begin{cases} \gamma_1 = u_1 - u_b = u_1, \\ \gamma_2 = -(u_2 - u_b) = -u_2, \\ \gamma_s = u_s^+ - u_s^-. \end{cases} \tag{B.1}$$

We now have to impose constraints to determine both the direction and the strength of the shed vortex sheet.

The continuity of the velocity in the direction parallel to the very near wake results in the following constraints:

$$\begin{cases} u_s^+ = u_1 \cos(\theta_0 + \beta), \\ u_s^- = u_2 \cos(\theta_0 - \beta), \end{cases} \tag{B.2}$$

Hence, using Eq. (B.1), we find an expression for the free vortex strength

$$\gamma_s = \gamma_1 \cos(\theta_0 + \beta) + \gamma_2 \cos(\theta_0 - \beta). \tag{B.3}$$

We then carry out a vorticity flux budget between regions downstream and upstream the trailing edge. We first define the vorticity flux operator

$$\aleph(x) = -\int_{-\delta}^{\delta} \omega u(x,y)\,\mathrm{d}y = \int_{-\delta}^{\delta} \frac{\partial}{\partial y}\left(\frac{u^2(x,y)}{2}\right)\,\mathrm{d}y = \frac{1}{2}(u^2(x,\delta) - u^2(x,-\delta)) \tag{B.4}$$

and calculate its value on each vortex sheet at the vicinity of the trailing edge:

$$\aleph(x) = \begin{cases} \frac{u_1^2}{2}, & \text{if } x \in \mathcal{S}_1, \\ -\frac{u_2^2}{2}, & \text{if } x \in \mathcal{S}_2, \\ \frac{1}{2}(u_s^+ + u_s^-)(u_s^+ - u_s^-), & \text{if } x \in \mathcal{S}_s. \end{cases} \tag{B.5}$$

The continuity of vorticity flux can therefore be expressed as

$$\frac{1}{2}(u_1 + u_2)(u_1 - u_2) = \frac{1}{2}(u_s^+ + u_s^-)(u_s^+ - u_s^-), \tag{B.6}$$

where the right hand side happens to be the product of the strength of the free vortex sheet and its average velocity. Equation (B.6) can be transformed with Eq. (B.2) into

$$u_1^2\big(1 - \cos^2(\theta_0 + \beta)\big) = u_2^2\big(1 - \cos^2(\theta_0 - \beta)\big). \tag{B.7}$$

This expression can be further simplified with the sine addition formula and Eq. (B.1) to give a final expression for β:

$$\beta = \tan^{-1}\left(\frac{\gamma_2 + \gamma_1}{\gamma_2 - \gamma_1}\tan(\theta_0)\right). \tag{B.8}$$

We can now clearly understand what happens at the trailing edge in three particular cases:

- $\gamma_1 = 0 \Rightarrow \beta = \theta_0$ and $\mathcal{S}_s$ aligned with $\mathcal{S}_2$;
- $\gamma_2 = 0 \Rightarrow \beta = -\theta_0$ and $\mathcal{S}_s$ aligned with $\mathcal{S}_1$;
- $\gamma_1 = -\gamma_2 \Rightarrow \beta = 0$, we retrieve the steady Kutta condition.

APPENDIX C

Derivation of the aerodynamic loads through a control-volume approach

This section is self-contained and exposes a mathematical adventure to compute instantaneous hydrodynamic force and moment on an planar body immersed in a inviscid flow using a control volume approach, i.e. with surface integrals of the velocity field and its derivatives only. This allows for a compact representation regardless of the ambient vorticity in the possibly infinite surrounding volume of fluid. It is inspired from and extends the work of [49] in which the analysis includes viscous effects but is limited to the hydrodynamic force without any discussion about the hydrodynamic moment.

C.1 Conservation equations

Without loss of generality, all forthcoming equations are written for a flow of unit density ($\rho = 1$). In addition, we only consider buoyant bodies, i.e. the fluid and solid are equally dense. Since density is uniform everywhere, the flow is incompressible and has therefore to obey the so-called continuity equation

$$\nabla \cdot \boldsymbol{u} = 0. \tag{C.1}$$

The second law the flow must obey regards the conservation of momentum everywhere in the domain. This is enforced by Euler's equation. When no volumic force interacts with the flow, using Eq. (C.46) and accounting for incompressibility, it becomes

$$\begin{aligned}\frac{\partial \boldsymbol{u}}{\partial t} &= -\boldsymbol{u}\cdot\nabla\boldsymbol{u} - \nabla p \\ &= -\nabla(p + \frac{1}{2}u^2) + \boldsymbol{u}\times\boldsymbol{\omega},\end{aligned} \tag{C.2}$$

where $\boldsymbol{\omega} = \nabla\times\boldsymbol{u}$ is the vorticity field. This formulation allows to clearly distinguish the rotational and irrotational parts in this equation.

C.2 Force computation

The force on a body can be obtained via the integral of the surface traction, namely

$$\boldsymbol{f} = \oint_{\mathcal{S}_b} -p\boldsymbol{n}\,\mathrm{d}S, \tag{C.3}$$

where the field p represents the pressure and the unit vector $\boldsymbol{n}$ normal to the body surface $\mathcal{S}_b$ points towards the fluid.

For reasons that will become clearer later, we can add and subtract the dynamic pressure without affecting the equality:

$$\boldsymbol{f} = \oint_{\mathcal{S}_b} -\left(p + \frac{1}{2}u^2\right)\boldsymbol{n}\,\mathrm{d}S + \oint_{\mathcal{S}_b}\frac{1}{2}u^2\boldsymbol{n}\,\mathrm{d}S. \tag{C.4}$$

Using Green's Theorem, the first integral turns into

$$\begin{aligned}\boldsymbol{f} &= \int_{\mathcal{V}_b} -\nabla\left(p + \frac{1}{2}u^2\right)\,\mathrm{d}V + \oint_{\mathcal{S}_b}\frac{1}{2}u^2\boldsymbol{n}\,\mathrm{d}S \\ &= \frac{1}{\mathcal{N}_d - 1}\oint_{\mathcal{S}_b}\boldsymbol{x}\times\left[\boldsymbol{n}\times\nabla\left(p + \frac{1}{2}u^2\right)\right]\,\mathrm{d}S + \oint_{\mathcal{S}_b}\frac{1}{2}u^2\boldsymbol{n}\,\mathrm{d}S,\end{aligned} \tag{C.5}$$

with the domain dimension $\mathcal{N}_d = \nabla\cdot\boldsymbol{x}$. The second line stems from Eq. (C.56) and $\nabla\times\nabla\varphi = 0$. Now, we use Euler equation in the first integral to obtain an expression for the force which only depends on the velocity field and its derivative:

$$\boldsymbol{f} = -\frac{1}{\mathcal{N}_d - 1}\oint_{\mathcal{S}_b}\boldsymbol{x}\times\left[\boldsymbol{n}\times\left(\frac{\partial\boldsymbol{u}}{\partial t} - \boldsymbol{u}\times\boldsymbol{\omega}\right)\right]\,\mathrm{d}S + \oint_{\mathcal{S}_b}\frac{1}{2}u^2\boldsymbol{n}\,\mathrm{d}S. \tag{C.6}$$

Computing the first integral is not straightforward, but it can be simplified further. Its second term can be re-written

$$\boldsymbol{x}\times[\boldsymbol{n}\times(\boldsymbol{u}\times\boldsymbol{\omega})] = \boldsymbol{n}\cdot[\,\boldsymbol{\omega}(\boldsymbol{x}\times\boldsymbol{u}) - \boldsymbol{u}(\boldsymbol{x}\times\boldsymbol{\omega})]\,, \tag{C.7}$$

such that the force on the body becomes

$$\begin{aligned} \boldsymbol{f} = &-\frac{1}{\mathcal{N}_d - 1}\oint_{\mathcal{S}_b} \boldsymbol{x}\times(\boldsymbol{n}\times\frac{\partial \boldsymbol{u}}{\partial t})\,\mathrm{d}S + \oint_{\mathcal{S}_b}\frac{1}{2}u^2\boldsymbol{n}\,\mathrm{d}S \\ &-\frac{1}{\mathcal{N}_d - 1}\oint_{\mathcal{S}_b}\left[\boldsymbol{n}\cdot\boldsymbol{u}(\boldsymbol{x}\times\boldsymbol{\omega}) - \boldsymbol{n}\cdot\boldsymbol{\omega}(\boldsymbol{x}\times\boldsymbol{u})\right]\,\mathrm{d}S. \end{aligned} \tag{C.8}$$

The time derivative of the first integral is still impractical. To get rid of it, we can combine Eq. (C.53) and Eq. (C.45) to show that

$$\begin{aligned} \oint_{\mathcal{S}_b}\boldsymbol{x}\times(\boldsymbol{n}\times\frac{\partial \boldsymbol{u}}{\partial t})\,\mathrm{d}S &= \frac{\mathrm{d}}{\mathrm{d}t}\oint_{\mathcal{S}_b}\boldsymbol{x}\times(\boldsymbol{n}\times\boldsymbol{u})\,\mathrm{d}S - \oint_{\mathcal{S}_b}\boldsymbol{n}\cdot\boldsymbol{u}_b\nabla\cdot\left[(\boldsymbol{x}\cdot\boldsymbol{u})\boldsymbol{I} - \boldsymbol{x}\boldsymbol{u}\right]\,\mathrm{d}S \\ &= \frac{\mathrm{d}}{\mathrm{d}t}\oint_{\mathcal{S}_b}\boldsymbol{x}\times(\boldsymbol{n}\times\boldsymbol{u})\,\mathrm{d}S - \oint_{\mathcal{S}_b}\boldsymbol{n}\cdot\boldsymbol{u}_b\left[\boldsymbol{x}\times\boldsymbol{\omega} - (\mathcal{N}_d - 1)\boldsymbol{u}\right]\,\mathrm{d}S, \end{aligned} \tag{C.9}$$

where the second line results from Eqs. (C.46) and (C.47).

We can plug this result into Eq. (C.8) to obtain a more gentle expression for the hydrodynamic force on the body

$$\begin{aligned} \boldsymbol{f} = &\oint_{\mathcal{S}_b}\left(\frac{1}{2}u^2\boldsymbol{n} - \boldsymbol{u}\boldsymbol{u}_b\cdot\boldsymbol{n}\right)\,\mathrm{d}S - \frac{1}{(\mathcal{N}_d - 1)}\frac{\mathrm{d}}{\mathrm{d}t}\oint_{\mathcal{S}_b}\boldsymbol{x}\times(\boldsymbol{n}\times\boldsymbol{u})\,\mathrm{d}S \\ &+\frac{1}{(\mathcal{N}_d - 1)}\oint_{\mathcal{S}_b}\boldsymbol{n}\cdot\left[\boldsymbol{\omega}(\boldsymbol{x}\times\boldsymbol{u}) - (\boldsymbol{u}-\boldsymbol{u}_b)(\boldsymbol{x}\times\boldsymbol{\omega})\right]\,\mathrm{d}S. \end{aligned} \tag{C.10}$$

In bidimensional domains, the vorticity field is always perpendicular to the planar domain so that the first term of the last integral vanishes. This leads us to the final result:

$$\boldsymbol{f} = \oint_{\mathcal{S}_b}\left(\frac{1}{2}u^2\boldsymbol{n} - \boldsymbol{u}\boldsymbol{u}_b\cdot\boldsymbol{n}\right)\,\mathrm{d}S - \frac{\mathrm{d}}{\mathrm{d}t}\oint_{\mathcal{S}_b}\boldsymbol{x}\times(\boldsymbol{n}\times\boldsymbol{u})\,\mathrm{d}S - \oint_{\mathcal{S}_b}\boldsymbol{n}\cdot(\boldsymbol{u}-\boldsymbol{u}_b)(\boldsymbol{x}\times\boldsymbol{\omega})\,\mathrm{d}S. \tag{C.11}$$

This formula remains true if written in a frame of reference that follows the center of mass of the body.

$$\begin{aligned} \boldsymbol{f} = &\oint_{\mathcal{S}_b}\left(\frac{1}{2}u'^2\boldsymbol{n} - \boldsymbol{u}'\boldsymbol{u}'_b\cdot\boldsymbol{n}\right)\,\mathrm{d}S - \frac{\mathrm{d}}{\mathrm{d}t}\oint_{\mathcal{S}_b}\boldsymbol{x}'\times(\boldsymbol{n}\times\boldsymbol{u})\,\mathrm{d}S \\ &-\oint_{\mathcal{S}_b}\boldsymbol{n}\cdot(\boldsymbol{u}-\boldsymbol{u}_b)(\boldsymbol{x}'\times\boldsymbol{\omega})\,\mathrm{d}S, \end{aligned} \tag{C.12}$$

where $\boldsymbol{x}' = \boldsymbol{x} - \boldsymbol{x}_{cm}$ and $\boldsymbol{u}' = \boldsymbol{u} - \dot{\boldsymbol{x}}_{cm}$. This expression avoids amplification of floating arithmetic errors due to the growth of $\boldsymbol{x}$ as the body gets further and further from the origin of the inertial frame.

Proof. To prove this, we take the difference between Eqs. (C.12) and (C.11) and obtain

$$\begin{aligned}\mathbf{0} = &\oint_{\mathcal{S}_b} \left(\frac{1}{2}u'^2\boldsymbol{n} - \boldsymbol{u}'\boldsymbol{u}'_b \cdot \boldsymbol{n}\right) \mathrm{d}S - \oint_{\mathcal{S}_b} \left(\frac{1}{2}u^2\boldsymbol{n} - \boldsymbol{u}\boldsymbol{u}_b \cdot \boldsymbol{n}\right) \mathrm{d}S \\ &+ \frac{\mathrm{d}}{\mathrm{d}t}\oint_{\mathcal{S}_b} \boldsymbol{x}_{cm} \times (\boldsymbol{n} \times \boldsymbol{u})\,\mathrm{d}S + \oint_{\mathcal{S}_b} \boldsymbol{n} \cdot (\boldsymbol{u} - \boldsymbol{u}_b)(\boldsymbol{x}_{cm} \times \boldsymbol{\omega})\,\mathrm{d}S.\end{aligned} \tag{C.13}$$

Now, by virtue of incompressibility and Green's Divergence Theorem, we can rewrite the first integral in Eq. (C.13) as

$$\oint_{\mathcal{S}_b} \left(\frac{1}{2}u'^2\boldsymbol{n} - \boldsymbol{u}'\boldsymbol{u}'_b \cdot \boldsymbol{n}\right) \mathrm{d}S = \int_{\mathcal{V}_b} \boldsymbol{u}' \times \boldsymbol{\omega}\,\mathrm{d}V + \oint_{\mathcal{S}_b} \boldsymbol{n} \cdot (\boldsymbol{u} - \boldsymbol{u}_b)\boldsymbol{u}'\,\mathrm{d}S, \tag{C.14}$$

and the second one as

$$\oint_{\mathcal{S}_b} \left(\frac{1}{2}u^2\boldsymbol{n} - \boldsymbol{u}\boldsymbol{u}_b \cdot \boldsymbol{n}\right) \mathrm{d}S = \int_{\mathcal{V}_b} \boldsymbol{u} \times \boldsymbol{\omega}\,\mathrm{d}V + \oint_{\mathcal{S}_b} \boldsymbol{n} \cdot (\boldsymbol{u} - \boldsymbol{u}_b)\boldsymbol{u}\,\mathrm{d}S, \tag{C.15}$$

such that Eq. (C.13) becomes

$$\begin{aligned}\mathbf{0} = &-\int_{\mathcal{V}_b} \dot{\boldsymbol{x}}_{cm} \times \boldsymbol{\omega}\,\mathrm{d}V - \oint_{\mathcal{S}_b} \boldsymbol{n} \cdot (\boldsymbol{u} - \boldsymbol{u}_b)\dot{\boldsymbol{x}}_{cm}\,\mathrm{d}S \\ &+ \frac{\mathrm{d}}{\mathrm{d}t}\oint_{\mathcal{S}_b} \boldsymbol{x}_{cm} \times (\boldsymbol{n} \times \boldsymbol{u})\,\mathrm{d}S + \oint_{\mathcal{S}_b} \boldsymbol{n} \cdot (\boldsymbol{u} - \boldsymbol{u}_b)(\boldsymbol{x}_{cm} \times \boldsymbol{\omega})\,\mathrm{d}S.\end{aligned} \tag{C.16}$$

The displacement of the center of mass being independent of the integral path and the incompressibility of the body and fluid make the second integral vanish such that

$$\mathbf{0} = -\int_{\mathcal{V}_b} \dot{\boldsymbol{x}}_{cm} \times \boldsymbol{\omega}\,\mathrm{d}V + \frac{\mathrm{d}}{\mathrm{d}t}\oint_{\mathcal{S}_b} \boldsymbol{x}_{cm} \times (\boldsymbol{n} \times \boldsymbol{u})\,\mathrm{d}S + \oint_{\mathcal{S}_b} \boldsymbol{n} \cdot (\boldsymbol{u} - \boldsymbol{u}_b)(\boldsymbol{x}_{cm} \times \boldsymbol{\omega})\,\mathrm{d}S. \tag{C.17}$$

By noting that

$$-\int_{\mathcal{V}_b} \dot{\boldsymbol{x}}_{cm} \times \boldsymbol{\omega}\,\mathrm{d}V = -\int_{\mathcal{V}_b} \frac{\partial}{\partial t}\left(\boldsymbol{x}_{cm} \times \boldsymbol{\omega}\right)\,\mathrm{d}V + \int_{\mathcal{V}_b} \boldsymbol{x}_{cm} \times \frac{\partial \boldsymbol{\omega}}{\partial t}\,\mathrm{d}V, \tag{C.18}$$

and, using Stokes' Theorem, that

$$\frac{\mathrm{d}}{\mathrm{d}t}\oint_{\mathcal{S}_b} \boldsymbol{x}_{cm} \times (\boldsymbol{n} \times \boldsymbol{u})\,\mathrm{d}S = \frac{\mathrm{d}}{\mathrm{d}t}\int_{\mathcal{V}_b} \boldsymbol{x}_{cm} \times \boldsymbol{\omega}\,\mathrm{d}V, \tag{C.19}$$

Eq. (C.17) simplifies into

$$\begin{aligned}\mathbf{0} &= \int_{\mathscr{V}_b} \boldsymbol{x}_{cm} \times \frac{\partial \boldsymbol{\omega}}{\partial t}\, \mathrm{d}V + \oint_{\mathscr{S}_b} \boldsymbol{n} \cdot \boldsymbol{u}(\boldsymbol{x}_{cm} \times \boldsymbol{\omega})\, \mathrm{d}S \\ &= \boldsymbol{x}_{cm} \times \frac{\mathrm{d}}{\mathrm{d}t} \int_{\mathscr{V}_{bm}} \boldsymbol{\omega}\, \mathrm{d}V,\end{aligned} \tag{C.20}$$

which is verified by taking the curl of Euler equation in two dimensions. □

C.3 Moment computation

Deriving an expression for the aerodynamic moment around the body is very similar to what has been carried out in the previous section. Therefore, fewer comments are addressed which should not hinder the comprehension of a motivated reader. The angular moment on a body can be obtained from the integral of the first moment of the surface traction, namely

$$\boldsymbol{m}_0 = \oint_{\mathscr{S}_b} -\boldsymbol{x} \times p\boldsymbol{n}\, \mathrm{d}S. \tag{C.21}$$

Once again, we can add and subtract the first moment of the dynamic pressure without interfering with the equation, yielding

$$\boldsymbol{m}_0 = \oint_{\mathscr{S}_b} -\boldsymbol{x} \times \left(p + \frac{1}{2}u^2\right) \boldsymbol{n}\, \mathrm{d}S + \oint_{\mathscr{S}_b} \boldsymbol{x} \times \frac{1}{2}u^2 \boldsymbol{n}\, \mathrm{d}S. \tag{C.22}$$

Using Green's Theorem, we get

$$\begin{aligned}\boldsymbol{m}_0 &= \int_{\mathscr{V}_b} \nabla \times \left[\boldsymbol{x} \times \left(p + \frac{1}{2}u^2\right)\right] \mathrm{d}V + \oint_{\mathscr{S}_b} \boldsymbol{x} \times \frac{1}{2}u^2 \boldsymbol{n}\, \mathrm{d}S \\ &= \int_{\mathscr{V}_b} -\boldsymbol{x} \times \nabla \left(p + \frac{1}{2}u^2\right) \mathrm{d}V + \oint_{\mathscr{S}_b} \boldsymbol{x} \times \frac{1}{2}u^2 \boldsymbol{n}\, \mathrm{d}S,\end{aligned} \tag{C.23}$$

where we used Eq. (C.49) to find the second equality. Then, using Eq. (C.59), we get

$$\boldsymbol{m}_0 = \frac{1}{\mathscr{N}_d} \int_{\mathscr{S}_b} \boldsymbol{x} \times \left(\boldsymbol{x} \times \left[\boldsymbol{n} \times \nabla \left(p + \frac{1}{2}u^2\right)\right]\right) \mathrm{d}S + \oint_{\mathscr{S}_b} \boldsymbol{x} \times \frac{1}{2}u^2 \boldsymbol{n}\, \mathrm{d}S. \tag{C.24}$$

The next step is to use Euler's equation in the first integral to obtain

$$\boldsymbol{m}_0 = -\frac{1}{\mathscr{N}_d} \int_{\mathscr{S}_b} \boldsymbol{x} \times \left(\boldsymbol{x} \times \left[\boldsymbol{n} \times \left(\frac{\partial \boldsymbol{u}}{\partial t} - \boldsymbol{u} \times \boldsymbol{\omega}\right)\right]\right) \mathrm{d}S + \oint_{\mathscr{S}_b} \boldsymbol{x} \times \frac{1}{2}u^2 \boldsymbol{n}\, \mathrm{d}S, \tag{C.25}$$

from which we can use Eq. (C.45) to rewrite the second term of the first integral as

$$\boldsymbol{x} \times [\boldsymbol{x} \times (\boldsymbol{u} \times \boldsymbol{\omega})] = \boldsymbol{n} \cdot \boldsymbol{\omega}[\boldsymbol{x} \times (\boldsymbol{x} \times \boldsymbol{u})] - \boldsymbol{n} \cdot \boldsymbol{u}[\boldsymbol{x} \times (\boldsymbol{x} \times \boldsymbol{\omega})]. \tag{C.26}$$

Hence, the moment can be formulated as

$$\begin{aligned} \boldsymbol{m}_0 = &- \frac{1}{\mathcal{N}_d} \oint_{\mathcal{S}_b} \boldsymbol{x} \times \left[\boldsymbol{x} \times \left(\boldsymbol{n} \times \frac{\partial \boldsymbol{u}}{\partial t}\right)\right] \, \mathrm{d}S + \oint_{\mathcal{S}_b} \boldsymbol{x} \times \frac{1}{2} u^2 \boldsymbol{n} \, \mathrm{d}S \\ &+ \frac{1}{\mathcal{N}_d} \int_{\mathcal{S}_b} \boldsymbol{n} \cdot \big(\boldsymbol{\omega}[\boldsymbol{x} \times (\boldsymbol{x} \times \boldsymbol{u})] - \boldsymbol{u}[\boldsymbol{x} \times (\boldsymbol{x} \times \boldsymbol{\omega})]\big) \, \mathrm{d}S. \end{aligned} \tag{C.27}$$

The last step is to get the time derivative out of the first integral. This is performed by noticing that

$$\boldsymbol{x} \times [\boldsymbol{x} \ \times (\boldsymbol{n} \times \boldsymbol{a})] = \boldsymbol{x} \times (\boldsymbol{x} \cdot \boldsymbol{a})\boldsymbol{n} - \boldsymbol{n} \cdot [\boldsymbol{x}(\boldsymbol{x} \times \boldsymbol{a})], \tag{C.28}$$

which allows to use both Eqs. (C.53) and (C.55) to find

$$\begin{aligned} \oint_{\mathcal{S}_b} \boldsymbol{x} \times \left[\boldsymbol{x} \times \left(\boldsymbol{n} \times \frac{\partial \boldsymbol{u}}{\partial t}\right)\right] \, \mathrm{d}S = &\frac{\mathrm{d}}{\mathrm{d}t} \oint_{\mathcal{S}_b} \boldsymbol{x} \times [\boldsymbol{x} \times (\boldsymbol{n} \times \boldsymbol{u})] \, \mathrm{d}S \\ &+ \oint_{\mathcal{S}_b} \big(\nabla \cdot [\boldsymbol{x}(\boldsymbol{x} \times \boldsymbol{u})] - \boldsymbol{x} \times \nabla(\boldsymbol{x} \cdot \boldsymbol{u})\big)\boldsymbol{u}_b \cdot \boldsymbol{n} \, \mathrm{d}S \\ = &\frac{\mathrm{d}}{\mathrm{d}t} \oint_{\mathcal{S}_b} \boldsymbol{x} \times [\boldsymbol{x} \times (\boldsymbol{n} \times \boldsymbol{u})] \, \mathrm{d}S \\ &+ \oint_{\mathcal{S}_b} [\mathcal{N}_d \boldsymbol{x} \times \boldsymbol{u} - \boldsymbol{x} \times (\boldsymbol{x} \times \boldsymbol{\omega})]\boldsymbol{u}_b \cdot \boldsymbol{n} \, \mathrm{d}S \end{aligned} \tag{C.29}$$

where the last integral results from Eqs. (C.46), (C.47), and (C.50).

Finally, we can assemble all pieces together to give an expression for the aerodynamic moment:

$$\begin{aligned} \boldsymbol{m}_0 = &\oint_{\mathcal{S}_b} \boldsymbol{x} \times \left(\frac{1}{2} u^2 \boldsymbol{n} - \boldsymbol{u}\boldsymbol{u}_b \cdot \boldsymbol{n}\right) \, \mathrm{d}S - \frac{1}{\mathcal{N}_d} \frac{\mathrm{d}}{\mathrm{d}t} \oint_{\mathcal{S}_b} \boldsymbol{x} \times [\boldsymbol{x} \times (\boldsymbol{n} \times \boldsymbol{u})] \, \mathrm{d}S \\ &+ \frac{1}{\mathcal{N}_d} \oint_{\mathcal{S}_b} \boldsymbol{n} \cdot \Big(\boldsymbol{\omega}[\boldsymbol{x} \times (\boldsymbol{x} \times \boldsymbol{u})] - (\boldsymbol{u} - \boldsymbol{u}_b)[\boldsymbol{x} \times (\boldsymbol{x} \times \boldsymbol{\omega})]\Big) \, \mathrm{d}S \end{aligned} \tag{C.30}$$

which in two-dimensions gives

$$\begin{aligned} \boldsymbol{m}_0 = &\oint_{\mathcal{S}_b} \boldsymbol{x} \times \left(\frac{1}{2} u^2 \boldsymbol{n} - \boldsymbol{u}\boldsymbol{u}_b \cdot \boldsymbol{n}\right) \, \mathrm{d}S - \frac{1}{2} \frac{\mathrm{d}}{\mathrm{d}t} \oint_{\mathcal{S}_b} \boldsymbol{x} \times [\boldsymbol{x} \times (\boldsymbol{n} \times \boldsymbol{u})] \, \mathrm{d}S \\ &- \frac{1}{2} \oint_{\mathcal{S}_b} \boldsymbol{n} \cdot (\boldsymbol{u} - \boldsymbol{u}_b)[\boldsymbol{x} \times (\boldsymbol{x} \times \boldsymbol{\omega})] \, \mathrm{d}S. \end{aligned} \tag{C.31}$$

Again, this result can be adapted for a frame of reference that follows the center of mass of the body

$$\boldsymbol{m}_{cm} = \oint_{\mathcal{S}_b} \boldsymbol{x}' \times \left(\frac{1}{2}u'^2\boldsymbol{n} - \boldsymbol{u}'\boldsymbol{u}_b' \cdot \boldsymbol{n}\right)\,\mathrm{d}S - \frac{1}{2}\frac{\mathrm{d}}{\mathrm{d}t}\oint_{\mathcal{S}_b} \boldsymbol{x}' \times [\boldsymbol{x}' \times (\boldsymbol{n} \times \boldsymbol{u})]\,\mathrm{d}S \\ - \frac{1}{2}\oint_{\mathcal{S}_b} \boldsymbol{n} \cdot (\boldsymbol{u} - \boldsymbol{u}_b)[\boldsymbol{x}' \times (\boldsymbol{x}' \times \boldsymbol{\omega})]\,\mathrm{d}S + \dot{\boldsymbol{x}}_{cm} \times \left(\oint_{\mathcal{S}_b} \boldsymbol{n} \cdot \boldsymbol{u}_b \boldsymbol{x}'\,\mathrm{d}S\right). \tag{C.32}$$

Proof. We begin by stating the relationship between the moments evaluated at these different points:

$$\boldsymbol{m}_{cm} - (\boldsymbol{m}_0 - \boldsymbol{x}_{cm} \times \boldsymbol{f}) = \boldsymbol{0}. \tag{C.33}$$

To proof this, we consider the left hand side as being composed of three surface integrals and a corrective term. Then, we use Eqs. (C.46), (C.47), (C.49) and (C.50) as well as Green's Theorem to express the first integral in Eq. (C.31) as

$$\oint_{\mathcal{S}_b} \boldsymbol{x} \times \left(\frac{1}{2}u^2\boldsymbol{n} - \boldsymbol{u}\boldsymbol{u}_b \cdot \boldsymbol{n}\right)\,\mathrm{d}S = \int_{\mathcal{V}_b} \boldsymbol{x} \times (\boldsymbol{u} \times \boldsymbol{\omega})\,\mathrm{d}V + \oint_{\mathcal{S}_b} \boldsymbol{n} \cdot (\boldsymbol{u} - \boldsymbol{u}_b)(\boldsymbol{x} \times \boldsymbol{u})\,\mathrm{d}S, \tag{C.34}$$

and the first one in Eq. (C.32) as

$$\oint_{\mathcal{S}_b} \boldsymbol{x}' \times \left(\frac{1}{2}u'^2\boldsymbol{n} - \boldsymbol{u}'\boldsymbol{u}_b' \cdot \boldsymbol{n}\right)\,\mathrm{d}S = \int_{\mathcal{V}_b} \boldsymbol{x}' \times (\boldsymbol{u}' \times \boldsymbol{\omega})\,\mathrm{d}V \\ + \oint_{\mathcal{S}_b} \boldsymbol{n} \cdot (\boldsymbol{u} - \boldsymbol{u}_b)(\boldsymbol{x}' \times \boldsymbol{u}')\,\mathrm{d}S. \tag{C.35}$$

In addition, taking the cross product between $\boldsymbol{x}_{cm}$ and the first integral of Eq. (C.11), we get

$$\oint_{\mathcal{S}_b} \boldsymbol{x}_{cm} \times \left(\frac{1}{2}u^2\boldsymbol{n} - \boldsymbol{u}\boldsymbol{u}_b \cdot \boldsymbol{n}\right)\,\mathrm{d}S = \int_{\mathcal{V}_b} \boldsymbol{x}_{cm} \times (\boldsymbol{u} \times \boldsymbol{\omega})\,\mathrm{d}V \\ + \oint_{\mathcal{S}_b} \boldsymbol{n} \cdot (\boldsymbol{u} - \boldsymbol{u}_b)(\boldsymbol{x}_{cm} \times \boldsymbol{u})\,\mathrm{d}S. \tag{C.36}$$

After noting that the following holds for planar vectors $\boldsymbol{a}$ and $\boldsymbol{b}$

$$\boldsymbol{a} \times (\boldsymbol{b} \times \varphi\hat{\boldsymbol{e}}_z) = -(\boldsymbol{a} \cdot \boldsymbol{b})\varphi\hat{\boldsymbol{e}}_z = \boldsymbol{b} \times (\boldsymbol{a} \times \varphi\hat{\boldsymbol{e}}_z), \tag{C.37}$$

we can compute the first integral of Eq. (C.33) as

$$\begin{aligned}
\boldsymbol{I}_1 &= \oint_{\mathcal{S}_b} \left[\boldsymbol{x}' \times \left(\frac{1}{2} u'^2 \boldsymbol{n} - \boldsymbol{u}' \boldsymbol{u}_b' \cdot \boldsymbol{n} \right) - (\boldsymbol{x} - \boldsymbol{x}_{cm}) \times \left(\frac{1}{2} u^2 \boldsymbol{n} - \boldsymbol{u} \boldsymbol{u}_b \cdot \boldsymbol{n} \right) \right] \mathrm{d}S \\
&= \dot{\boldsymbol{x}}_{cm} \times \left(\int_{\mathcal{V}_b} -\boldsymbol{x}' \times \boldsymbol{\omega} \, \mathrm{d}V + \oint_{\mathcal{S}_b} \boldsymbol{n} \cdot (\boldsymbol{u} - \boldsymbol{u}_b) \boldsymbol{x}' \, \mathrm{d}S \right) \\
&= \dot{\boldsymbol{x}}_{cm} \times \left(\int_{\mathcal{V}_b} -\boldsymbol{x}' \times \boldsymbol{\omega} \, \mathrm{d}V + \int_{\mathcal{V}_b} (\boldsymbol{u} - \boldsymbol{u}_b) \, \mathrm{d}V \right).
\end{aligned} \tag{C.38}$$

To derive the second integral of Eq. (C.33), we use the fact that

$$\boldsymbol{x}_{cm} \times \left(\frac{\mathrm{d}}{\mathrm{d}t} \int_{\mathcal{V}_b} \boldsymbol{a} \, \mathrm{d}V \right) = \frac{\mathrm{d}}{\mathrm{d}t} \int_{\mathcal{V}_b} \boldsymbol{x}_{cm} \times \boldsymbol{a} \, \mathrm{d}V - \dot{\boldsymbol{x}}_{cm} \times \left(\int_{\mathcal{V}_b} \boldsymbol{a} \, \mathrm{d}V \right), \tag{C.39}$$

so that we can regroup the time derivatives as

$$\begin{aligned}
\boldsymbol{I}_2 =& -\frac{1}{2} \frac{\mathrm{d}}{\mathrm{d}t} \oint_{\mathcal{S}_b} \left(\boldsymbol{x}' \times [\boldsymbol{x}' \times (\boldsymbol{n} \times \boldsymbol{u})] - (\boldsymbol{x} - 2\boldsymbol{x}_{cm}) \times [\boldsymbol{x} \times (\boldsymbol{n} \times \boldsymbol{u})] \right) \mathrm{d}S \\
& + \dot{\boldsymbol{x}}_{cm} \times \left(\oint_{\mathcal{S}_b} \boldsymbol{x} \times (\boldsymbol{n} \times \boldsymbol{u}) \, \mathrm{d}S \right) \\
=& \frac{1}{2} \frac{\mathrm{d}}{\mathrm{d}t} \oint_{\mathcal{S}_b} \left(\boldsymbol{x}' \times [\boldsymbol{x}_{cm} \times (\boldsymbol{n} \times \boldsymbol{u})] - \boldsymbol{x}_{cm} \times [\boldsymbol{x} \times (\boldsymbol{n} \times \boldsymbol{u})] \right) \mathrm{d}S \\
& + \dot{\boldsymbol{x}}_{cm} \times \left(\oint_{\mathcal{S}_b} \boldsymbol{x} \times (\boldsymbol{n} \times \boldsymbol{u}) \, \mathrm{d}S \right) \\
=& -\frac{1}{2} \frac{\mathrm{d}}{\mathrm{d}t} \oint_{\mathcal{S}_b} \boldsymbol{x}_{cm} \times [\boldsymbol{x}_{cm} \times (\boldsymbol{n} \times \boldsymbol{u})] \, \mathrm{d}S + \dot{\boldsymbol{x}}_{cm} \times \left(\oint_{\mathcal{S}_b} \boldsymbol{x} \times (\boldsymbol{n} \times \boldsymbol{u}) \, \mathrm{d}S \right) \\
=& -\frac{1}{2} \frac{\mathrm{d}}{\mathrm{d}t} \int_{\mathcal{V}_b} \boldsymbol{x}_{cm} \times (\boldsymbol{x}_{cm} \times \boldsymbol{\omega}) \, \mathrm{d}V + \dot{\boldsymbol{x}}_{cm} \times \left(\oint_{\mathcal{S}_b} \boldsymbol{x} \times (\boldsymbol{n} \times \boldsymbol{u}) \, \mathrm{d}S \right),
\end{aligned} \tag{C.40}$$

where we use Green's Theorem to obtain the last equality. The third integral of Eq. (C.33) is

$$\begin{aligned}
\boldsymbol{I}_3 &= -\frac{1}{2}\oint_{\mathscr{S}_b} \boldsymbol{n}\cdot(\boldsymbol{u}-\boldsymbol{u}_b)[\,\boldsymbol{x}'\times(\boldsymbol{x}'\times\boldsymbol{\omega}) - \boldsymbol{x}\times(\boldsymbol{x}\times\boldsymbol{\omega}) + 2\boldsymbol{x}_{cm}\times(\boldsymbol{x}\times\boldsymbol{\omega})]\,\mathrm{d}S \\
&= \frac{1}{2}\oint_{\mathscr{S}_b} \boldsymbol{n}\cdot(\boldsymbol{u}-\boldsymbol{u}_b)[\,\boldsymbol{x}'\times(\boldsymbol{x}_{cm}\times\boldsymbol{\omega}) - \boldsymbol{x}_{cm}\times(\boldsymbol{x}\times\boldsymbol{\omega})]\,\mathrm{d}S \\
&= -\frac{1}{2}\oint_{\mathscr{S}_b} \boldsymbol{n}\cdot(\boldsymbol{u}-\boldsymbol{u}_b)\,\boldsymbol{x}_{cm}\times(\boldsymbol{x}_{cm}\times\boldsymbol{\omega})\,\mathrm{d}S.
\end{aligned} \tag{C.41}$$

Prior to putting everything together, the sum of $\boldsymbol{I}_2$ and $\boldsymbol{I}_3$ is

$$\begin{aligned}
\boldsymbol{I}_2 + \boldsymbol{I}_3 &= -\frac{1}{2}\frac{\mathrm{d}}{\mathrm{d}t}\int_{\mathscr{V}_{bm}} \boldsymbol{x}_{cm}\times(\boldsymbol{x}_{cm}\times\boldsymbol{\omega})\,\mathrm{d}V + \dot{\boldsymbol{x}}_{cm}\times\left(\oint_{\mathscr{S}_b} \boldsymbol{x}\times(\boldsymbol{n}\times\boldsymbol{u})\,\mathrm{d}S\right) \\
&= -\dot{\boldsymbol{x}}_{cm}\times\left(\boldsymbol{x}_{cm}\times\int_{\mathscr{V}_b}\boldsymbol{\omega}\,\mathrm{d}V\right) + \dot{\boldsymbol{x}}_{cm}\times\left(\oint_{\mathscr{S}_b} \boldsymbol{x}\times(\boldsymbol{n}\times\boldsymbol{u})\,\mathrm{d}S\right) \\
&= \dot{\boldsymbol{x}}_{cm}\times\left(\oint_{\mathscr{S}_b} \boldsymbol{x}'\times(\boldsymbol{n}\times\boldsymbol{u})\,\mathrm{d}S\right),
\end{aligned} \tag{C.42}$$

where we used the conservation of vorticity on a two-dimensional material volume as well as Green's Theorem on the vorticity integral. By adding a corrective term accounting for the displacement of momentum, we can rewrite Eq. (C.33) as

$$\begin{aligned}
\boldsymbol{0} &= \boldsymbol{m}_{cm} - (\boldsymbol{m}_0 - \boldsymbol{x}_{cm}\times\boldsymbol{f}) \\
&= \boldsymbol{I}_1 + \boldsymbol{I}_2 + \boldsymbol{I}_3 + \dot{\boldsymbol{x}}_{cm}\times\left(\int_{\mathscr{V}_b}\boldsymbol{u}_b\,\mathrm{d}V\right) \\
&= \dot{\boldsymbol{x}}_{cm}\times\left(\int_{\mathscr{V}_b} -\boldsymbol{x}'\times\boldsymbol{\omega}\,\mathrm{d}V + \oint_{\mathscr{S}_b}\boldsymbol{x}'\times(\boldsymbol{n}\times\boldsymbol{u})\,\mathrm{d}S + \int_{\mathscr{V}_b}\boldsymbol{u}\,\mathrm{d}V\right) \\
&= \boldsymbol{0}
\end{aligned} \tag{C.43}$$

in virtue of Eq. (C.56).

Finally, we can easily transform the volume integral of the corrective term into a surface integral

$$\dot{\boldsymbol{x}}_{cm}\times\left(\int_{\mathscr{V}_b}\boldsymbol{u}_b\,\mathrm{d}V\right) = \dot{\boldsymbol{x}}_{cm}\times\left(\oint_{\mathscr{S}_b}\boldsymbol{n}\cdot\boldsymbol{u}_b\boldsymbol{x}'\,\mathrm{d}S\right) \tag{C.44}$$

thanks to the incompressibility of the body motion, Green's Divergence Theorem and Eq. (C.47). □

C.4 Useful identities

C.4.1 Vector identities

$$\boldsymbol{a} \times (\boldsymbol{b} \times \boldsymbol{c}) = (\boldsymbol{a} \cdot \boldsymbol{c})\boldsymbol{b} - (\boldsymbol{a} \cdot \boldsymbol{b})\boldsymbol{c} \tag{C.45}$$

$$\nabla(\boldsymbol{a} \cdot \boldsymbol{b}) = \boldsymbol{a} \times (\nabla \times \boldsymbol{b}) + \boldsymbol{b} \times (\nabla \times \boldsymbol{a}) + \boldsymbol{a} \cdot \nabla \boldsymbol{b} + \boldsymbol{b} \cdot \nabla \boldsymbol{a} \tag{C.46}$$

$$\nabla \cdot (\boldsymbol{a}\boldsymbol{b}) = (\nabla \cdot \boldsymbol{a})\boldsymbol{b} + \boldsymbol{a} \cdot \nabla\, \boldsymbol{b} \tag{C.47}$$

$$\nabla(\varphi \boldsymbol{a}) = \nabla\varphi \boldsymbol{a} + \varphi \nabla \boldsymbol{a} \tag{C.48}$$

$$\nabla \times (\varphi \boldsymbol{a}) = \nabla\varphi \times \boldsymbol{a} + \varphi \nabla \times \boldsymbol{a} \tag{C.49}$$

$$\boldsymbol{a} \cdot \nabla(\boldsymbol{b} \times \boldsymbol{c}) = (\boldsymbol{a} \cdot \nabla \boldsymbol{b}) \times \boldsymbol{c} - (\boldsymbol{a} \cdot \nabla \boldsymbol{c}) \times \boldsymbol{b} \tag{C.50}$$

C.4.2 Time differentiation of volume and integrals

Let us give here a few relations for the time derivative of volume and surface integrals.

We first give the time derivative of the volume integral of any quantity φ

$$\frac{\mathrm{d}}{\mathrm{d}t} \int_{\mathscr{V}} \varphi \, \mathrm{d}V = \int_{\mathscr{V}} \frac{\partial \varphi}{\partial t} \, \mathrm{d}V + \oint_{\mathscr{S}} \boldsymbol{n} \cdot \boldsymbol{u}_s \varphi \, \mathrm{d}S \tag{C.51}$$

The transport of a scalar field ϕ along a moving surface is

$$\frac{\mathrm{d}}{\mathrm{d}t} \int_{\mathscr{S}} \varphi \boldsymbol{n} \, \mathrm{d}S = \int_{\mathscr{S}} \left(\frac{\partial \varphi}{\partial t} \boldsymbol{n} + \nabla\varphi \boldsymbol{u}_s \cdot \boldsymbol{n} \right) \mathrm{d}S \tag{C.52}$$

where $\boldsymbol{u}_s$ is the velocity of the surface.

Similarly, the first moment of this relation also holds:

$$\frac{\mathrm{d}}{\mathrm{d}t} \int_{\mathscr{S}} \boldsymbol{x} \times \varphi \boldsymbol{n} \, \mathrm{d}S = \int_{\mathscr{S}} \boldsymbol{x} \times \left(\frac{\partial \varphi}{\partial t} \boldsymbol{n} + \nabla\varphi \boldsymbol{u}_s \cdot \boldsymbol{n} \right) \mathrm{d}S \tag{C.53}$$

Now, we look at the rate of change in the flux of a vector field out of an arbitrary volume.

$$\frac{\mathrm{d}}{\mathrm{d}t} \int_{\mathscr{V}} \nabla \cdot \boldsymbol{a} \, \mathrm{d}V = \frac{\mathrm{d}}{\mathrm{d}t} \oint_{\mathscr{S}} \boldsymbol{a} \cdot \boldsymbol{n} \, \mathrm{d}S = \oint_{\mathscr{S}} \left(\frac{\partial \boldsymbol{a}}{\partial t} + (\nabla \cdot \boldsymbol{a}) \boldsymbol{u}_s \right) \cdot \boldsymbol{n} \, \mathrm{d}S. \tag{C.54}$$

The generalization of Eq. (C.54) for a 2-rank tensor is

$$\frac{\mathrm{d}}{\mathrm{d}t} \oint_{\mathscr{S}} \boldsymbol{A} \cdot \boldsymbol{n} \, \mathrm{d}S = \oint_{\mathscr{S}} \left(\frac{\partial \boldsymbol{A}}{\partial t} + (\nabla \cdot \boldsymbol{A}) \boldsymbol{u}_s \right) \cdot \boldsymbol{n} \, \mathrm{d}S. \tag{C.55}$$

C.4.3 Burgatti's identities

It is useful to note that both the first and second moments of vorticity integrated on a volume can be expressed as integrals that only depend on the velocity field. These equivalences will be referred to Burgatti's identities. This section presents these expressions as well as how to obtain them.

We begin with the integral of the first moment of vorticity:

$$\int_{\mathscr{V}} \boldsymbol{x} \times \boldsymbol{\omega} \, \mathrm{d}V = (\mathscr{N}_d - 1) \int_{\mathscr{V}} \boldsymbol{u} \, \mathrm{d}V + \oint_{\mathscr{S}} \boldsymbol{x} \times (\boldsymbol{n} \times \boldsymbol{u}) \, \mathrm{d}S. \tag{C.56}$$

Proof. Using Eqs. (C.46) and (C.47), we can show that

$$(\mathscr{N}_d - 1)\boldsymbol{u} = \boldsymbol{x} \times \boldsymbol{\omega} - \nabla(\boldsymbol{x} \cdot \boldsymbol{u}) + \nabla \cdot (\boldsymbol{x}\boldsymbol{u}). \tag{C.57}$$

Now, taking the volume integral of this equation, we can use Green's Theorem to get a surface integral

$$(\mathscr{N}_d - 1) \int_{\mathscr{V}} \boldsymbol{u} \, \mathrm{d}V = \int_{\mathscr{V}} \boldsymbol{x} \times (\nabla \times \boldsymbol{u}) \, \mathrm{d}V + \oint_{\mathscr{S}} \big(\boldsymbol{n} \cdot \boldsymbol{x}\boldsymbol{u} - (\boldsymbol{x} \cdot \boldsymbol{u})\boldsymbol{n}\big) \, \mathrm{d}S. \tag{C.58}$$

The proof ends when applying Eq. (C.45) on the integrand of the surface integral. □

Remarkably, Burgatti's second identity closely resembles to the first one:

$$\int_{\mathscr{V}} \boldsymbol{x} \times (\boldsymbol{x} \times \boldsymbol{\omega}) \, \mathrm{d}V = \mathscr{N}_d \int_{\mathscr{V}} \boldsymbol{x} \times \boldsymbol{u} \, \mathrm{d}V + \oint_{\mathscr{S}} \boldsymbol{x} \times [\boldsymbol{x} \times (\boldsymbol{n} \times \boldsymbol{u})] \, \mathrm{d}S. \tag{C.59}$$

Proof. By using Eq. (C.45), Green's Theorem, Eqs. (C.49) and (C.50), we can write the surface integral as

$$\begin{aligned}
\oint_{\mathscr{S}} \boldsymbol{x} \times [\boldsymbol{x} \times (\boldsymbol{n} \times \boldsymbol{u})] \, \mathrm{d}S &= \oint_{\mathscr{S}} \Big((\boldsymbol{x} \cdot \boldsymbol{u})\boldsymbol{x} \times \boldsymbol{n} - (\boldsymbol{x} \cdot \boldsymbol{n})\boldsymbol{x} \times \boldsymbol{u}\Big) \, \mathrm{d}S \\
&= \oint_{\mathscr{S}} \Big(- \boldsymbol{n} \times (\boldsymbol{x} \cdot \boldsymbol{u})\boldsymbol{x} - \boldsymbol{n} \cdot \boldsymbol{x}(\boldsymbol{x} \times \boldsymbol{u})\Big) \, \mathrm{d}S \\
&= \int_{\mathscr{V}} \Big(- \nabla \times [(\boldsymbol{x} \cdot \boldsymbol{u}) \times \boldsymbol{x}] - \nabla \cdot [\boldsymbol{x}(\boldsymbol{x} \times \boldsymbol{u})] \Big) \, \mathrm{d}V \\
&= \int_{\mathscr{V}} \Big(\boldsymbol{x} \times \nabla(\boldsymbol{x} \cdot \boldsymbol{u}) - \boldsymbol{x} \times (\boldsymbol{x} \cdot \nabla\boldsymbol{u}) - (\mathscr{N}_d + 1)\boldsymbol{x} \times \boldsymbol{u}\Big) \, \mathrm{d}V.
\end{aligned} \tag{C.60}$$

Then, by taking the volume integral of the cross product of $\boldsymbol{x}$ and Eq. (C.57), we obtain

$$(\mathcal{N}_d - 1)\int_{\mathcal{V}} \boldsymbol{x}\times\boldsymbol{u}\,\mathrm{d}V = \int_{\mathcal{V}} \boldsymbol{x}\times(\boldsymbol{x}\times\boldsymbol{\omega})\,\mathrm{d}V - \int_{\mathcal{V}} \boldsymbol{x}\times[\nabla(\boldsymbol{x}\cdot\boldsymbol{u}) - \nabla\cdot(\boldsymbol{x}\boldsymbol{u})]\;\mathrm{d}V. \tag{C.61}$$

We can now add and subtract both sides of Eq. (C.60) to the right hand side of this result to obtain

$$\begin{aligned}(\mathcal{N}_d - 1)\int_{\mathcal{V}} \boldsymbol{x}\times\boldsymbol{u}\,\mathrm{d}V = &\int_{\mathcal{V}} \boldsymbol{x}\times(\boldsymbol{x}\times\boldsymbol{\omega})\,\mathrm{d}V - \oint_{\mathcal{S}} \boldsymbol{x}\times[\boldsymbol{x}\times(\boldsymbol{n}\times\boldsymbol{u})]\;\mathrm{d}S \\ &- \int_{\mathcal{V}} \boldsymbol{x}\times[\nabla(\boldsymbol{x}\cdot\boldsymbol{u}) - \nabla\cdot(\boldsymbol{x}\boldsymbol{u})]\;\mathrm{d}V \\ &+ \int_{\mathcal{V}} \Big(\boldsymbol{x}\times\nabla(\boldsymbol{x}\cdot\boldsymbol{u}) - \boldsymbol{x}\times(\boldsymbol{x}\cdot\nabla\boldsymbol{u}) - (\mathcal{N}_d + 1)\boldsymbol{x}\times\boldsymbol{u}\Big)\,\mathrm{d}V.\end{aligned} \tag{C.62}$$

Finally, using Eq. (C.47), we get the final result

$$\mathcal{N}_d\int_{\mathcal{V}} \boldsymbol{x}\times\boldsymbol{u}\,\mathrm{d}V = \int_{\mathcal{V}} \boldsymbol{x}\times(\boldsymbol{x}\times\boldsymbol{\omega})\,\mathrm{d}V - \oint_{\mathcal{S}} \boldsymbol{x}\times[\boldsymbol{x}\times(\boldsymbol{n}\times\boldsymbol{u})]\;\mathrm{d}S. \tag{C.63}$$

□

APPENDIX D

Time Integration

Consider an immersed body with mass matrix $\boldsymbol{M}_b$ and moment of inertia $\boldsymbol{I}_b$. It has matrices of added mass $\boldsymbol{M}^{\zeta\zeta}$, $\boldsymbol{M}^{\zeta\chi}$, and added inertia $\boldsymbol{M}^{\chi\zeta}$ and $\boldsymbol{M}^{\chi\chi}$ as defined in Section 2.1.1. It is in rigid motion with linear velocity $\boldsymbol{u}$ and angular velocity $\boldsymbol{\Omega}$. It undergoes a circulatory force $\boldsymbol{f}_v$ and moment $\boldsymbol{l}_v$ induced by ambient vorticity. Then, we can derive its equations of motion.

D.1 In the inertial frame of reference

In this Section, we consider terms of the added mass/inertia matrices computed in the inertial frame of reference.

D.1.1 Linear equilibrium

$$\frac{\mathrm{d}}{\mathrm{d}t}\left(\boldsymbol{M}_b\boldsymbol{u}\right) = \boldsymbol{f}_v - \frac{\mathrm{d}}{\mathrm{d}t}\left(\boldsymbol{M}^{\zeta\zeta}\boldsymbol{u}\right) - \frac{\mathrm{d}}{\mathrm{d}t}\left(\boldsymbol{M}^{\zeta\chi}\boldsymbol{\Omega}\right) \tag{D.1}$$

$$\left(\boldsymbol{M}^{\zeta\zeta} + \boldsymbol{M}_b\right)\frac{\mathrm{d}\boldsymbol{u}}{\mathrm{d}t} + \boldsymbol{M}^{\zeta\chi}\frac{\mathrm{d}\boldsymbol{\Omega}}{\mathrm{d}t} = \boldsymbol{f}_v - \left(\dot{\boldsymbol{M}}^{\zeta\zeta} + \dot{\boldsymbol{M}}_b\right)\boldsymbol{u} - \dot{\boldsymbol{M}}^{\zeta\chi}\boldsymbol{\Omega} \tag{D.2}$$

D.1.2 Angular equilibrium

$$\begin{aligned}\frac{\mathrm{d}}{\mathrm{d}t}\left(\boldsymbol{I}_b\boldsymbol{\Omega}\right) = \boldsymbol{l}_v - \boldsymbol{x}\times\boldsymbol{f}_v - \frac{\mathrm{d}}{\mathrm{d}t}(\boldsymbol{M}^{\chi\chi}\boldsymbol{\Omega}) + \boldsymbol{x}\times\frac{\mathrm{d}}{\mathrm{d}t}\left(\boldsymbol{M}^{\zeta\zeta}\boldsymbol{u}\right) \\ - \frac{\mathrm{d}}{\mathrm{d}t}\left(\boldsymbol{M}^{\chi\zeta}\boldsymbol{u}\right) + \boldsymbol{x}\times\frac{\mathrm{d}}{\mathrm{d}t}\left(\boldsymbol{M}^{\zeta\chi}\boldsymbol{\Omega}\right)\end{aligned} \tag{D.3}$$

$$\begin{aligned}\left(\boldsymbol{M}^{\chi\chi} + \boldsymbol{I}_b - [\boldsymbol{x}]_\times \boldsymbol{M}^{\zeta\chi}\right) \frac{\mathrm{d}\boldsymbol{\Omega}}{\mathrm{d}t} + \left(\boldsymbol{M}^{\chi\zeta} - [\boldsymbol{x}]_\times \boldsymbol{M}^{\zeta\zeta}\right) \frac{\mathrm{d}\boldsymbol{u}}{\mathrm{d}t} = \\ \left(\boldsymbol{l}_v - [\boldsymbol{x}]_\times \boldsymbol{f}_v\right) - \left(\dot{\boldsymbol{M}}^{\chi\chi} + \dot{\boldsymbol{I}}_b - [\boldsymbol{x}]_\times \dot{\boldsymbol{M}}^{\zeta\chi}\right)\boldsymbol{\Omega} - \left(\dot{\boldsymbol{M}}^{\chi\zeta} - [\boldsymbol{x}]_\times \dot{\boldsymbol{M}}^{\zeta\zeta}\right)\boldsymbol{u}\end{aligned} \tag{D.4}$$

D.1.3 Plücker notation for two-dimensional problems

The Plücker notation allows to regroup the linear and angular equilibria into one single equation for planar problems, by regrouping the associated variables into an augmented variable. Let's define $\boldsymbol{v} = [u, v, \Omega]^T$, $\tilde{\boldsymbol{f}}_v = [f_{v,x}, f_{v,y}, l_v]^T$, $\tilde{\boldsymbol{M}}_b = \begin{bmatrix} M_b & 0 & 0 \\ 0 & M_b & 0 \\ 0 & 0 & I_b \end{bmatrix}$ and $\boldsymbol{M}_a = \begin{bmatrix} \boldsymbol{M}^{\zeta\zeta} & \boldsymbol{M}^{\zeta\chi} \\ \boldsymbol{M}^{\chi\zeta} & \boldsymbol{M}^{\chi\chi} \end{bmatrix}$. We also define the matrix $\boldsymbol{A} = \mathbb{I} - [\boldsymbol{x}]_\times = \begin{bmatrix} 1 & 0 & 0 \\ 0 & 1 & 0 \\ y & -x & 1 \end{bmatrix}$.

Then the coupled system of equations turns into

$$(\boldsymbol{A}\boldsymbol{M}_a + \tilde{\boldsymbol{M}}_b)\dot{\boldsymbol{v}} = \boldsymbol{A}\tilde{\boldsymbol{f}}_v - (\boldsymbol{A}\dot{\boldsymbol{M}}_a + \dot{\tilde{\boldsymbol{M}}}_b)\boldsymbol{v} \tag{D.5}$$

which can be integrated for $\dot{\boldsymbol{v}}$ with our favourite scheme.

D.2 In the frame of reference following center of mass of the body

D.2.1 Linear equilibrium

The equation for the linear equilibrium is the same as in the previous section.

D.2.2 Angular equilibrium

The angular moment of the body depends on its point of application. In the frame of reference following the body (but not rigidly attached to it), it can be formulated as the sum of contributions from the vorticity in the flow, the added mass effects due to body acceleration and finally a term accounting for the displacement of momentum in the flow. We write it

$$\boldsymbol{l} = \boldsymbol{l}_v - \frac{\mathrm{d}}{\mathrm{d}t}\left(\boldsymbol{M}^{\chi\chi}\boldsymbol{\Omega} + \boldsymbol{M}^{\chi\zeta}\boldsymbol{u}\right) - \boldsymbol{u} \times (\boldsymbol{M}^{\zeta\zeta}\boldsymbol{u} + \boldsymbol{M}^{\zeta\chi}\boldsymbol{\Omega}). \tag{D.6}$$

Therefore, the equilibrium of angular momentum takes the form

$$(\boldsymbol{M}^{\chi\chi} + \boldsymbol{I}_b)\frac{\mathrm{d}\boldsymbol{\Omega}}{\mathrm{d}t} + \boldsymbol{M}^{\chi\zeta}\frac{\mathrm{d}\boldsymbol{u}}{\mathrm{d}t} = \boldsymbol{l}_v - (\dot{\boldsymbol{M}}^{\chi\chi} + \dot{\boldsymbol{I}}_b)\boldsymbol{\Omega} - \dot{\boldsymbol{M}}^{\chi\zeta}\boldsymbol{u} - \boldsymbol{u}\times(\boldsymbol{M}^{\zeta\zeta}\boldsymbol{u} + \boldsymbol{M}^{\zeta\chi}\boldsymbol{\Omega}). \tag{D.7}$$

D.2.3 Plücker notation

Using the Plücker notation, the total equilibrium is written

$$(\boldsymbol{M}_a + \tilde{\boldsymbol{M}}_b)\dot{\boldsymbol{v}} = \tilde{\boldsymbol{f}}_v - (\dot{\boldsymbol{M}}_a + \dot{\tilde{\boldsymbol{M}}}_b + [\boldsymbol{v}]_\times \boldsymbol{M}_a)\boldsymbol{v}. \tag{D.8}$$

APPENDIX **E**

Code structure

E.1 `VSFlow.jl`

This package deals with the unsteady dynamics of rigid airfoils with imposed kinematics. It can be accelerated through vorticity lumping.

The package can be found by browsing `http://www.github.com/yosinlpet/VSFlow.jl` and is organized as follows:

```
VSFlow
├── Project.toml
├── Manifest.toml
├── ReadMe.md
└── src
    ├── Airfoil.jl
    ├── History.jl
    ├── Utils.jl
    ├── VortexElement.jl
    └── VSFlow.jl
```

E.1.1 Package files

In addition to the `ReadMe` file whose purpose is straightforward. Any *julia* package contains a `Project.toml` and a `Manifest.toml`. Amongst other things, these files specify the dependencies and their compatible versions.

E.1.2 `Airfoil.jl`

This file contains all the functions used to generate the airfoil geometry and prescribe its kinematics.

E.1.3 `History.jl`

The current state of a simulation is stored in the `History` data structure. It contains the position, velocity, velocity potential, pressure, impulse history and aerodynamic coefficients of the airfoil.

E.1.4 `Utils.jl`

This file regroups all mathematical utilities like numerical derivation and integration tools, overriden operators like the *planar* cross product, etc.

E.1.5 `VortexElement.jl`

This code contains the data structures representing vorticity it defines the point vortex and the vortex panel. It is there that any analytical integration over panels is performed.

E.1.6 `VSFlow.jl`

Finally, this file contains the bulk of the program. It displaces the airfoil, solves the linear system for bound vorticity, performs the time marching step, compute aerodynamic coefficients. It also orchestrates the other files.

E.2 `Swimmers.jl`

This is the package to use for biolocomotion of anguilliform swimmers. It embeds the framework with inverse and direct MBS dynamics and enables simulations involving multiple swimmers. Since this package is a sensibly more sizeable chunk, it is separated into more files each having its own well-defined purpose.

The package is organized as follows:

```
Swimmers
├── Manifest.toml
├── Project.toml
├── ReadMe.md
└── src
    ├── Airfoil.jl
    ├── Common.jl
    ├── DirMBS.jl
    ├── DirFish.jl
    ├── Forces.jl
    ├── InvFish.jl
    ├── InvMBS.jl
    ├── MBS.jl
    ├── MultiFish.jl
    ├── Swimmers.jl
    ├── Utils.jl
    ├── VortexElement.jl
    └── WriteUtils.jl
```

E.2.1 `Common.jl`

This file contains the code common to the inverse and direct dynamics frameworks. They involve for instance the computation of the bound vorticity, the positioning of the swimmer, etc.

E.2.2 `DirMBS.jl`

This file contains the code specific to direct dynamics of a MBS.

E.2.3 `DirFish.jl`

This file contains the code specific to the direct dynamics of a swimmer like the initialization, the time integration of the system. The computation of the coupled added mass matrix is performed in this file.

E.2.4 `Forces.jl`

Everything force-related is developed in this file: all three formulations for the force and moments are there as well as the computation of pressure distribution or fluid impulse.

E.2.5 `InvFish.jl`

This file contains the code specific to the inverse dynamics of a swimmer like the initialization, the time integration of the system.

E.2.6 `InvMBS.jl`

This file contains the code specific to invers dynamics of a MBS.

E.2.7 `MBS.jl`

This file contains the code specific to Euler-Lagrange framework but common to both inverse/direct dynamics setups.

E.2.8 `MultiFish.jl`

In this code, we enable simulations with multiple swimmers. Added mass matrix for the whole system is computed, time integration ow the full system is performed, bound vorticity is solved for.

E.2.9 `Swimmers.jl`

This file gives the user the right to access a set of functions from outside the package. It coordinates all the other files.

E.2.10 `WriteUtils.jl`

This file is dedicated to I/O.